TAMPEREEN TEKNILLINEN YLIOPISTO
TAMPERE UNIVERSITY OF TECHNOLOGY

WENJUAN ZHOU

FORWARD STUDY OF THE STRUCTURAL MATERIALS FOR THE SUPPORTING SYSTEM OF THE CLIC TWO-BEAM MODULE

Master of Science Thesis

Examiner: Professor Jyrki Vuorinen
Examiners and topic approved by the
Department of Materials Science
Council meeting on 8 April 2015.

ABSTRACT

TAMPERE UNIVERSITY OF TECHNOLOGY
Master's Degree Programme in Materials Science
WENJUAN ZHOU: FORWARD STUDY OF THE STRUCTURAL MATERIALS FOR THE SUPPORTING SYSTEM OF THE CLIC TWO-BEAM MODULE
Master of Science Thesis, 81 pages, 10 Appendix pages
August 2013
Major subject: Polymeric Materials
Examiner: Professor Jyrki Vuorinen
Supervisors: Ph.D Kenneth Osterberg, Dr. Germana Riddone, Dr. Nick Gazis
Keywords: girder, Boron Carbide (B_4C), Aluminum Oxide (Al_2O_3), Macor machinable glass ceramic (Macor), Brazilian disk test, three-point bending test, simulation, Young's modulus, Poisson's ratio, tensile stress, tensile strain

The supporting system for the CLIC Two-Beam Module plays a fundamental role for the support and alignment of the RF-components. Thus, the structural materials of the girder and V-shaped supports, along with their corresponding joining methods, need to follow a dedicated study. So far, one baseline and one so-called alternative material have been studied and the very first supporting system prototypes have been produced out of both materials, and undergo validation testing. The stiffness properties in combination with issues faced regarding the precise assembly of the V-shaped supports and the girders require an additional study. The aim of this thesis is to investigate and study potential candidate materials which present similar mechanical properties compared to the materials used for the prototype fabrications so far.

The thesis is divided by the theoretical part, followed by the experimental part. In the theoretical part, the mechanical properties of selected materials are studied and compared. The factors limiting the material selection for the supporting system and their corresponding joining methods for the different materials are studied. In addition, the thesis focuses on determining an innovative testing methodology for the studied materials. Furthermore, the relevant optical inspection is foreseen to validate and to provide additional information regarding the surface quality and shape of the fractured area on the candidate materials which will be tested. The goal of the testing part is to obtain and process the experimental data through a series of mechanical and possibly radiation tests on material specimens, in order to validate and confirm or reject the potential use of the tested materials for CLIC fabrications, such as the supporting system of the Module or other. Moreover, the scientific approach of the thesis can result to a useful extension on the material mapping that takes place for the CLIC structural materials.

PREFACE

This thesis is carried out at CERN in collaboration with Helsinki Institute of Physics (HIP). The mechanical tests (Brazilian disk test and three-point bending test) took place at the National Technical University of Athens in the framework of the CLIC-NTUA collaboration of CERN.

First of all, I am grateful to my supervisors Dr. Germana Riddone and Ph.D. Kenneth Osterberg for accepting and providing me such a good opportunity to work at CERN. Since the thesis topic started, Dr. Germana Riddone gave me many advices and supports. Her seriousness and rigorous taught me a lot. Thanks to Ph.D. Kenneth Osterberg for accepting me and supporting me as a research assistant and a thesis worker in HIP and at CERN. Thanks for his concern, suggestions and comments on this thesis.

I am especially thankful to my thesis supervisor Dr. Nikolaos Gazis. Thanks for his guidance, tutoring and support during the forward material study for girders of CLIC Two-Beam Module. He really took care of my thesis work through weekly actions, experimental processes, thesis writing and presentations. He has been offering me numerous time and energy on my work and papers. He gave me valuable advices and infinite help. Without his contribution, I could not achieve my thesis in this half year.

I would like to thank my professor Jyrki Vuorinen from the Tampere University of Technology for accepting me on this thesis and supporting me on my master thesis application. I am grateful for his guidance, encouragement, comments and for looking over the thesis.

I want to thanks professor S. Kourkoulis, Dr. Pasiou Ermioni and Miss Ioanna Dakanali from the National Technical University of Athens. Thanks their help and tutoring during the experiments in NTUA.

I also want to say many thanks to my colleagues in the CLIC RF working group at CERN, and those friends I met at CERN. Their kindness and friendship made my stay in Switzerland wonderful.

Last but not least, a huge thanks to my parents and my brother. Without their understanding, support and encouragement, I wouldn’t have been able to see the different part of the world, study abroad, work at CERN, and meet friends abroad.

Geneva, August 21, 2013

Wenjuan Zhou

CONTENTS

TERMS AND DEFINITIONS

CERN	The European Organization for Nuclear Research
CLIC	The Compact Linear Collider
LHC	The Large Hadron Collider
ALICE	A Large Ion Collider Experiment
CMS	The Compact Muon Solenoid
LHCb	a Large Hadron Collider beauty
ATLAS	A Toroidal LHC Apparatus
TBA	Two-Beam Acceleration
multi-TeV	multi-Tera-Electron-Volt
RF	the Radio Frequency
DB	Drive Beam
MB	Main Beam
DR	Damping Ring
IP	Interaction Point
AS	Accelerating Structure
PETS	Power Extraction and Transfer Structures
TBM	Two-Beam Module
OFE	Oxygen-Free electronic copper
EBW	Electron-Beam Welding
MBQ	Main Beam Quadrupoles
DBQ	Drive Beam Quadrupoles
EM	Conventional electromagnets
PM	Permanent magnet
BPM	Beam Position Monitors
BLM	Beam Loss Monitors
CLEX	Experimental Area
CTF	the Linear Collider Test Facility
XFEL	the X-Ray Free-Electron Laser
CTE	Coefficient of Thermal Expansion
SiC	Silicon Carbide
CMCs	Ceramic Matrix Composites
Al_2O_3	Aluminum Oxide
B_4C	Boron Carbide
TiC	Titanium Carbide
CAE	Computer-Aided Engineering
Tensile strength	The maximum tensile stress that a material can withstand before failure.
Compressive strength	The maximum stress in compression that a material can withstand before compressive failure.
Ductility	The ability of a solid material to deform plastically under

	tensile stress.
Shear strength	The maximum shear stress that a material can withstand.
Young's modulus	The ratio of linear tensile stress to linear strain when a material is under tension. It is also known as elastic modulus or tensile modulus.
Poisson's ratio	The negative ratio of lateral strain to axial strain when a material is under compression in one direction.
ISRM	The International Society for Rock Mechanics
T/D	The thickness to diameter ratio
RFPA	Rock Failure Process Analysis
ASTM	The American Society for Testing and Materials
RoR	Ring-on-Ring biaxial bending test
4PB	4-point-bending test
3PB	3-point-bending test

1. INTRODUCTION

CERN, the European Organization for Nuclear Research, is amongst the largest physics research and experimental center internationally and provides a wide range of projects for researchers and students. The CLIC (Compact Linear Collider) study, a world-wide project for a future electron-positron collider, would provide a significant research result of the unique combination of high energy and experimental precision (for exploring further knowledge of the universe). To realize the production of such machine, the CLIC Two-Beam acceleration concept was proposed and the study of related technical systems is progressing.

The current chapter introduces CERN, the experiments, and the CLIC study, one of the latest research projects, the CLIC Two-Beam acceleration scheme and the Modules. The research methodology and the structure of the thesis are presented as well.

1.1. CERN – The European Organization for Nuclear Research

CERN, the European Organization for Nuclear Research, was founded in 1954 by 12 founding states. Since then, more countries joined the organization. Today, CERN has 20 European member states (shown in Figure 1.1), one candidate (Romania) to become a member state of CERN, three associate members (Serbia, Israel and Cyprus) in the pre-stage of CERN membership [1]. In addition, CERN has a wide collaboration with nations from all over the world.

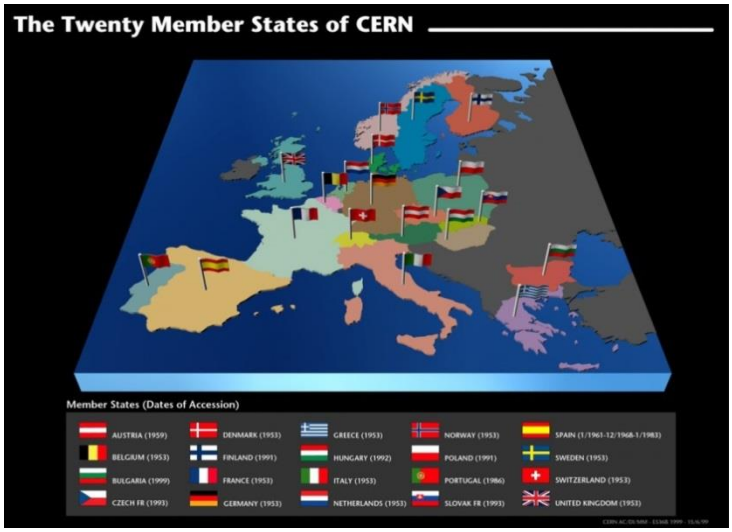

Figure 1.1.*CERN member states [2]*

As one of the world's largest particle physics laboratory, CERN is located across the France-Switzerland border. There are more than 3000 employees, over 10,000 visiting scientists and engineers, representing 608 universities and research institutes and more than 100 nationalities, contributing to CERN programs [3]. In addition, hundreds of students come to CERN for training in research and engineering fields. One of the initial goals of CERN is to understand the inside of nucleus. However, the development of science is beyond the initial goals. Today, the research is deeper than the study of nucleus, and the particle physics become CERN's key research area, which is a study of the fundamental particles of the universe by using the world's largest and most complex scientific machines. The process and the result provide clues of the elementary particles to physicists. For this reason, it became a huge engine to promote and pursuit the science, technology, and human knowledge to go forward.

There is a series of massive experiments carried out at CERN. The Large Hadron Collider (LHC) is the largest and most powerful particle accelerator in the world, and is an approximately 27 km long ring and constituted of superconducting magnets. A heavy-ion detector, a Large Ion Collider Experiment (ALICE), and a general-purpose detector at the LHC, named as the Compact Muon Solenoid (CMS), a Large Hadron Collider beauty (LHCb) are integrated detectors in the LHC ring. In addition, one of two general-purpose detectors at the LHC, the ATLAS, probes physics such as the Higgs boson, dark matter etc. The map of CERN complex is shown in Figure 1.2.

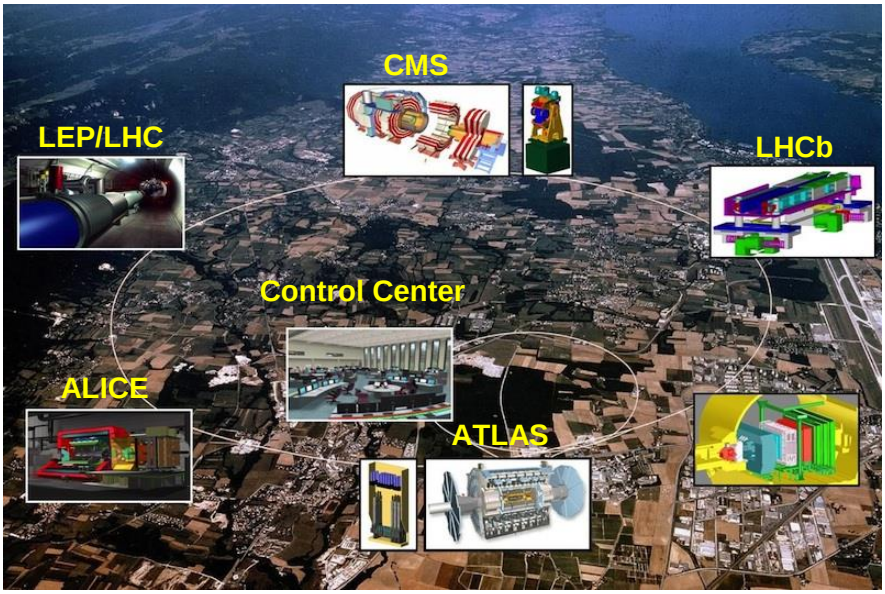

Figure 1.2. *Map of CERN complex [4]*

Moreover, experiments at CERN require massive data processing and analysis, which is conducted around the world and provides the foundation for future developments in computer science. Briefly, research, technology, collaboration and education have been CERN's main missions since 1954 [5].

1.2. CLIC study overview

The Compact Linear Collider (CLIC) study is focusing on the development of a design for a multi-Tera-Electron-Volt (multi-TeV) electron-positron (e+ e-) collider at a colliding beam energy of 3 TeV with a luminosity of 2×10^{34} cm^{-2} s^{-3} [6]. The energy range of linear colliders is extended by developing a new technology of Two-Beam acceleration (TBA). The CLIC concept is based on the scheme of Two-Beam particle acceleration, where the Radio Frequency (RF) power is obtained from a low energy but high-intensity particle beam, called Drive Beam (DB), and conversed with a parallel high energy accelerating particle beam, called Main Beam (MB). The high energy particle beams in Main Beam are produced and pre-accelerated in the injector. Then, in the damping rings (DR), ultra-low emittance is reduced before any further acceleration or transfer. The layout of the CLIC accelerator complex is shown in Figure 1.3.

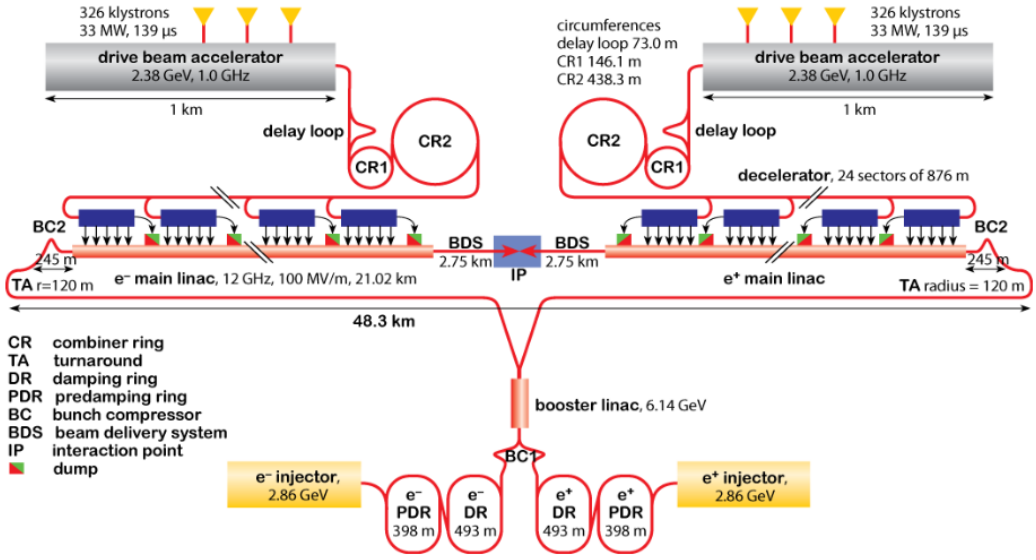

Figure 1.3. *The CLIC layout at 3 TeV [7]*

The whole process of small emittance beam generation and conversion requires RF power. The construction of an approximately 48 km long linac demands extremely tight geometrical tolerances (µm level) and high beam stability at the Interaction Point (IP), one of the key issues of the CLIC study. Hosts of the components of the collider, such as Accelerating Structures (AS), Power Extraction and Transfer Structures (PETS), Magnets/Quadrupoles, RF-network, supporting system, alignment and re-position systems etc. require such geometrical tolerances.

1.3. The CLIC Two-Beam acceleration scheme and the CLIC Two-Beam Modules

CLIC is based on a Two-Beam acceleration scheme, and the innovative scheme of two main linear accelerators is constituted of the MB and the DB. All technical systems are integrated in it. Figure 1.4 shows the principle of the Two-Beam scheme: RF power is

obtained by the PETS and transferred from the PETS of DB to the AS of the MB, and the particle beam acceleration is achieved in the AS under a frequency of 12 GHz.

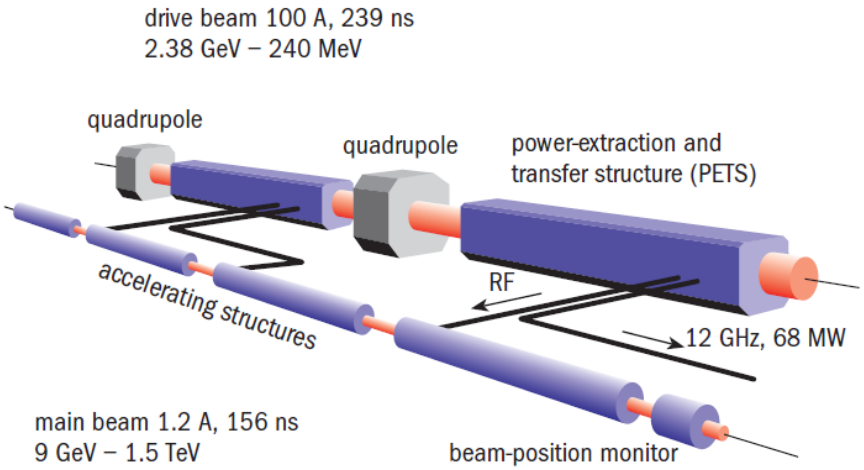

Figure 1.4. *Principle of the Two-Beam scheme [8]*

CLIC is divided into thousands of AS segments in the MB and PETS sectors in the DB. Meanwhile, dedicated waveguide networks and RF components realize the connection between AS and PETS. The smallest fundamental repetitive unit of the collider is the Two-Beam Module. The Two-Beam Modules are assembled in series and form two individual approximately 21 km long linacs [6]. According to the technical requirements of the particle beam, there are several types of Two-Beam Modules (so called TBMs). An indicative type of TBMs (Type-1) is supported on a dedicated supporting system, as shown in Figure 1.5 [6].

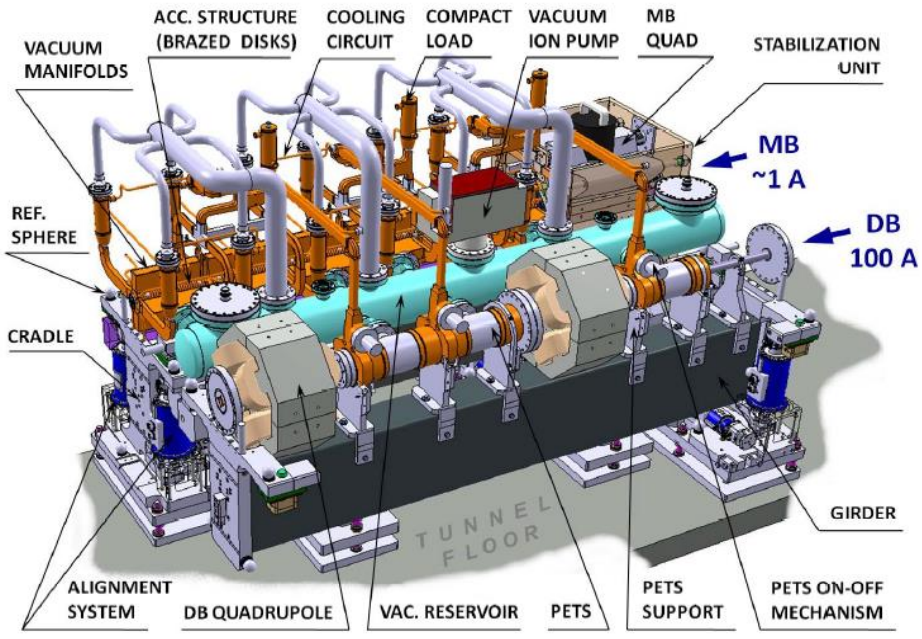

Figure 1.5. *3D view of the CLIC Two-Beam Module (Type 1)[6]*

The RF components of the TBMs are housed on girders, the fundamental component of the CLIC supporting system that allows the precise alignment of components along the two linacs. The RF components are repeated periodically in the TBMs. A micro-precision is required in the structures so as to align and realize the particle beam collision. All girders constitute a mechanically articulated chain along the two linacs. This mechanical interconnection forms the so called “Snack System” [6].

1.4. Technical Systems

Each TBM is formed by different technical systems. The requirements of the different technical systems have to be taken into consideration during the design. The main technical systems are described in this section, such as the RF structures and RF system, vacuum system, cooling system, magnet system and magnet stabilization system, beam instrumentation, supporting and alignment system. Some general information which includes the main components and the key manufacturing issues are followed.

1.4.1. RF structures and RF system

For the Two-Beam acceleration, RF power is generated from the DB, decelerated by low-resistance PETS, transferred to the MB and accelerated by a high-resistance AS. Accordingly, the kinetic energy is transferred from a high-current but low energy DB to a low-current but high energy MB by using the two RF structures, so that a high transformer ratio can be realized [6].

The smallest unit of the 12 GHz RF system is built with a single PETS, feeding two AS by the RF network, which is shown in Figure 1.6. An AS is assembled with Oxygen-Free Electronic copper (OFE) bonded discs, irises, compact couplers and damping waveguides. Then, a Super Accelerating Structure is formed by two AS. In parallel, two PETS, together with a mini-tank and an output coupler, form a PETS unit, via electron-beam welding (EBW) [6].

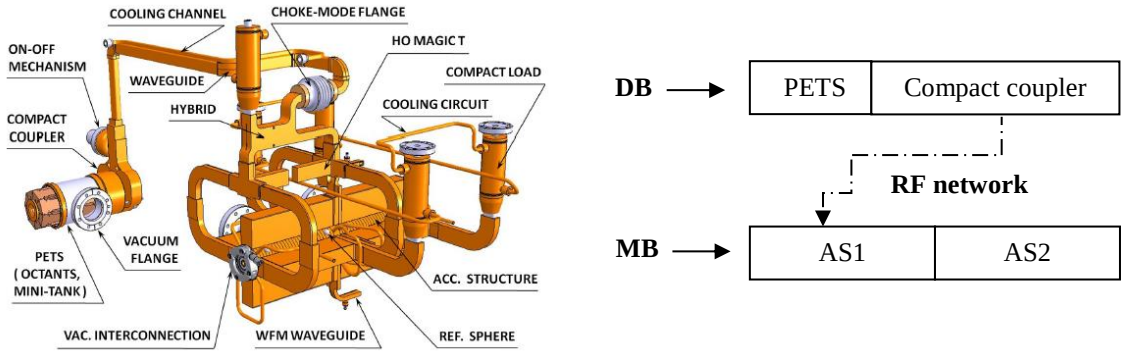

Figure 1.6. *Lay out of RF system*
(Left: 3D Layout of RF network; Right: scheme of RF system) [6]

The main components of the RF system are the AS, the PETS and the RF network together with waveguides and the RF components. The design has strict geometrical and dimensioned tolerance requirements, as listed in Table 1.1 [9].

Table 1.1. *Tolerance requirements of the RF system [9]*

	AS	**PETS**
Shape Accuracy	5 μm	15 μm
Assembly	10 μm	31 μm
Pre-alignment	14 μm	100 μm

1.4.2. Vacuum System

To reduce the beam-gas interactions while beams travel in the particle accelerators, the molecules of the residual gas left in the vacuum atmosphere are the mainly restrictive factor. Usually, the beam-gas interactions limit the machine performance, such as reducing beam lifetime (which leads to nuclear scattering) and luminosity (which cause multiple coulomb scattering). It also causes pressure and electron instabilities. Effects of the beam-gas scattering not only increase the radiation dose rates in the accelerator tunnels, but also increase the chance for the detector to see the background in the experimental areas, resulting in the material activation, tunnel infrastructures untimely degradation, and degradation of the electronics in the tunnel and service galleries [6]. Thus, the beam vacuum system in the CLIC accelerator must comply with different design requirements and the effects of the CLIC complex. So, various types of vacuum are able to be differentiated from the vacuum chamber temperature (cold or room temperature), baked or unbaked system, coated or uncoated chamber [6]. Currently, the baseline of the TBM vacuum system avoids the odds of heating the vacuum enclosure for geometrical stability reasons, which leads to an unbaked system. The 3D layout of the CLIC module vacuum system is illustrated in Figure 1.7 [6].

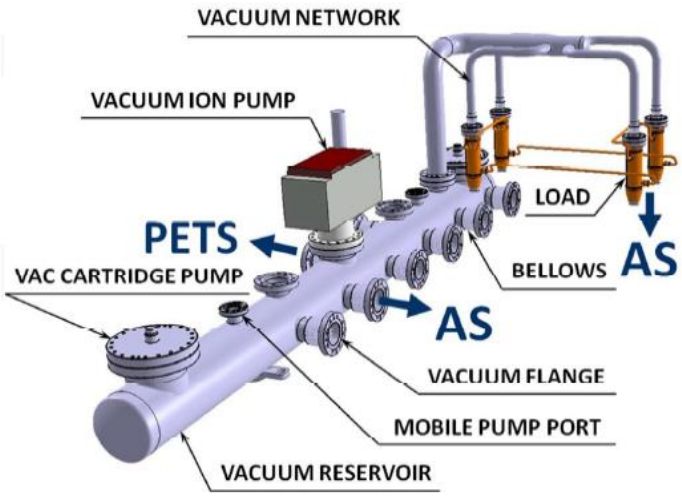

Figure 1.7. *Layout of the CLIC Module vacuum system [6]*

A vacuum pump is connected with two cartridge pumps by vacuum flanges through vacuum reservoir tube. A mobile pump port with a roughing piston connects a mobile turbo-molecular pump station that is for preliminary evacuating. Such interconnections between main components offer a sufficient electrical continuity with low impedance but flexibility to sustain the vacuum force and without limiting the alignment of the RF components [6].

1.4.3. Cooling System

The demanded RF power is usually dissipated as a thermal energy in the TBM structures. To minimize the average dissipated power per unit length, and compensate the nominal operation temperature, the cooling system is an essential part to be considered in TBM structure. Because of the different structures, the MB Quadrupoles, the cooling layouts of all types of TBMs are different. Besides, the requirements of vacuum, alignment and mechanical stability give demands for the cooling system. Also, the tight tolerance requirements of TBM define the parallel cooling configuration. Circulating water of the cooling system is used to cool down about 95% heat of the components in the Modules of each 21 km long linac. The size of cooling pipes is affected by the TBM as well. The temperature difference between the different types of TBMs also influences the diameter of the cooling pipes [6].

1.4.4. Magnet System and Magnet powering system

The magnet system is constituted primarily of the Main Beam Quadrupoles (MBQ) and the Drive Beam Quadrupoles (DBQ). As a group of the major components of the TBMs, the MBQs (2010 units per linac) are required to focus the MB along the linac. The MBQs have various lengths and quantities depending on the type of Quadrupoles. There are four types of MBQs, which have the same cross-section dimensions (with a 10 mm magnetic aperture and 200 T/m nominal gradients) and identical operational parameters. However, the active (magnetic) length is differentiated per MBQ. The cross-section of the magnet is optimized for the beam requirements. The interconnections (electrical and hydraulic) are not optimized for the MBQ prototype phase. The beam-steering correction capability is required along the MB, so a small dipole is added to each MBQ. In parallel, each TBM contains two DBQs (20740 units per linac), which appear along the beam in a dedicated configuration on each Module to keep the DB focusing along the decelerators [6]. Based on the design of the TBM baseline, the assigned space for the DBQs is constant along the decelerators even when the working gradient changes. Therefore, a Conventional Electromagnets (EM) design and an adjustable Permanent Magnet (PM) solution are conducted.

The radiation levels in the Main Linac tunnel may have a significant effect on the powering of the 50,000 magnets. With the power transfers in the tunnel, more aspects will be affected, such as the mean time between failures and the efficiency. So, the powering

of all magnets is done in dedicated radiation-free caverns (one per accelerating sector). The powering strategy of the MBQs and DBQs has been created in order to minimize both length and cross-section of the cables which are used for MBQs and DBQs [6].

1.4.5. Beam Instrumentation

The TBM beam instrumentation mainly includes Beam Position Monitors (BPM) and Beam Loss Monitors (BLM). Beam instrumentation will be placed above special girders at the end of each DB decelerator for the MB and on Modules of four types for the DB. The MB contains about 4,000 BPMs (one BPM per Quadrupole). Meanwhile, the DB requires about 42,000 BPMs (two Drive Beam BPMs per Module). Therefore, there will be a large quantity of BPM produced [6]. Besides, due to the rigid connection between BPM and quadrupole, the related position (both x and y directions) cannot be adjusted. To measure the BPM position with respect to the quadrupole, the alignment objective is built on the top. In addition, only 25 mm short strip line BPMs will be used for the DB BPM, which will enable the measurement from DB BPM to Quadrupole [6]. As an integral part of the CLIC machine protection system, the main purpose of the BLM is to prevent the damage to the accelerator components and to monitor the daily operation.

1.4.6. Supporting and Alignment system

All micro-precision CLIC structures are mounted and aligned on girders. All girders of CLIC Modules constitute the Snake System, as Figure 1.8 shows [6].

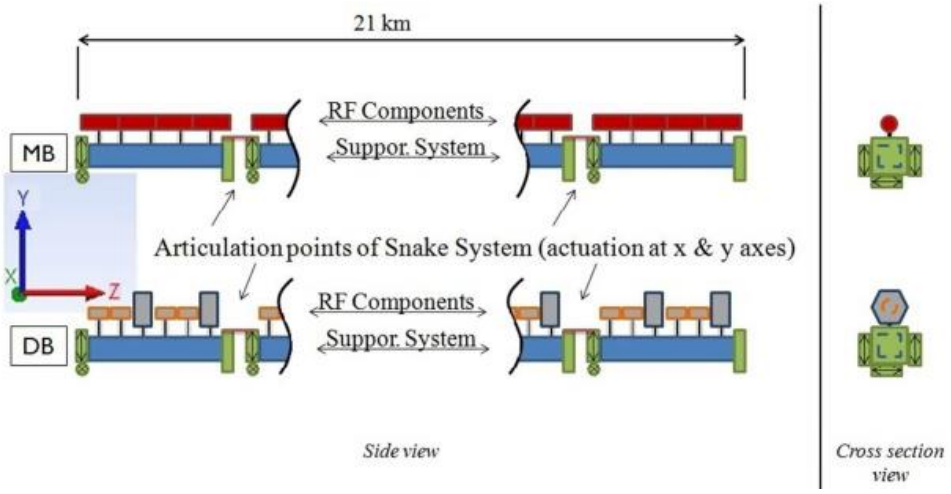

Figure 1.8. *The supporting "Snake-System" concept [6]*

To realize the different technical requirements for supporting and stabilization of the RF components, the supporting system is mainly constituted of girders, V-shaped supports, actuators, cradles and alignment sensors, as Figure 1.9 shows [6].

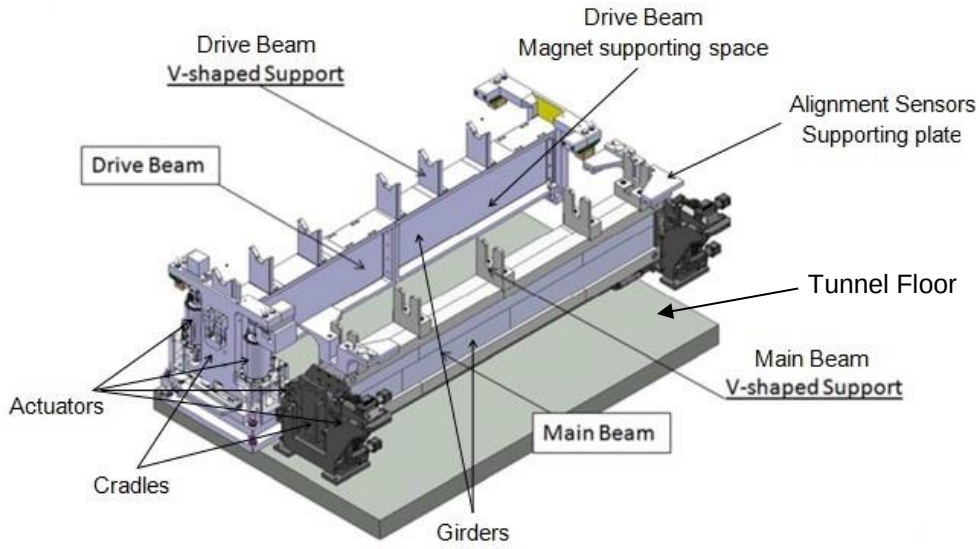

Figure 1.9. *CLIC Two-Beam Module (Type 0) supporting system [6]*

The intermediate parts between the RF components and the girder are the V-shaped supports. The essential issue of the supporting system is the stiffness of the girders and the V-shaped supports, which are supposed to have higher stiffness values compared to the other components of the CLIC TBMs. The possible static deflection of the girders and V-shaped supports has to be considered when calibrating the actuators. The supporting system must also contain a reference transfer system to represent the beam axis with respect to the outside surface of the RF structures [6]. The detail engineering design and technical requirements of the girders and the V-shaped supports are described in chapter two.

To avoid overmuch emittance increasing, all the beam line elements, especially the BPMs, have to be aligned with high accuracy. Each linac needs to be built with a complex pre-alignment system, which uses a sequence of overlapping wires along the whole linac length as a reference line. The pre-alignment of the TBM will take place without particle beams. The alignment system is divided into two steps. One is the mechanical pre-alignment of all components between + 0.1 mm and – 0.1 mm with respect to the metrological reference network. The other is the active pre-alignment which determines in reality position of each component and readjusts respectively the normal position of it via the remote-controlled actuators [6].

1.5. Case study and structure of the thesis

In the present thesis, the study of three types of candidate structure materials is presented for the supporting system of the CLIC Two-Beam Module. The so-called CLIC forward material study is a new project leading to further study of the structural materials for the supporting system. The thesis focuses on studying three categories of potential structural materials based on currently used baseline and alternative structural materials

of the supporting system. It can result in a meaningful application for general of mapping the future CLIC structural materials. The current study and recent application on the supporting system of the forward study are implemented step by step. Starting from studying the technical specification of the supporting system and investigating potential materials for simulation and mechanical tests, finally material properties are analyzed in different stages. The mechanical tests are related to the material properties which will affect the application of manufacturing and operating of the supporting system. The simulation is considered the only way to preliminarily determine the needed Young's Modulus, stresses, strain limit, and deformations. A comparison of the simulated values with the experimentally obtained data is presented. The structure of the thesis relies on the implementation of above mentioned processes. Amongst them, all simulations are conducted by the help of the ANSYS Workbench 15.0 software.

The main CLIC technical systems are presented and the key technical requirements of the supporting system are introduced during the studying process. The alignment requirements are also presented. The main goal focuses on the materials, properties and applications. The technical conditions of simulation and mechanical experiments are also introduced. The thesis presents the principles and strategies of material selection, sample design, simulation and mechanical tests. In the discussion part, the results and the experimental approach are evaluated. Also future types of testing such as radiation tests and thermal analysis are considered.

2. ENGINEERING DESIGN OF THE SUPPORTING SYSTEM AND STRUCTURAL MATERIAL SELECTION

The current chapter describes the engineering design and the operational conditions of the supporting system. The main components of the supporting system are described. In addition, the baseline material, alternative material and candidate materials are introduced.

2.1. Boundary and operational conditions

As mentioned in chapter one, the tolerance requirements for the alignment of the TBM components are challenging. The girders are positioned and re-aligned parts of the supporting system in the underground tunnel.

The extremities of each girder are mechanically connected with a cradle. On each cradle, two vertical high resolution linear actuators and one radial high resolution linear actuator together with a mechanical articulation point are assembled. The "stand-along" station formed by two adjacent cradles equipped with their actuators provides three degrees movement, also described as master-slave movement [10]. It helps to realize the micro-position adjustment towards x, y or z axis, as Figure 2.1 presents. In addition, V-shaped supports are used to link girders and RF structures. To realize the alignment of RF structures with respect to the particle beam axis, micro-positioning reference is required for each of the V-shaped supports. The main differences between all types of supporting systems are the length of the MB girders, as shown in Figure 2.1 [11].

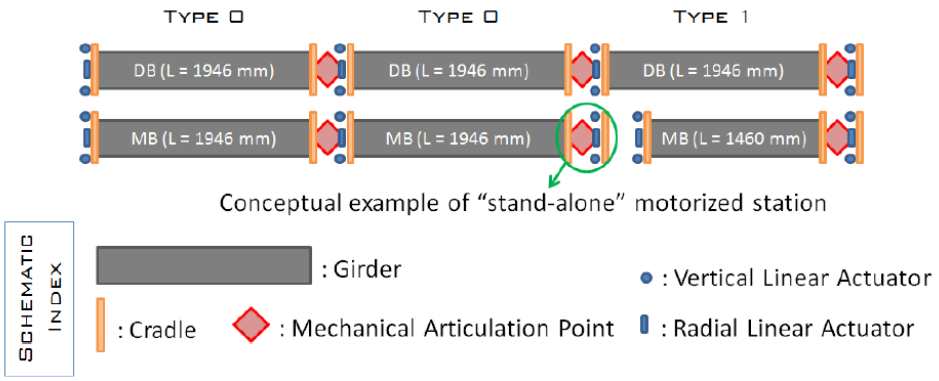

Figure 2.1. *Schematic representation of the master-slave movement for TBM [11]*

A configuration of indicative girder is illustrated in Figure 2.2, which has maximum length of 1946 ±1 mm, maximum height of 320 ±1 mm and width of 150 ±1 mm with 50 mm wall thickness of the cross section. The tolerance of flatness of the reference surfaces is 5-10 μm. Due to the space limitations, a compact girder design is required. Based on a series of studies and taking into account the existing manufacturing methods and the valid precise machining methods, a rectangular hollow tube was chosen for the baseline configuration of the girder. Such a configuration is defined as a result of an extensive optimization, with the allowed static deformation value of no more than 10 μm under the loading of RF structures. Meanwhile, other cross sections (such as a solid I-shaped girder cross section) have been evaluated [12].

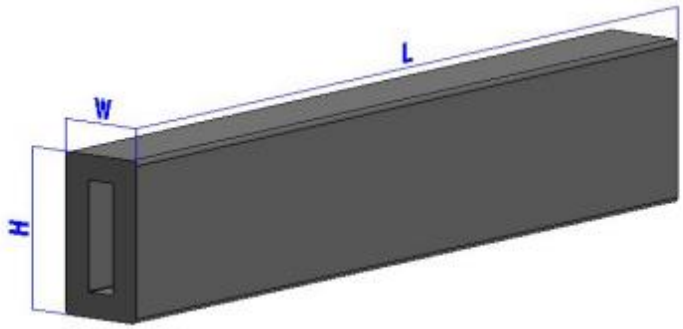

***Figure 2.2**. CLIC Module girder baseline configuration*

To preserve the alignment of the particle beam in a few micrometers, the girders shall maintain the damping and isolation of the dynamic behavior of the CLIC TBM [6]. As one of the largest and important component for the MB and the DB, the main parameters for the girder are listed in Table 2.1 [11].

***Table 2.1** Main technical requirements of girders [11]*

Parameter	Requirement
Modulus of elasticity (Young's Modulus)	≥ 320 GPa
Mass per girder (universal)	≤ 240 kg
Maximum vertical deformation in loaded condition	10 μm
Maximum lateral deformation in loaded condition	10 μm
Maximum weight on top of the girder (distributed load)	400 kg/m
Loaded girder eigenfrequency (1st mode)	> 50 Hz
Unloaded girder eigenfrequency (1st mode)	700 Hz

The maximum weight of each girder makes material selection process more challenging. Several industrial materials such as aluminum alloys and stainless steels were investigated and excluded due to the strict requirements of girders. Structural materials like carbon fiber composites and metal foams couldn't meet the length requirement in the previous study [6]. Besides, low static deformation values are required. To archive the stiffness requirement for the girder material, a group of potentially interesting materials

were studied and compared. Various static deformation values are summarized in Table 2.2 [10, 12].

Table 2.2. *Material comparison of Girder [10, 12]*

Materials	Static Deformation loaded with RF components (μm)
Aluminum-6061-AHC	43.39
Austenitic Stainless Steel	36.49
Beryllium	82.64
Carbon Fiber Composite	66.68
Epument 140/5	15.08
Epoxy-Aramid Fiber Composite	69.96
Silicon Carbide (SiC)	3.8
Structural Steel	36.29
Stainless Steel 440C	35.32
Titanium	48.46

In above simulation result table, a baseline material - Silicon Carbide (SiC) with less than a static deformation of 10 μm was proposed, and an alternative material - Epument 145 B with slightly more than a static deformation of 10 μm was shown. Despite its static deformation result, the Epument 145 B is still considered for further research on girders.

The V-shaped supports have flatness requirement on their upper surface to ensure the RF structures are aligned while the accelerated beams pass through. Thus, V-shaped supports have to be firmly fixed on girders.

There are two prototypes of girder. One is made from the baseline material SiC, another is made from the alternative material Epument. Correspondingly, V-shaped supports are made from SiC and stainless steel. Because of the mechanical properties, V-shaped SiC supports have to be brazed on SiC girders. While the stainless steel V-shaped supports can be mechanically fixed to Epument girders [12]. So far, the combination of SiC girders with SiC V-shaped supports works well, except it is hard to transport the whole assembled structure. But the combination of Epument girders with mechanically fixed stainless steel V-shaped supports has some assembly stability difficulties. The detail information is presented in the following section.

The cradles are equipped with positioning sensors and inclinometers, which are assembled on each longitudinal extremity of the girder. The vertical and lateral displacements of the girders are provided by the high resolution linear actuators. The Figure 2.3 gives a schematic view of a cradle with actuators [13]. Thanks to nano-metric adjustments,

the actuators provide the possibility of moving, regulating the position and timely maintaining a stable position of girders.

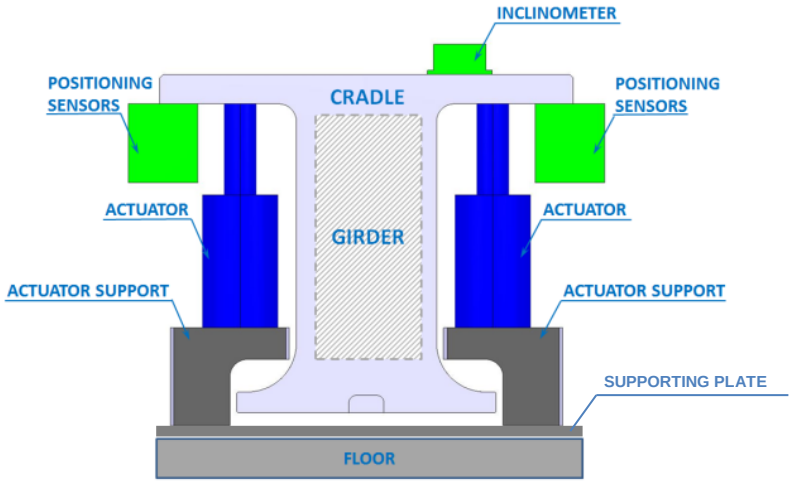

***Figure 2.3**. Schematic view of the cradle with actuators and sensors assembled [13]*

2.2. Key parameters of the material study

The forward material study is based on the established technical specification of the supporting system. The background of structural material should sustain the aging effects of high radiation. For the TBM, there are two different test configurations. The first configuration is to realize integration and operation of different accelerator components and sub-systems in a linac. This configuration involves installing CLIC Modules in the LAB (with so called “mock-up” RF-component) with neither particle beam acceleration nor RF field. The RF AS and quadrupoles are replaced by mock-ups made of the same material and having the same volume. The mock-ups have real mechanical functions and precision of geometrical tolerances. This conception is as close as possible to the one of future CLIC machine. The second configuration is the Modules in the CLIC Experimental Area (CLEX). The Modules are installed in CLEX with particle beam acceleration and RF field. The real components are integrated to the existing test infrastructures and testing environment.

A series of tests should be conducted in order to understand the properties of the selected material, and to use the material in proper application. The mechanical performance of materials is very important for analyzing the material failure situation, and the mechanical properties of materials are obtained by series of mechanical tests. In the mechanical tests, it is fundamental for the material to be homogeneous or to behave homogeneously, because the homogeneity of the microstructure of the material is enough to represent the average behavior of the material on a macroscopic scale. However, impurities always exist in materials and it is very hard to produce pure materials. In this study, the material which presents homogeneous behavior in all directions of its cross-section will be investigated, simulated and tested.

SiC is used in the existing CLIC test facilities such as CTF (the Linear Collider Test Facility). It appears to have the best stiffness to sampling rates and the minimum static deformation. Thus, SiC is chosen as the baseline material of girders. Moreover, each girder has the maximum two meters length requirement. It requires restricted feasible fabrication methods in industry (such as the size of furnace, material homogeneity) [6]. For this reason, the sintered SiC composite is applied on girders.

In addition, a mineral cast material called Epument 145 B is made from epoxy resin reinforced with different sizes of rocks. This mineral cast is used for the girders of the X-Ray Free-Electron Laser (XFEL) accelerator in PSI [14, 15]. Compared with SiC, Epument involves less fabrication steps (no casting modules), short production cycle, easy mechanical assembly flexibility and about 10 times lower cost. Thus, Epument 145 B was introduced as the alternative structural material for the girder of the CLIC TBM [10, 12].

Currently, a prototype of the girders is made from the baseline material SiC. Another prototype, which is made from the alternative material Epument mineral cast, is still under validation. Thus, a reference material of the V-shaped supports with respect to each other and to the girder cradles is needed. The detail is explained in section 2.3.

As mentioned, girder has micrometric precision machining requirement. When choosing materials, the corresponding transportation, assembly and all possible operations have to be taken into account. Due to the temperature changes during operation of the machine, material will expand. Therefore, material's Coefficient of Thermal Expansion (CTE) has to be considered. Besides, high resolution linear actuators are used for micro-precision positioning for the supporting system, and the girders are installed with them. Because the actuator is quite expensive device, it cannot be changed without a significant budget impact. Yet, the material can be selected, so can the density of materials. In order to select a material under the maximum weight required, three criteria are fundamental: the Young's modulus, the Poison ratio, and the density.

2.3. Material selection

To support the static loads of the TBM, a fulfill girder is required. Considering the required homogeneous behavior of each material, a comparison study is essential.

Through the comparison in Table 2.2, the selection range of materials covers from metals to plastic and ceramics. More candidate materials need to be studied for the needs of the forward study, even though a baseline material SiC is used, and an alternative material Epument 145 B is under studying for CLIC girder. This section introduces the baseline material, the alternative material and three candidate materials.

2.3.1. Baseline material (SiC) and Alternative material (EPUMENT)

Silicon Carbide (SiC) is a compound of silicon and carbon [16]. It is a ceramic material with properties similar to diamond's, such as high hardness, low bulk density and high oxidation resistance [17]. It is extremely rare to find SiC in nature, and it is difficult to manufacture high-purity SiC. Thus, most of the industrially using SiCs are made from synthetic methods depending on the usage requirements. Usually, SiC is sintered, hot pressed, or reaction bonded [18]. Impurities like boron can be added for sintering, or introduced in reaction bonding. Direct-sintered SiC and reaction bonded SiC are the two structural families of SiC. The direct-sintered SiC is a high-purity product, which is made of compacted and sintered submicrometer SiC powder at more than 2000 °C. Different from the direct-sintered SiC, the reaction-bonded SiC is made of the porous mixture of SiC and carbon-powder, infiltrated with silicon metal [19].

SiCs have many different crystalline structures, also called polytypes. Alpha SiC (α-SiC) has hexagonal crystal structure. It is formed under 1700 °C, and is a polymorph which is used often. SiC has high hardness (27 GPa), excellent thermal conductivities (11 W/m.K), low thermal expansion coefficient which provides very good thermal shock resistance, and high strength (500 MPa). Therefore, SiC is widely used in refractory applications [19], such as radiant heating tubes in metallurgical heat-treating furnaces, car brakes, clutches, bulletproof vests, semi-conductor materials, and LED products. SiC composite material is a very important material for using in nuclear fuel reactors and nuclear fuel cladding, due to its properties of high temperature, high voltage and high resistance to thermal conductivity.

One of the strongest ceramic materials is sintered SiC [19]. Giuseppe Magnani et al. mentioned in their study that through sintering boron and carbon with SiC powder, the flexural strength is affected by the reduced grain size, while the hardness and fracture resistance remained unchanged [16]. The main composition of the baseline material - SiC composite, which has been used in girder, is sintered α-SiC. The density of the SiC is 3.21×10^{3} kg/m^{3}, the CTE is 5.2×10^{-6}/ °C during 20 °C -1400 °C, the Young's modulus is 420 GPa and the Poisson's ratio is 0.16. The datasheet of the used SiC is attached in Appendix 2. SiC has high rigidity, but it is very brittle. Thus, the fabrication and assembly methodologies are challenging. The V-shaped supports are made of SiC as well, so brazing it on girder is possible.

Ceramic matrix composites (CMCs) maintain the high-temperature properties of ceramics but overcome the low fracture toughness of monolithic ceramics. However, composite materials are micro-structurally heterogeneous [20]. To perform desired mechanical tests, making CMCs behaviour homogeneous is important. The alternative material - Epument 145 B is provided by an industrial firm. It is a three components cast polymer based on an epoxy resin, including a material with a combination of special filler. It is

described as a homogenous composite material, which has high rigidity, low thermal conductivity and the CTE is close to steel's. Not only that, its creep behavior is very low under stress. Epument 145 B is used for casting large constructions which require high static and dynamic rigidity, such as vibration engines, gears and turbines. This mineral cast Epument has density of approximately 2.4 g/m^3, the Poisson's ratio is 0.3, and the Young's modulus is from 40 to 45 GPa. The datasheet of the Epument is attached in Appendix 2. Epument can be assembled with mechanical methods, so that the V-shaped supports which are made of stainless steel alloys could be mounted on girders. During transportation, the re-mount could be done easily as well. Since the supporting system has high micro-precision alignment requirements, to meet such demand, the mechanical assembly becomes challenging.

As mentioned in the technical requirements of the girder, the defined minimum Young's Modulus of the girder material is 320 GPa. However, the Young's modulus of the alternative material Epument 145 B is around 45 GPa, which is much lower than the required value. Despite the low modulus, Epument is still considered as a reference material in this study because it has been applied in similar supporting cases (XFEL in PSI) and is 10 times less expensive to manufacture. Even the Young's modulus is 45 GPa, the static deformation with loaded RF components is around 15 μm. The technical requirements of 320 GPa was defined only after studying and establishing the SiC as a baseline material. In this case, a combination of mechanical properties needs to be studied for each material.

2.3.2. Candidate materials

Since those mentioned challenges exist, a forward study of the girder structural materials is continually conducted. Therefore, a group of candidate materials is proposed: Aluminium Oxide (Al_2O_3), Titanium Carbide (TiC), Boron Carbide (B_4C), Macor machinable glass ceramic (Macor), QC-10 mold plate and forged block, and Anocast silica-filled epoxy polymer composite.

Boron Carbide (B_4C) is a hard ceramic material like diamond and cubic boron nitride. It can be manufactured by reacting and fusing the boric oxide and carbon at very high temperature (more than 2000 °C) [18]. The commercial B_4C products are made through hot pressing or sintering and hot isostatic pressing. Hot pressing sintering in a furnace is the most common fabrication method [21]. Most of the commercial B_4Cs are more like a composite of B_4C and carbon in a graphic form. B_4C has rhombohedra like crystal structure. The graphic carbon limits the strength of B_4C [18]. B_4C has density of approximately 2.48 g/cm^3, the Young's modulus is from 450 GPa to 470 GPa, and the CET is 5×10^{-6} / °C. In the study of H.K.Clark et al. it shows that the crystal structure of B_4C has a consecutively bonded three-dimensional form with the presence of the carbon atoms [22]. Thus, B_4C presents exceptionally high hardness, high stiffness, low density, low thermal conductivity and good thermal neutron capture ability [18, 23]. Therefore,

it is used as a refractory material in many important applications. It can endure large amounts of radiation damage, and so can be used in the nuclear industry as a neutron absorber and shielding material and neutron moderators. Moreover, it is used in high temperature thermoelectric power conversion to absorb the thermal neutron that liberates a low energy particle [23, 24].

Polycrystalline glass-ceramics can be formed by controlled crystallization of special glasses [25]. Due to a variety of processing methods that are applicable in manufacturing industries, Macor has drawn attention. It is a two phases white ceramic composite of approximately 55% fluorophlogopite mica and 45% borosilicate glass, which contains silicon, magnesium, aluminum, potassium, boron and Fluorine. The CET of Macor makes it fits together with most of metals and sealing glasses. It also stands high temperatures (maximum 1000 °C). It has good radiation resistance, excellent insulation at high voltages and different frequencies. Macor can be machined with normal metal-working tools, so complex shapes and precision parts can be achieved, and the tight dimensional tolerance can be met. It proves to be a machinable material. Macor can also be joined and sealed in different ways. For example it can be soldered and brazed with metalized components. Macor has been widely used in ultra-high vacuum environments, constant vacuum applications, aerospace industry, nuclear-related experiments and welding nozzles [26].

Aluminum Oxide (Al_2O_3) is also called alumina ceramics. It includes a family of materials which contents of Al_2O_3 from 85% to more than 99 %. The properties of alumina depend highly on the percentage of Al_2O_3. Those differences result in diverse possible applications. Among of those, high purity alumina which contains more than 99% Al_2O_3 has a much simpler microstructure of equiaxed Al_2O_3 grains, compared to the commonly elongated shape. The grain boundary phase can be amorphous or/and crystalline, depending on the way of processing [24]. Alumina usually appears as a crystalline polymorphic phase α-Al_2O_3, manufactured through sintering at high temperature (around 1600 °C to 1700 °C) [27]. The grain size, porosity, purity and size distribution of ceramics affect the properties of sintered ceramics, such as strength, fatigue resistance and fracture toughness. With a small grain size and very high purity, alumina presents excellent compressive strength, good flexural strength, high hardness and low electrical conductivity [24, 27]. Besides the application in orthopedic surgery, alumina is also used as a refractory material for making furnace construction and kiln rollers.

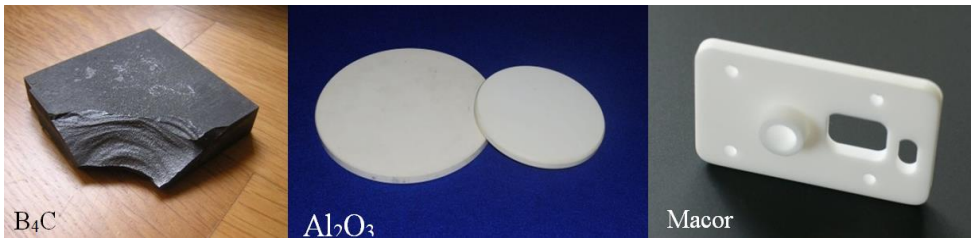

***Figure 2.4**. Products of B_4C, Al_2O_3 and Macor [28, 29, 30]*

Titanium Carbide (TiC) is produced by the reaction between TiO_2 and carbon powders at 1600 °C to 1700 °C. TiC has low density, good high-temperature oxidation resistance, good thermal conductivity and chemical inert ability to steel and iron [31]. It also has high hardness, preferred corrosion resistance and thermal stability.

Anocast Silica-filled Epoxy Polymer Composites can be used for vibration damping products. This feature is better than metals and natural stones have. Compared with metal structure, it has better thermal stability and dimensional stability.

QC-10 Mold Plate and Forged Block, an aluminum alloy, is designed usually for production of injection molds. It has low density, good stability and durability. Its manufacturing time can be greatly reduced, compared with steel. It can be machined by electrical discharge. Besides, polishing and texturization are also possible.

Taking into account the manufacturing feasibility in industrial and the cost aspect of manufacture, the candidate structural materials for the girder to be investigated and chosen are B_4C, Al_2O_3 and Macor, as shown in Figure 2.4.

2.3.3. Summary of candidate materials

After a pre-selection of the candidate structural materials for the girder, B_4C, Al_2O_3 and Macor are all have similar mechanical properties when taking SiC and Epument 145B as references. In addition, the related products can be produced in the industry. The mechanical properties of three candidate materials are summarized and compared with baseline and alternative materials in Table 2.3 [32].

Table 2.3. *Materials comparison*

Materials	**SiC**	**Epument 145 B**	**B_4C**	**Al_2O_3 (99%)**	**Macor**
Density (g/cm^3)	3.21	2.4	2.48	3.81	2.52
Young's modulus (GPa)	420	40-45	450-470	370	66.9
Poisson's ratio	0.16	0.30	0.17	0.22	0.29
Flexural strength (MPa)	450	30-40	440-520	340	94
Compressive strength (MPa)	\	130-150	\	3000-1900	345
CTE (10^{-6}/°C)	5.2	15	5.0	7.6	12.6

As described in Table 2.3, B_4C has higher Young's modulus than SiC. The fact that Al_2O_3 has smaller Young's modulus than SiC is still scientifically interesting to verify whether it can be used for a girder construction or not. Meanwhile, due to the diversity of machining methods, the manufacturing cost can be reduced if Macor could be used for girder.

3. EXPERIMENTAL STRATEGY, SAMPLE DESIGN, PROCUREMENT AND QUALITY CONTROL

Mechanical property characterization is commonly used for research and development, quality control, and design data generation. Different tests can help to investigate, develop and apply materials properly [33]. At current stage, the study of the performance of materials is supported by research and development testing in comparison to competitive materials. By this, the costs of the material and the accuracy of the material data can be controlled. Therefore, a series of mechanical tests are programmed in order to determine and understand the mechanical property of the material, and to characterize its performance and applications. This chapter describes the principal of mechanical tests used for studying the materials, specimen design, procurement and quality control of the specimens. The detailed mechanical tests are presented in chapter four.

3.1. Experimental strategy and sample design

3.1.1. Brazilian disk test and the configuration of the specimen

Tension test and compression test are two of the most common mechanical tests. From the tension and compression test, the material behavior characteristics can be easily determined by the stress-strain curves [34]. For ceramic or ceramic composites, the tension test requires a specimen with a single stress component. The test should also be cost effective with reasonable turnover period and should be easy to be conducted [35]. The basic geometry of the specimen for both tensile test and compression test should be without end tabs. The shape of the specimen can be various. It depends on the type of tests and the used test standards [34].

Brazilian disk test is a common scientific way to indirectly measure the tensile strength of brittle materials (including rocks, concrete and rock-like materials). In addition, observations for the material homogeneity can be made through Brazilian disk test [36]. DiYuan Li et al. reviewed numerical researches that had been done on Brazilian disk test. This test is commonly used to determine the tensile strength of rocks, because the specimen preparation is easier than in the uniaxial tensile test [36]. The details of the Brazilian disk test are presented in chapter four.

In the Brazilian disk test, a thin circular disk, made from the tested material, is loaded by a uniform force and compressed to failure [36]. The disk is assumed to be com-

pressed across its diameter to obtain the indirect tensile strength of the tested material. In Brazilian disk test, one side of the disk is fixed and the symmetrical side of the disk is getting the external loads, until the disk is ruptured. The geometry of the Brazilian disk test is shown in Figure 3.1:

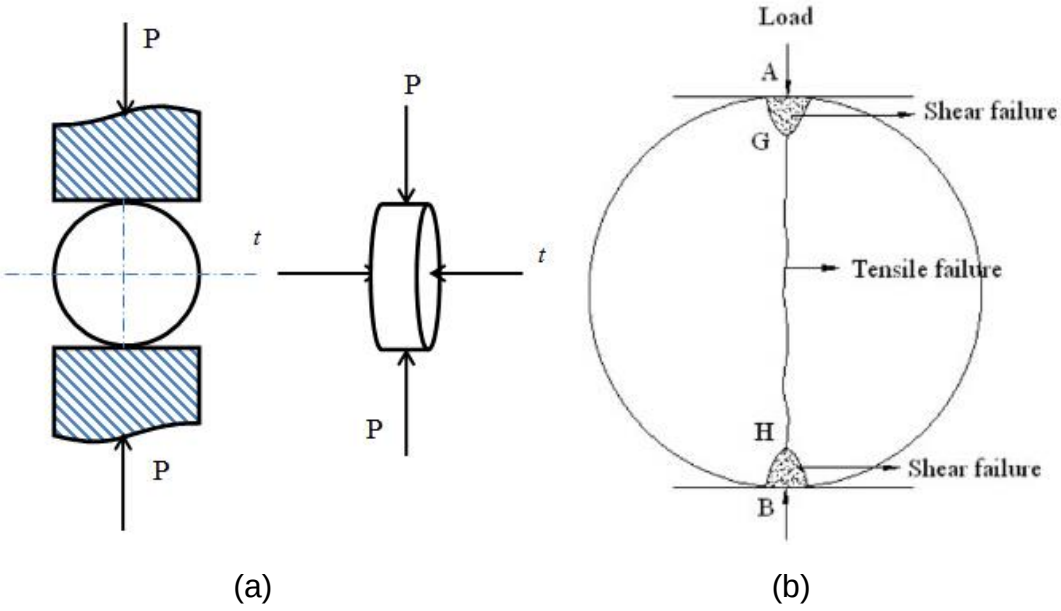

Figure 3.1. *(a) The geometry of the Brazilian disk test (P: uniform load, t: tension) (b) Transition between shear and tensile failure modes in a solid disk in the Brazilian disk test [36]*

As figure 3.1 illustrates, the strength of the material is increasing from inside of the tested specimen while the load is applied on the disk. The initial cracking points are located on the contacting surface of the specimen. The transverse direction refers to the vertical loading direction along the diameter of the specimen. If the rock or rock like material is homogenous, the straight line-like crack can be either single or double cracks in the disk center, and is developing along the vertical diameter. In the paper of Hadi Haeri et al., a detailed study indicated different crack propagation paths were formed from the coalescence of either one or two pre-existing cracks in the central area of the specimen [37]. It provides a theoretical foundation for the study of the formation of crack pattern in the damage zone of heterogeneous material under static or dynamic loading conditions, which will be explained in detail in chapter four.

In the study of Yong Yu et al., it was mentioned that the International Society for Rock Mechanics (ISRM) proposed the thickness to diameter ratio (T/D) of the specimen for the Brazilian disk tensile test to be around 0.5, assuming that the rock materials are homogeneous and linearly elastic. In addition, the National standards and specifications for rock tests in China suggested the T/D ratio can be in between of 0.5 and 1.0 [38]. Based on elasticity theory, Poisson's ratio has significant effect on the stress distribution in specimen. The stress concentration exists in the traditional Brazilian disk test, and a

high T/D ratio is involved according to Hudson et al [39]. So, in the study of Yong Yu et al., a T/D ratio of 0.2 was used to compare with the one used in the traditional method. More accurate measurement results were obtained in their modified test method. Furthermore, in the study of K.Kan et al., a comparison was done on the specimens with different geometrical dimensions through the Brazilian disk test. It is found that the diameter of the specimen has effect on the fracture toughness. The recommended thickness and diameter of the Brazilian disk was proposed too [40]. In addition, Abbass et al., indicated that the failure behavior of Brazilian specimens are not affected by their diameters with a constant thickness [41].

Therefore, based on the tested material and the strategy of the Brazilian disk test, a proper specimen is essential in order to conduct such a test. In this study, the Brazilian disk test is conducted at first, to verify whether the tested material is homogeneous or not, so that the following studies and tests can be processed smoothly. If the tested material is homogeneous, the cracking of the specimen will be vertically along the diameter. Therefore, the configuration of the tested specimens for Brazilian disk test is defined and shown in Figure 3.3, the size of the disk is 100 mm diameter by 30 mm thickness.

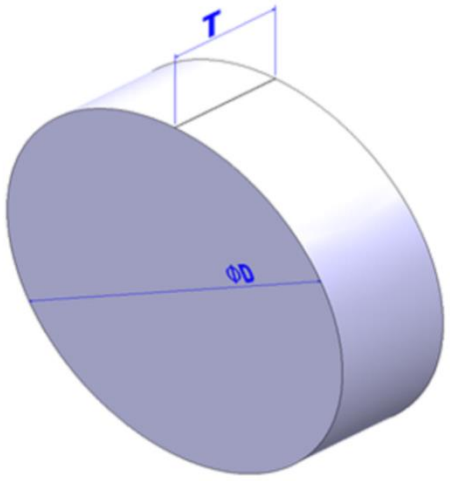

Figure 3.3. *Configuration of a specimen for Brazilian disk test (Diameter: 100 mm, thickness: 30 mm)*

In the Brazilian disk test, the compression that the specimen received consists of the tensile stresses that are perpendicular to the vertical diameter, are basically constant through the region around the center [36]. Based on the fact that the failure occurs at the point of maximum tensile stress, the indirect tensile strength of Brazilian disk test can be calculated. As the ASTM 2008 defined, which was mentioned in the study of Diyuan Li, the tensile strength σ_t (MPa) based on the Brazilian disk test is

$$\sigma_t = \frac{2P}{\pi DL} = 0.636\,\frac{P}{DL}\,, \tag{1}$$

where P is the compressive load at failure (N), D is the diameter of the disk (mm), and L is the thickness of the disk (mm) [36]. With the measured tensile strain ε_t (mm/mm), the Young's modulus of isotropic material of Brazilian disk test E (GPa) can be calculated by

$$E = \sigma_t / \varepsilon_t = \arctan \frac{y}{x}, \tag{2}$$

where σ_t is the tensile stress (MPa), εt is the tensile strain (mm/mm), $\arctan \frac{y}{x}$ represents the slope of strain-stress curve. The formula gives the relationship between E, σ_t and ε_t. Also, the Poisson's ratio can be calculated by the following formula

$$\nu = \varepsilon_v / \varepsilon_h, \tag{3}$$

where ε_v is the transverse strain (mm/mm), ε_h is the axial strain (mm/mm). The Young's modulus of Brazilian disk test will be compared with the one from the following three-point bending (3PB) test. The tested material is homogenous if and only if the corresponding values are the same.

However, in the thesis, the tested material might be not homogenous. In the study of Ye Jianhong et al., an interesting calculation for non-homogenous material in the Brazilian disk test was proposed [42]. With the equation (1), the stress distribution in Brazilian disk was presented in their study. As Figure 3.4 shows, when the stress concentration located at the region of point C or F on the disk, the represented σ_x, σ_y and τ_{xy} can be calculated with formula (4)

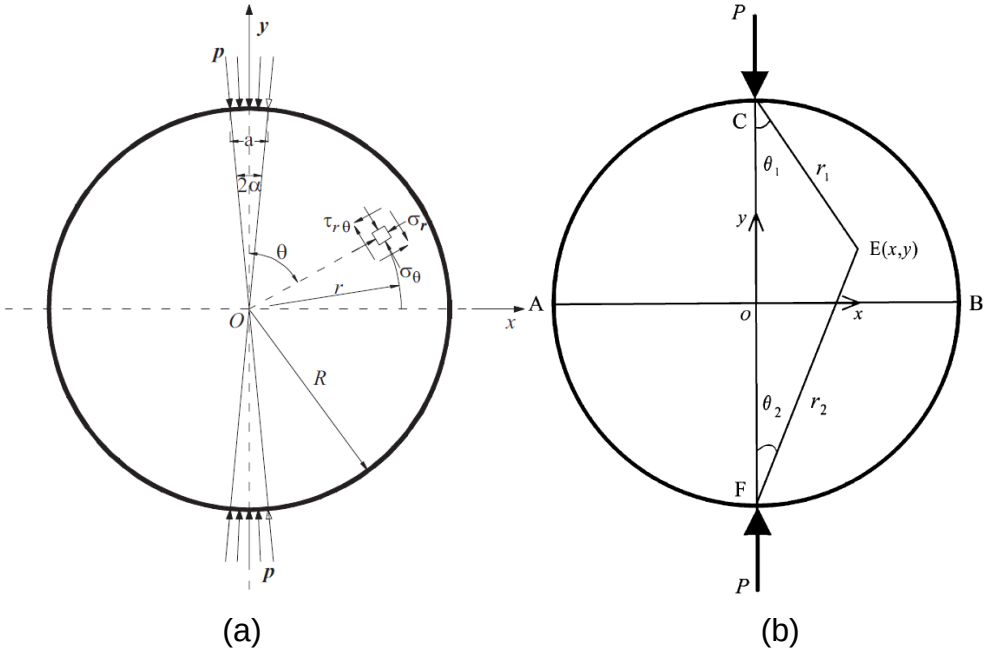

Figure 3.4. *(a) A pair of distributed load applies over an arc of the disk oppositely and diametrically on the disk; (b) A Brazilian disk subject to line load P [42]*

$$\sigma_x = \frac{2P}{\pi l}\left\{\frac{((D/2)-y)x^2}{(((D/2)-y)^2+x^2)^2}+\frac{((D/2)+y)x^2}{(((D/2)+y)^2+x^2)^2}-\frac{1}{D}\right\}$$
$$\sigma_y = \frac{2P}{\pi l}\left\{\frac{((D/2)-y)^3}{(((D/2)-y)^2+x^2)^2}+\frac{((D/2)+y)^3}{(((D/2)+y)^2+x^2)^2}-\frac{1}{D}\right\} \quad (4)$$
$$\tau_{xy} = \frac{2P}{\pi l}\left\{\frac{((D/2)-y)^2x}{(((D/2)-y)^2+x^2)^2}+\frac{((D/2)+y)^2x}{(((D/2)+y)^2+x^2)^2}-\frac{1}{D}\right\},$$

where P (N/m) is the line load applied. With the assumption of y=0 in above formula, τ_{xy} is 0, the stress concentration is along the diameter AB. Therefore, the tensile stress σ_x is half of the compressive stress σ_y at the center of Brazilian disk [42]. Due to the stress-strain curve sometimes shows of non-linearity in the test, the Young's modulus E can be obtained by

$$E_s = \frac{1}{2}\sigma_t / \varepsilon_t, \quad (5)$$

$$E_t = E_s\{(1-\frac{D}{L}\arctan\frac{2L}{D})(1-\nu)+\frac{2D^2(1+\nu)}{4L^2D^2}\} = A*E_s, \quad (6)$$

$$A = (1-\frac{D}{L}\arctan\frac{2L}{D})(1-\nu)+\frac{2D^2(1+\nu)}{4L^2D^2}, \quad (7)$$

where E_t is the Young's modulus of the specimen, E_s is defined as splitting Young's modulus that is obtained from the strain-stress curve in the Brazilian disk test, and A is a correction coefficient [42].

3.1.2. Three-point bending test and the configuration of the specimen

For the non-ductile monolithic ceramic material, the common direct tensile test is hard and costly to be conducted [43]. The process of holding specimen can break the specimen. The stiffness can also lead to some errors on bending stresses. Moreover, specimen preparation process needs to minimize machining damage and stress concentration [43]. Flexural strength (cross-breaking strength) is the maximum stress developed when a simple beam (bar-shape) is under a bending force. Three-point bending (3PB) test and four-point bending (4PB) test can be used in this case. However, 4PB test is used more often for the material which does not fail in the 3PB test [44]. By the load-deflection, in addition to the flexural strength, flexural strain, flexural stress-strain response, Young's modulus E (modulus of elasticity in bending) and yield point of materials can be obtained. Also the stiffness of the tested material can be indicated when it is flexed.

3PB test is mainly used for homogeneous materials. Because 3PB test is a widespread flexural strength test method, extensive researches are conducted on different materials, especially on composite materials, using this test method. Still, there are not many studies about the 3PB test on brittle materials like Al_2O_3, Macor and B_4C. Luca Collini et al., conducted Ring-on-Ring (RoR) biaxial bending tests and 4-point bending (4PB) tests on glass-ceramic, for the comparison of the statistical characterization of bending strength, and evaluating the influence of the static fatigue [45]. The authors show the similar test results of both RoR and 4PB tests in their research. In this paper, both Brazilian disk

test and 3PB test are chosen to identify the homogeneity of specimen materials by analyzing and comparing the similarity of the test results, in order to select the appropriate material that can be used for CLIC girder.

3PB test is performed on an universal testing machine with a three point bend fixture. In this test, a rectangular shaped specimen is placed on two mounted supporting cylinders which are parallel with each other on the test machine. The loading force is applied on the geometry center of the specimen by a loading cylinder. The loading cylinder is mounted but allowing its free rotation to the axis way as parallel as the cylinder axis and the specimen axis. The minimum thickness of the specimen for 3PB test is 0.25 mm. Based on this, the total length and width of the specimen can be hundreds times the thickness in different of ranges [46]. In this thesis, the 3PB test is applied with the assumption of homogeneous structure for B_4C, Al_2O_3 and Macor. In order to further analyze, the actual test results and the relevant simulation results are monitored. The geometry of the 3PB test is shown in Figure 3.2.

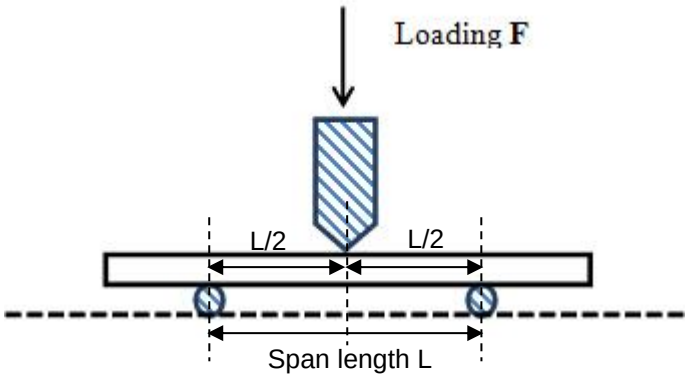

***Figure 3.2**. The geometry of the 3PB test (F: load; L: span length)*

According to ASTM C 293, the span length of the specimen is three times the thickness and the width. The load is applied in the middle of the span length, and both the supporting cylinders should be at least 25 mm from their closest ends [47]. Thus, in this study, the configuration and the size of the rectangle beam (120 mm length, 30 mm width and 30 mm height) for 3PB test are defined and shown in Figure 3.4.

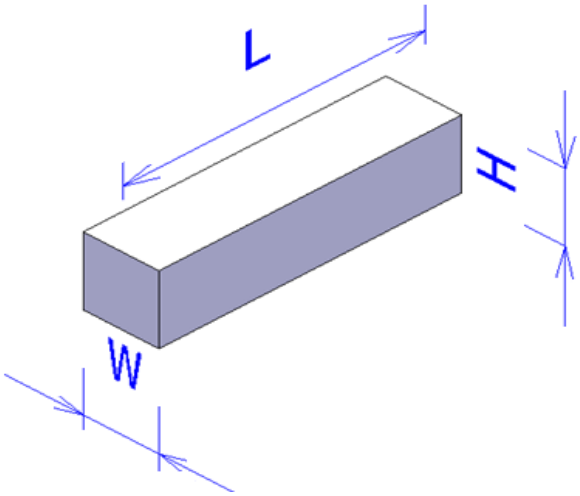

Figure 3.4. *Configuration of a specimen for 3PB test (L: 120 mm, W: 30 mm, H: 30 mm)*

In the 3PB test, the maximum flexural stress σ (MPa) can be obtained by

$$\sigma = My/I \,, \tag{8}$$

where M is the torque applied in the middle of the specimen, y is the distance from the center of the specimen to its convex surface (mm), I is the moment of inertia (mm^4). Because

$$M = PL/2 \,, \tag{9}$$

$$y = H/2 \,, \tag{10}$$

$$I = WH^3/12 \,, \tag{11}$$

Substituting formulas (9), (10) and (11) into Eq. (8), the flexural stress σ can be calculated by

$$\sigma = 3PL/WH^3 \,, \tag{12}$$

where W is the width of the specimen (mm), H is the height of the specimen (mm), and L is the length of the specimen (mm). With the equation (2), Young's modulus for 3PB test can be obtained.

In the experiment, the homogenous structure of the material is assumed. The mechanical tests for both Brazilian disk test and 3PB test are presented, measured, compared and analyzed in chapter five.

3.2. Procurement and Quality control

3.2.1. Procurement

When the candidate materials are defined, corresponding mechanical tests are scheduled. Supplier firms are investigated to produce the needed material specimens. Initially, several suppliers are picked for each material type. After market consultation, production

possibilities investigation and the price surveys, orders are placed promptly. Five specimens of each tested material from different firms are ready for tests. The specimen quantities are listed in Table 3.1.

Table 3.1. *Quantities of specimens*

Materials	Quantity of specimens for Brazilian disk test	Quantity of specimens for 3PB test
B_4C	5 disks	5 bars
Al_2O_3	5 disks	5 bars
Macor	5 disks	5 bars

3.2.2. Inspections and Measurements

Before conducting the dimensional acceptance check, a visual inspection is performed. For the 15 disks and the 15 bars, no cracks were visible on the surface. However, the edges of the disks are not chamfered, so few minor dents are dispersed on the disk edges.

Dimensions of each specimen are measured with Mitutoyo callipers (range 0-150 mm), with accuracy of two decimal places. Because there are no pre-defined tolerances for the dimensions of the specimen, the basic dimension of the geometrical product has to comply with ISO-2768-1 [48]. "General tolerance from standard machining tolerance" [49] and "Linear dimensions of ceramic-metal seals" [50] are also referred. As described, the tolerance for the length excludes the chamfered areas. The "coarse class", allowed by ceramic manufacturing technology, is referred. In this thesis, the tolerance of ±0.2 mm for dimensions of 12.7 mm to 76.2 mm is used. Likewise, tolerance of ±0.3 mm for dimensions of 76.2 mm to 152.4 mm is applied.

Before any measurement, B_4C, Macor and Al_2O_3 are named as B, M and A respectively. Five measurements for each specimen are taken in a way to average the dimensional measurements, and the verified mean value dimensions of the specimens are shown in Tables 3.2 and 3.3.

Table 3.2. *Measurement results of specimens for Brazilian disk test (mean value)*

	B1	**B2**	**B3**	**B4**	**B5**
D (mm)	100.13	100.14	100.10	100.10	100.05
H (mm)	29.96	30.15	29.96	29.96	30.14
	M1	**M2**	**M3**	**M4**	**M5**
D (mm)	100.16	100.14	100.11	100.13	100.14
H (mm)	30.20	30.19	30.20	30.18	30.19
	A1	**A2**	**A3**	**A4**	**A5**
D (mm)	100.15	99.81	99.91	100.02	99.96
H (mm)	30.15	29.99	30.09	30.06	30.03

Table 3.3. *Measurement results of specimens for 3PB test (mean value)*

	B1	**B2**	**B3**	**B4**	**B5**
L (mm)	120.05	120.03	120.03	120.03	120.03
W (mm)	30.16	30.17	30.01	30.16	30.01
H (mm)	30.11	30.09	30.12	30.90	30.09
	M1	**M2**	**M3**	**M4**	**M5**
L (mm)	120.14	120.20	120.18	120.15	120.18
W (mm)	30.17	30.18	30.18	30.15	30.15
H (mm)	30.16	30.17	30.17	30.17	30.17
	A1	**A2**	**A3**	**A4**	**A5**
L (mm)	120.10	120.07	120.01	120.07	120.06
W (mm)	30.02	30.02	30.02	30.00	29.95
H (mm)	30.03	30.03	30.00	30.01	30.02

As the general tolerances are selected, the results from above tables are all in the range of the corresponding tolerances. Therefore, all specimens can be tested under mechanical destructive experiments (Brazilian disk test and 3PB test).

4. SIMULATION AND MECHANICAL TESTING

Simulations of the mechanical tests are performed before the experiments. The simulation results help to understand the testing mechanics on the subject. Also the comparisons between the simulation results and the mechanical testing results are studied, in order to see whether they are in good accord with each other or not. This chapter introduces the ANSYS simulations of the mechanical tests. In addition, the related Brazilian disk test and 3PB test are presented. In the thesis, mechanical tests (Brazilian disk test and 3PB test) take place at the National Technical University of Athens (Greece) in the framework of the CLIC-NTUA collaboration of CERN. Furthermore, the comparison between the theoretical part of the tests and practical explanation can be linked together. The processing of the testing data and the corresponding result analysis are presented in the forthcoming chapter five.

4.1. Description of ANSYS simulation software

ANSYS software is an engineering simulation package, known as Computer-Aided Engineering (CAE), and it has been available since 1970 [51]. So far, ANSYS is widely used in automotive, aerospace, energy, materials and chemical processing, academia, civil engineering, electronics consumer products and other industries by designers, engineers, analysts, managers, executives and others. It is an excellent platform for analyzing broad effects, connecting the results and input together to study structural mechanics, multi-physics, fluid dynamics etc. It integrates all requirements in one platform [51]. In the thesis, ANSYS simulation is involved for simulating the mechanical test results and comparing with the results of practical mechanical tests which are conducted later. With the simulation results, the possible failures could be found out before the real test begins.

4.2. Material Experiments

To determine the mechanical properties of a solid or quasi-solid material (such as metal, ceramic, polymeric material), a standard test method is the first choice. Mechanical testing shows the elastic and inelastic behavior of the tested material under various temperature, tension, compression and loading conditions [52]. It indicates information about whether a material is suitable for its intended mechanical application by measuring different properties. The measured properties are tensile strength, elasticity, elongation, hardness, impact resistance, stress rupture, fatigue limit and fracture toughness. In addition to the above properties, compressive strength, ductility, flexural modulus, shear modulus and shear strength are also measured [52]. Meanwhile, as mentioned in chapter

three, mechanical properties like Young's modulus and Poisson's ratio can also be obtained. By this way, mechanical experimentation can help companies design products perform as expected [53].

For the experiments, a series of mechanical testing methods can be chosen, such as Brazilian disk test, 3PB test, 4PB test, uniaxial compression test, coaxial double ring bending test. Products made of the three proposed candidate materials are not yet ascertained to have homogenous structure. Therefore, the Brazilian disk test is selected to confirm the structure composition of each material. Afterwards, 3PB test is conducted in this study.

4.3. Simulation and Brazilian disk test

4.3.1. Simulation of Brazilian disk test

The simulation of Brazilian disk test started with the creation of a 3D geometry according the defined configuration (100 mm diameter and 30 mm thickness). Two symmetrical test surfaces were created on the surface where the force and the support would be applied on. The dimension of both contact surfaces (one for loading, and the other for the fixed support) is 10 mm × 30 mm, as Figure 4.1 shows.

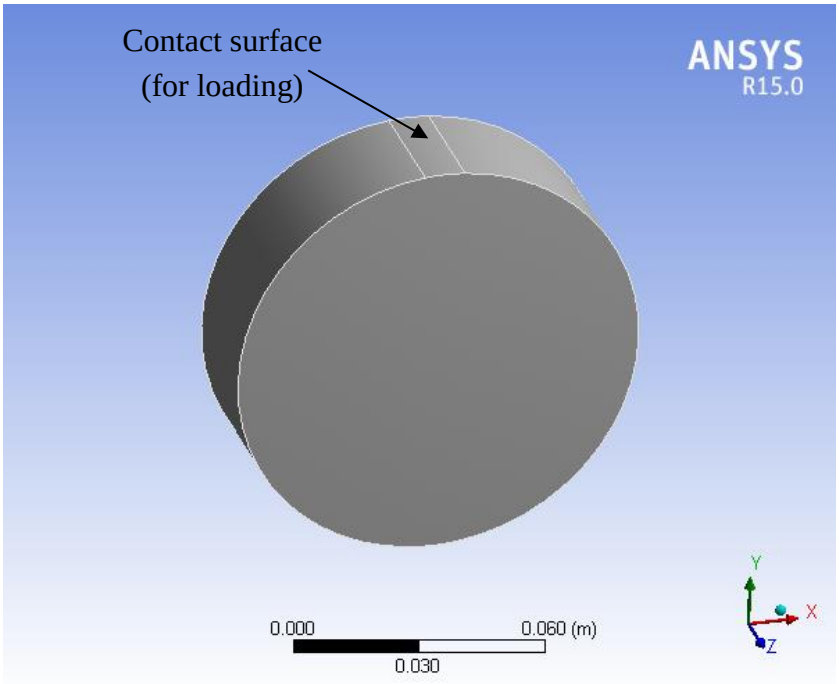

Figure 4.1. *Geometry of the Brazilian disk test simulation*

After choosing the corresponding material, the coordinate system was built. The geometry was meshed, and boundary conditions were inputted. The simulation parameters of B_4C, Macor and Al_2O_3 of Brazilian disk test are listed in Table 4.1.

Table 4.1. *Simulation parameters of mechanical tests*

Materials	B_4C	Macor	Al_2O_3
Environment Temperature (°C)	22	22	22
Unit System	Metric (mm, kg, N, s, mV, mA) Degrees rad/s Celsius		
Density kg mm^-3	2.48e-006	2.52e-006	3.81e-006
Coefficient of Thermal Expansion	5.6e-006 C^-1	9.3e-006 C^-1	7.6e-006 C^-1
Reference Temperature (°C) of CTE	1000	300	227
Young's Modulus (MPa)	4.6e+005	6.69e+004	3.7 e+005
Poisson's Ratio	0.17	0.29	0.22
Bulk Modulus (MPa)	2.32e+005	5.31e+004	2.20 e+005
Shear Modulus (MPa)	1.97e+005	2.59e+004	1.52 e+005

Based on the boundary conditions previously set, the simulations are conducted at room temperature, 300 kN and 30 kN loads are applied respectively on the specimens of B_4C, Macor and Al_2O_3. By applying two different loading conditions on specimens, the total deformations of B_4C, Macor and Al_2O_3 are shown in Figures 4.2, 4.3 and 4.4. The equivalent strains and the equivalent stresses of B_4C, Macor and Al_2O_3 are listed accordingly in Table 4.2.

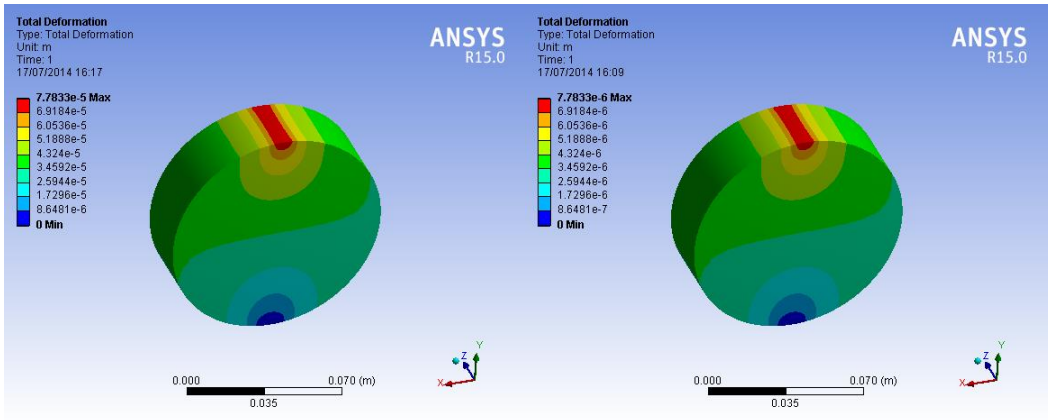

Figure 4.2*. Total deformation of B_4C (Load: left-300 kN, right-30 kN)*

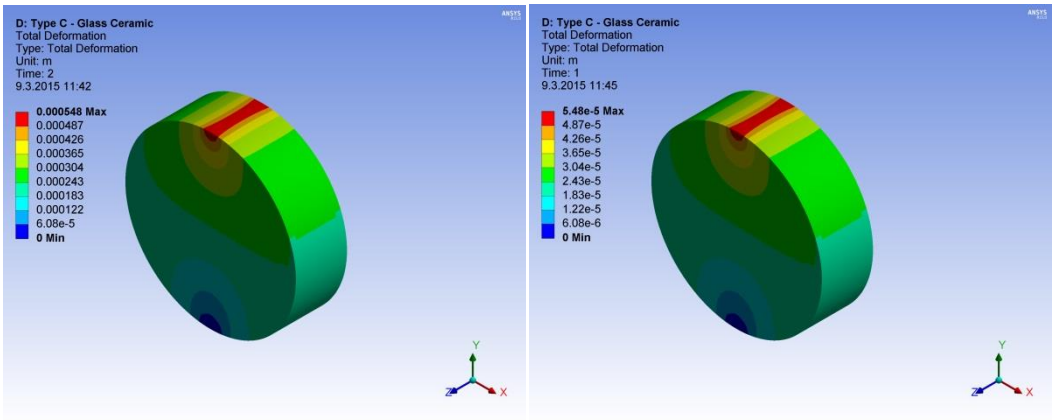

Figure 4.3*. Total deformation of Macor (Load: left-300 kN, right-30 kN)*

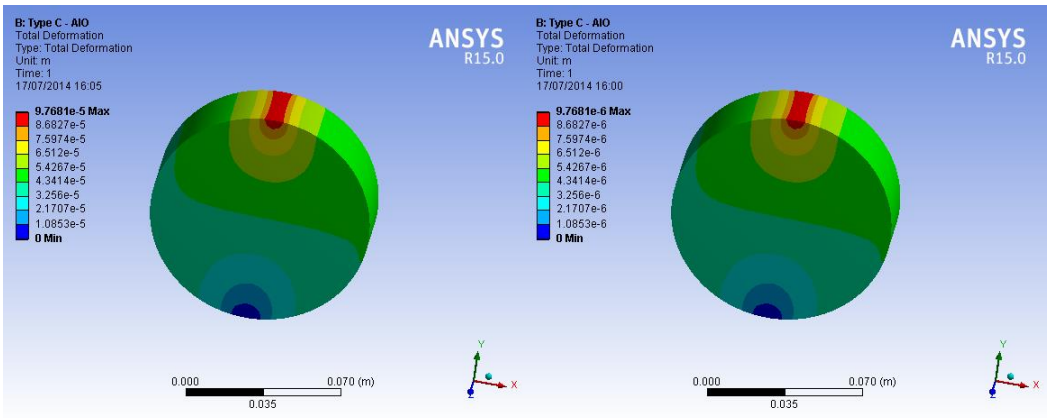

***Figure 4.4**. Total deformation of* Al_2O_3 *(Load: left-300 kN, right-30 kN)*

Figures 4.2-4.4 illustrate the deformation status of the tested materials in Brazilian disk tests under the corresponding static loading conditions. The maximum deformation occurs on the top contacting surface of the specimen, and then the deformation is extended towards the bottom of the disk, while the symmetric bottom contacting area is fixed and has no deformation before material fail. It also reveals that the stress concentration implodes on the top surface of the specimen when the load is applied. Together with the actual mechanical test results, which are introduced later, the simulation and the mechanical test results correspond to the study of W.C.Zhu at al., which is about the failure process of a heterogeneous rock disk in Brazilian disk test under static and dynamic loading conditions [54]. The authors studied the rock fracture process by using a Rock Failure Process Analysis (RFPA). An illustration of the theoretical and numerical results of the stresses distribution across the loaded diameter of the specimen under the loading is shown in Figure 4.5. The initiation of fractures and the propagation processes can also demonstrate the disk failure mechanism for further understanding the microstructural behavior of the tested material at different loading conditions. The disk failure mechanism under the loading is presented in Figures 4.6 and 4.7 [54].

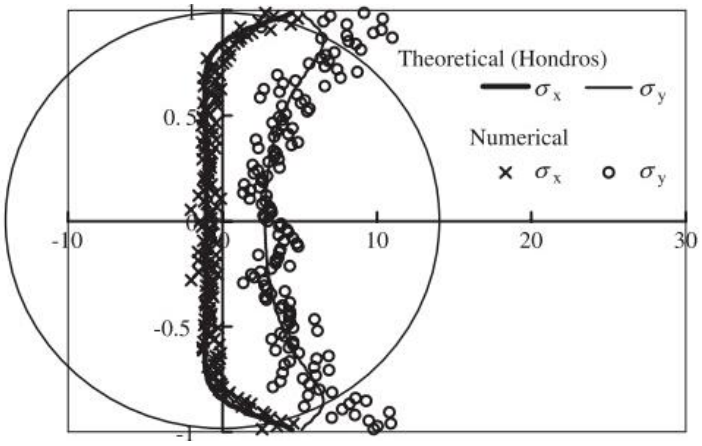

***Figure 4.5** Theoretical and numerical results of stresses distribution across loaded diameter for disk specimen under indirect test [54].*

As it is shown in Figure 4.5, an elastic rock specimen is under a static loading at the beginning. The tensile stress distribution locates at the central area and along the vertical diameter of the specimen. The numerical results are in accord with the theoretical results. However, the numerical results undulate around the theoretical curves because of the heterogeneity of the material. If the elastic rock specimen is under a dynamic loading, spalling occurs when an incident compressive stress wave reaches to twice of the tensile strength of the material. Furthermore, a fraction of the tensile wave passes through the failure point and continually goes through the specimen when the material fails. At some point, it also initials other spalls [54].

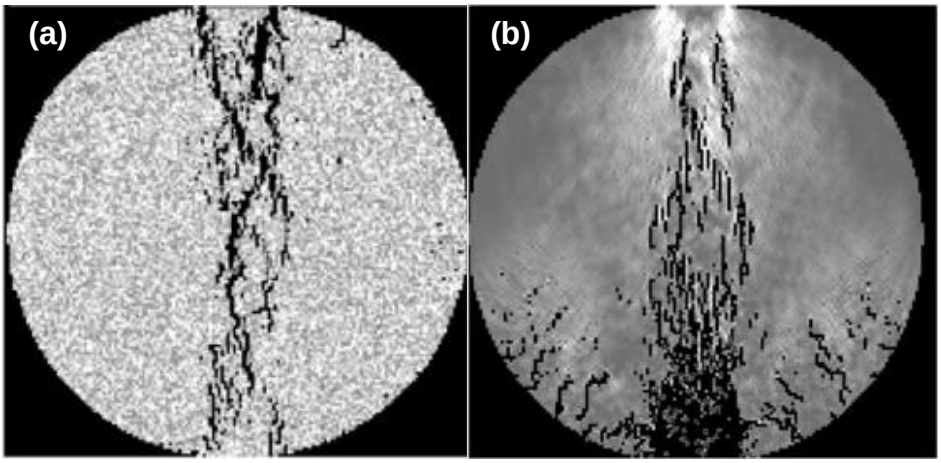

Figure 4.6 *Failure statues (cracking pattern) of rock disks: (a) Under static loading; (b) Under dynamic loading [54]*

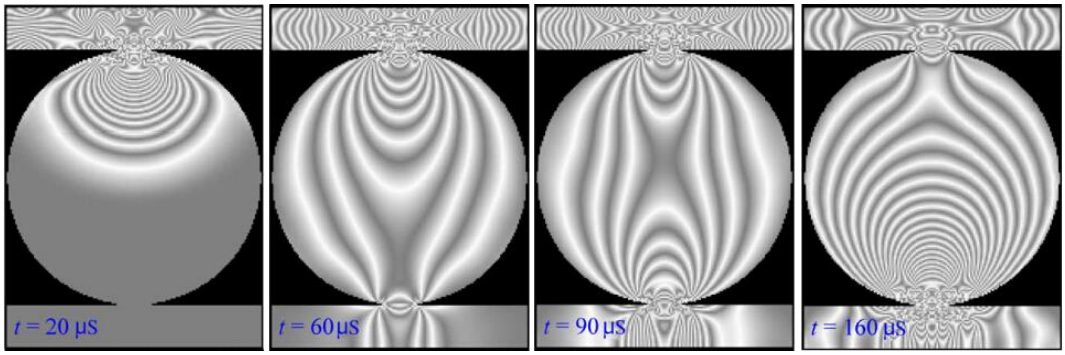

Figure 4.7 *The photo-elastic fringes of the maximum shear stress of a homogeneous rock specimen under a dynamic compressive stress wave in elastic stress field [54]*

From figure 4.6, the cracking patterns of rock disks under a static and a dynamic incident compresses are different. Under the static loading, the failure is around the vertical diameter of the disk, also a damage zone is expended in a region that is near the vertical diameter. It can also be seen that a primary crack pattern along the vertical diameter of the disk is formed of many damaged elements by joining together in the damage zone. It is because the first element is damaged around the vertical diameter of the disk under tension, and the increased external loading propagates the tensile damage of many ele-

ments [54]. Besides, the subordinate cracks around the diagonal lines are growing too. Comparing with the results of homogeneous material, the heterogeneity of the test material leads a non-straight line of the primary crack [54]. Under the dynamic loading, different stress waves are involved; accordingly, various cracking patterns of the rock disk are noticed. The stress distribution appears in a similar way than it is under the static loading, at the beginning. As the dynamic loading continues, the compressive stress wave increases because of the stress wave reflection, and more cracks are initiated around the bottom side of the disk. Hereafter, the cracks generate and grow upward along the vertical diameter of the disk. Additionally, a lot of cracks are initiated and scattered radially around the bottom half of the disk. Hence, the failure pattern and failure mechanism of the disk have strong relevance to the propagation of the stress wave. Therefore, the disk specimen is more fractured than under the static loading [54].

The stress distribution in the homogeneous material seems to be the same as in a statically loaded specimen initially. In order to understand the stress wave propagation in heterogeneous rock disk under the dynamic loading, the stress wave propagation in the homogeneous rock disk is demonstrated with photo-elastic fringes of maximum shear stress at different times in the study of W.C.Zhu et al [54]. As shown in Figure 4.7, the authors indicate the elastic stress wave, whose reflection initiates the failure pattern, can be periodically distributed in the rock disk. For each cycle, the stress wave goes through the rock disk from the tip end of the crack, and partially reflects back into the rock disk, and partially transmitted into the fixed steel plate. The changing waves are periodically, but the stress distribution is irregular, because the location of the maximum stresses is shifted in the disk. In the process, the stress wave propagates downwards and arrives at the bottom of the rock disk in one cycle [54].

Table 4.2. *Simulation results of Brazilian disk tests*

Material	**300 kN of Loading**			**30 kN of Loading**		
	Max Deformation (mm)	Equivalent Stress (MPa)	Equivalent Strain (mm/mm)	Max Deformation (mm)	Equivalent Stress (MPa)	Equivalent Strain (mm/mm)
B_4C	0.078	1353.6	0.0033	0.0078	135.36	0.00033
Al_2O_3	0.098	1338.7	0.0041	0.0098	133.87	0.00041
Macor	0.55	1319.6	0.022	0.055	131.96	0.0022

Figures 4.2-4.4 show that the maximum total deformations of B_4C, Al_2O_3 and Macor are 0.078 mm, 0.098 mm and 0.55 mm under 300 kN loads, and 0.0078 mm, 0.0098 mm and 0.055 mm under 30 kN loads correspondingly. Table 4.2 summaries the simulation results of three candidate materials. It can be seen that the Macor has the biggest maximum deformation and the biggest equivalent strain among three tested materials under the same loads (0.55 mm and 0.022 mm/mm under 300 kN, and 0.055 mm and 0.0022 mm/mm under 30 kN respectively), while B_4C has the smallest values. In addi-

tion, Macor has the smallest equivalent stress (131.96 MPa under 30 kN) among three materials, while B_4C has the biggest one (135.36 MPa under 30 kN). The simulation results present that the Macor is more brittle than B_4C and Al_2O_3, and can endure less load than the two others. Furthermore, with the same geometry and under the same load, equivalent stresses of three tested materials are different. Young's modulus is defined by the stress σ and the strain ε, as expressed in the formula $\sigma = E * \varepsilon$. Thus, materials with different Young's modulus have different stresses under the same loading condition. Moreover, the deformation per unit length is not the same; even though the pressure per unit area of the material is the same.

4.3.2. Brazilian disk test and analysis

It is unsure that the three candidate materials (B_4C, Al_2O_3 and Macor) are homogenous materials. Therefore, the Brazilian disk test is the first mechanical test to be conducted so as to verify if the assumption of homogenous material is valid. According to the simulation results, Macor has been proven as the weakest material among three candidate materials.

In the experiment, a INSTRON 30 TON machine is used for both Brazilian disk test and 3PB test. The static load of this machine is 100 kN. As the Brazilian disk test is the most popular substitute method for acquiring the direct tensile strength of brittle materials, a standardized test method, proposed by the ISRM, is selected. One of the typical Brazilian tensile test loading configurations with curved loading jaws is shown in Figure 4.8 [36]. In the study of Diyuan Li et al., the configuration with curved loading jaws is more stable for Brazilian disk test than the different types of flat loading platens. It is also easy to align the geometric center of the specimen with the center of the curved loading jaws, so that the compressed load goes through both centers along the vertical direction can be verified [36]. Although, based on a preliminary study, a possible curve-to-plane contact problem of Brazilian curved loading configuration is discussed and needs to be further studied in the paper of S.K.Kourkoulis et al., even there is only a very small difference between the parabolic and the circular distributions [55]. However, no perfect smooth surface exists. A very recent study which is also from S.K.Kourkoulis et al. shows that the curve-to-plane contact problem mentioned previously could be proved to be useful for the case of non-perfectly smooth surfaces [56].

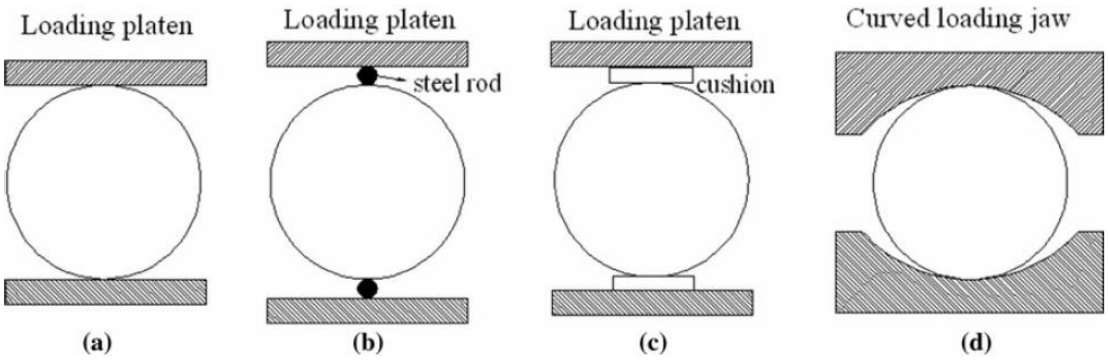

Figure 4.8. *Typical loading configurations for Brazilian disk test: (a) Flat loading platens, (b) Flat loading platens with two small-diameter steel rods, (c) Flat loading platens with cushion, (d) Curved loading jaws [36].*

Before starting the test, the geometric center of each specimen is measured and retrieved. The center is used for the definition of the position of the HBM triple strain gauges. The strain gauge is used for acquiring the experimental data (strains, stresses and deformations) from each specimen that is under testing, as a data acquisition sensor. A triple strain-gauge rosette and an electro strain-gauge are positioning on each specimen with ±1 mm of accuracy. The method of measuring Young's modulus in Brazilian disk test is proposed in the study of Ye Jiang et al., as shown in Figure 4.9. To measure the tensile deformation of the center of the disk, a strain gauge is stuck at the center O on the side face of the disk, along the direction that is perpendicular to the loading direction. A force sensor is used to record the applied load. With the stress-strain acquisition system, the stress and strain data are acquired [42]. Then, the Young's modulus can be resolved by using the computer processing system.

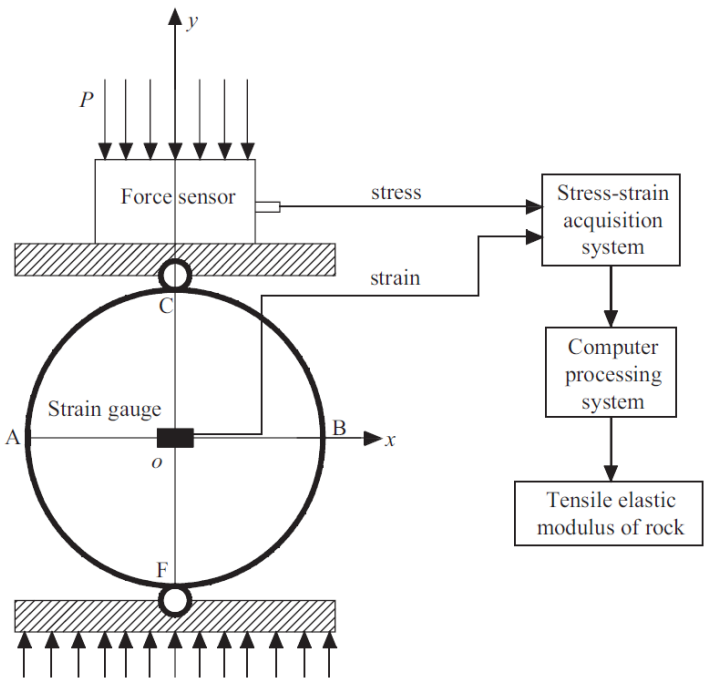

Figure 4.9. *The method of measuring tensile elastic modulus of Brazilian disk [42]*

Table 4.3 *HBM gauge categories*

HBM Categories		**Indicative CTE**
Category 1	ferritic steel	11 - 10 (10^{-6} in./in.*/°C)
Category 3	aluminum	25 - 21 (10^{-6} in./in.*/°C)
Category 5	austenitic steel	18 - 16 (10^{-6} in./in.*/°C)
Category 6	quartz	0.59 (10^{-6}/°C)
Category 7	titanium / gray cast iron	13 - 09 (10^{-6} in./in.*/°C)
Category 8	plastic material	/
Category 9	molybdenum	06 - 05 (10^{-6} in./in.*/°C)

To conduct the test precisely, appropriate strain gauge material is essential, and it has to be determined based on the property of the tested material. The similar Coefficient of Thermal Expansion (CTE) of material can help to select the proper HBM gauge material. The HBM gauge categories and the indicative CTE are listed in Table 4.3 [57]. According to the CTE of each tested material, B_4C and Al_2O_3 can be categorized based on category 9 - molybdenum, while Macor is under the category 7 – titanium / gray cast iron. Thus, the proper category of HBM strain gauge for each material under the working temperature is categorized, and the appropriate strain gauge used in the test is defined before the test start.

Each HBM triple strain gauge has to be connected with an electronic bridge by welding with a solder wire. Three strain sensors from equivalent different directions (sensor c-horizontal, sensor a-vertical and sensor b-45°) are contained within each HBM triple strain gauge, as Figure 4.7 shows. Correspondingly, three channels from the electronic bridge are connected with sensors *a*, *b* and *c*, in order to obtain the vertical strain, horizontal strain and the strain from 45°. The corresponding gauge factors are 2.01±1.0% for sensor *a*, 2.05±1.0% for both sensor *b* and sensor *c*. The connection between the electronic bridge and the HBM triple strain gauge, and the orientation of sensors *a*, *b* and *c* are shown in Figure 4.10. The strain gauge has to be glued on the geometric center of each specimen, and polymerized for at least 24 hours before the test starts. The data sheet of HBM strain gauge is attached in Appendix 3.

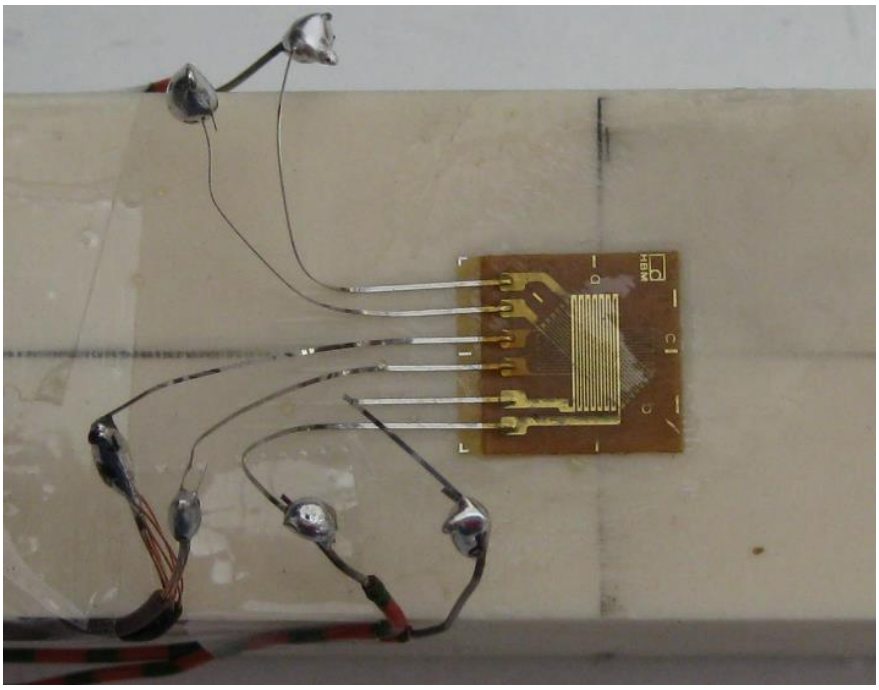

Figure 4.10. *The connection and orientation of the sensors of the HBM triple gauge*

Five Macor specimens are named accordingly as M1, M2, M3, M4 and M5. Five Al_2O_3 and five B_4C specimens are named in the same way (as A1, A2, A3, A4, A5, B1, B2, B3, B4 and B5 correspondingly). Then the specimen with the glued gauge is placed on a curved loading jaw. To ensure the testing result is successful, the orientation of the sensor *a* is parallel with the vertical diameter of the disk and the center of the curved loading jaw. Both centers of the disk and the curved loading jaw have to be on the same line. Meanwhile, the sensor *c* is positioned in parallel to the test platform (which means perpendicular to the vertical diameter of the disk and the sensor *a*), as shown in Figure 4.11 (c). The drawing lines on the specimen are helping to position the tested specimen to the curved loading jaw. The stages of the specimen preparation are presented in Figure 4.11.

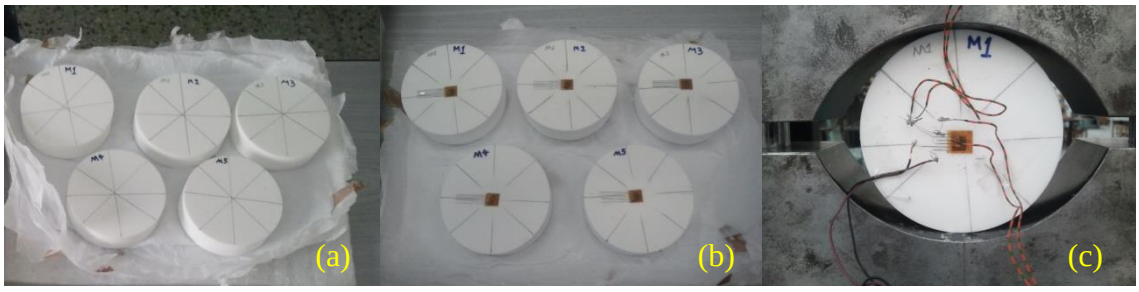

Figure 4.11 *Specimen preparations: (a) Calculation of the geometry center of each specimen, (b) Specimen with the glued strain gauge, (c) Final position of the specimen on the testing bed*

To simulate a static load, the loading speed is defined at 0.02 mm/min with the help of a computer. The testing machine, the electronic bridge (for data acquisition) and the testing PC are connected with each other, as Figure 4.12 shows. Low speed can reduce the instant impact of rupture to the specimens.

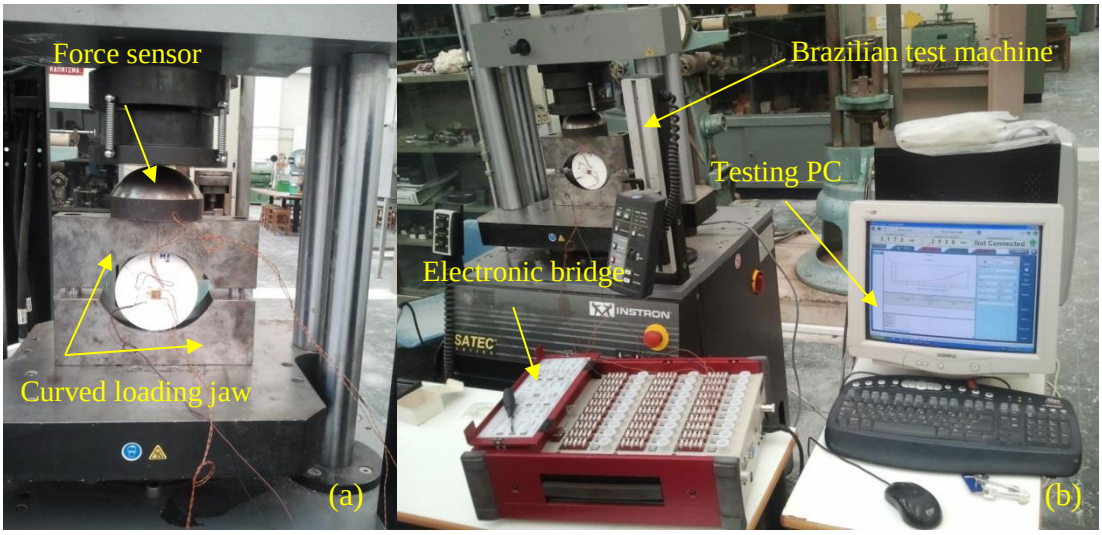

Figure 4.12 *Brazilian disk test equipment: (a) Brazilian disk test machine with curved loading jaws, (b) Brazilian disk test machine, electronic bridge and testing PC*

When the load is approximately 110 kN for M1, the tested specimen is ruptured. For M2, M3, M4 and M5, the maximum loads are measured to be 138 kN, 136 kN, 138 kN and 133 kN respectively. The corresponding pictures are shown in Figures 4.13 and 4.14.

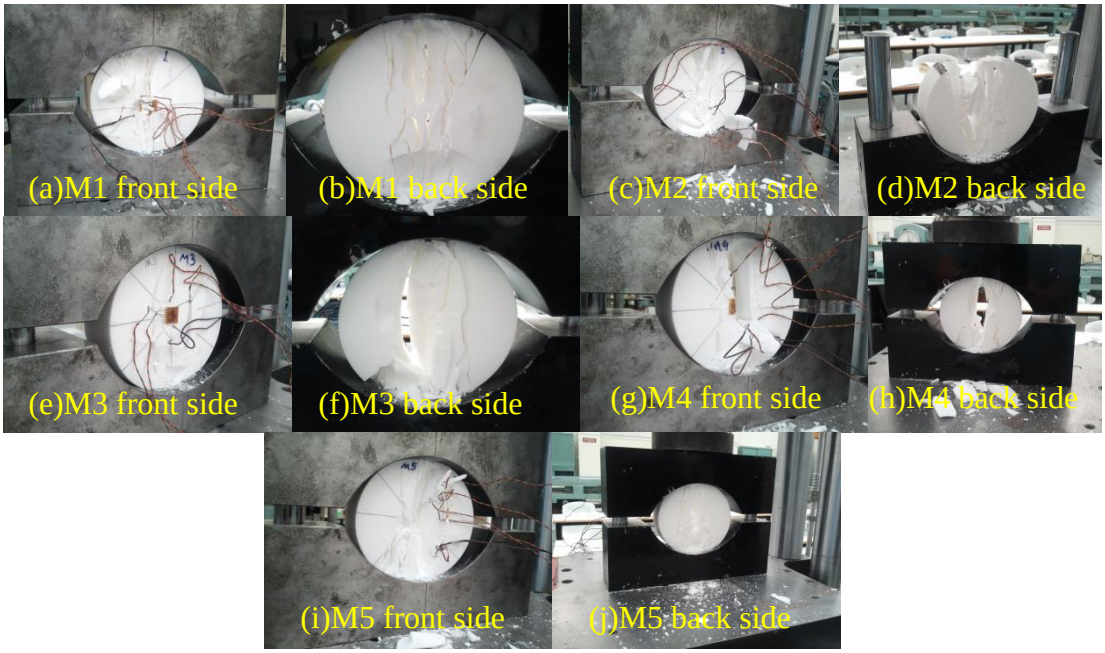

Figure 4.13 *The failure status of five Macor specimens*

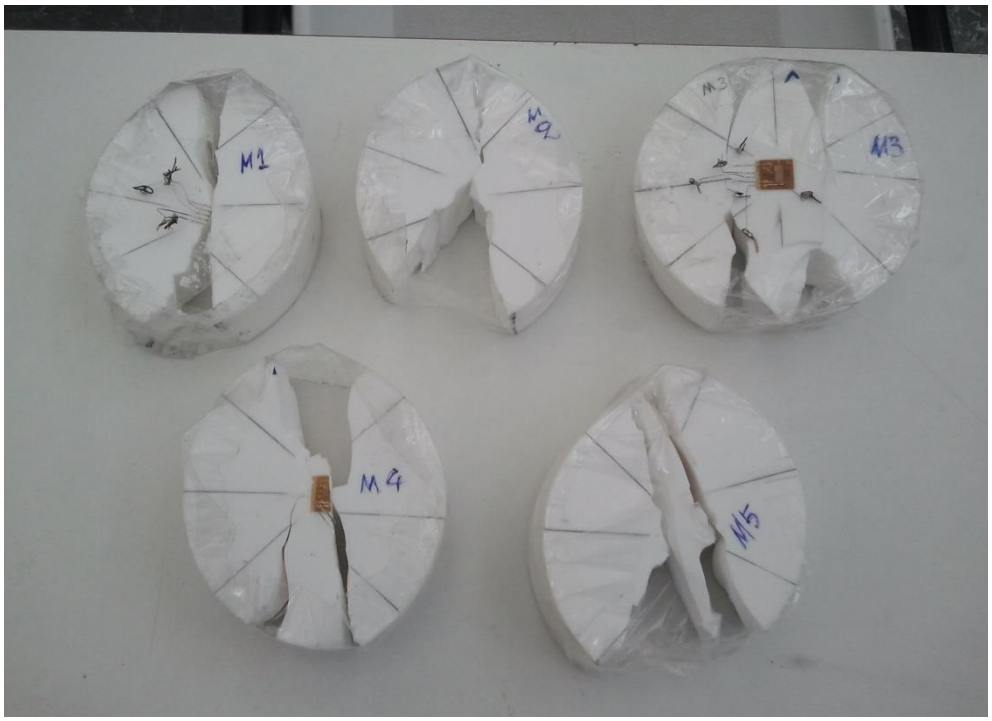

Figure 4.14 *Five fractured Macor specimens*

Figures 4.13 and 4.14 demonstrate the cracks of five M specimens. The crack patterns correspond to the numerical simulation result, the fracture process and the disk failure mechanism which were presented previously. It is obvious that the fracture crack is not a straight line along the vertical diameter of the disk, and the damaged region has been proved to be near the vertical diameter of the disk. Due to the stress concentration and the propagation of the damaged elements, the damages are initiated from the center of the disk, then extend outwards of the vertical diameter. Besides, there are many micro-cracks dispersed on each specimen because of the heterogeneity of the Young's modulus, as mentioned before. All of the above have explained that the Macor is a heterogeneous and massively porous material.

Followed by Al_2O_3 (A1), the failure does not take place until the static load reaches around 160 kN, which is over the static loading capability of the machine (100 kN as mentioned before). Therefore, the Brazilian disk tests for Al_2O_3 and also for B_4C are then stopped. In order to continue the tests in the future, a machine with a large load capability is needed for such a testing phase. However, the testing feasibility and the tight schedule limit the processed Brazilian disk test. So, in the current study, only Brazilian disk test on Macor is performed.

In spite of that, previously acquired data for Epument specimens of two different sizes in the Brazilian disk test are available (D=190 mm, H=61 mm and d= 104 mm, h=30 mm). The measurement results of large Epument disks and small Epument disks are listed in Table 4.4. From the measurement results, all specimens are accepted for Brazilian disk test.

Table 4.4. *Measurement results of Epument specimens with two different sizes in Brazilian disk test (mean value) (B: large; S: small)*

	BR-B-1	**BR-B-2**	**BR-B-3**	**BR-B-4**	**BR-B-5**
D (mm)	189.68	189.77	190.02	189.68	189.73
H (mm)	61.34	61.79	62.40	61.62	61.79
	BR-S-1	**BR-S-2**	**BR-S-3**	**BR-S-4**	**BR-S-5**
D (mm)	104.79	104.86	104.78	104.74	104.78
H (mm)	30.99	31.02	30.20	30.90	31.16

Figure 4.15. *Two different sized Epument disks after Brazilian disk test*

Figure 4.15 presents the fracture patterns of all tested specimens of two different sizes. All the fracture patterns on the specimens show line-like cracks along the vertical diameter of each disk. Those line-like cracks around the disk center comply with the crack pattern of homogeneous material which was described in previous chapter. Although, there are some micro-cracks are around the primary crack line. Therefore, Epument can be seen as homogeneous like material. Moreover, Macor is compared with Epument in this thesis. The detailed analysis is presented in chapter five.

4.4. Simulation and Three-point bending test

4.4.1. Simulation of three-point bending

The simulation of a 3PB test, similar to the Brazilian disk test, started with creation of a 3D geometry according to the defined configuration: 100 mm length, 30 mm height and 30 mm width. Three tested surfaces were created on the top and the bottom sides where the force and the supports would be applied on. The dimension of three contacting sur-

faces (one for loading, and the other two for fixed supports) is 20 mm × 30 mm, as Figure 4.16 shows.

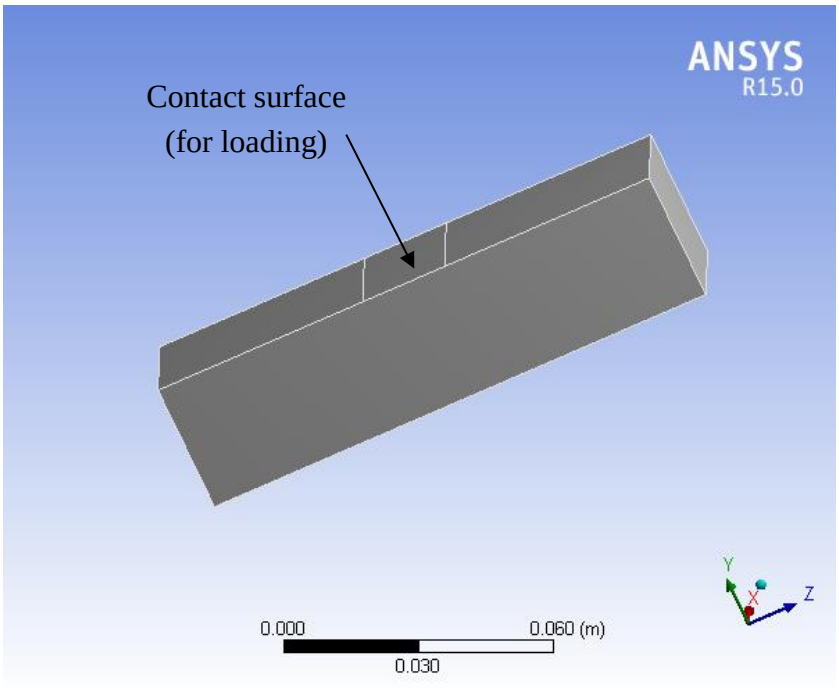

Figure 4.16. *Geometry of the 3PB test simulation*

In the same way as the simulation of the Brazilian disk test, the coordinate system was built after choosing the corresponding testing material. The meshing was generated on the geometry with the input boundary conditions. The simulation parameters of B_4C, Macor and Al_2O_3 of 3PB test are the same as listed in Table 4.1. Likewise, the 3PB experiments are conducted at room temperature, 300 kN loads and 30 kN loads are applied on the specimens correspondingly. The total deformations of B_4C, Macor and Al_2O_3 in the 3PB simulation test are shown in Figures 4.17, 4.18 and 4.19.

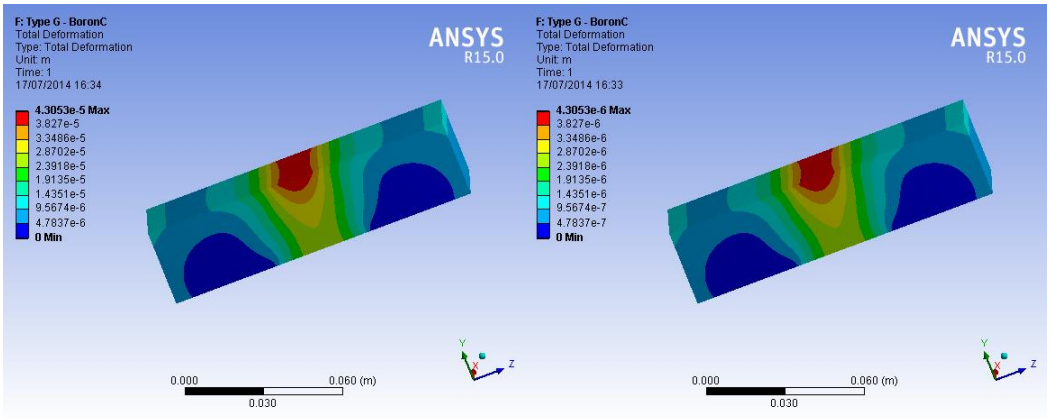

Figure 4.17*. Total deformation of B_4C (Load: left-300 kN, right-30 kN)*

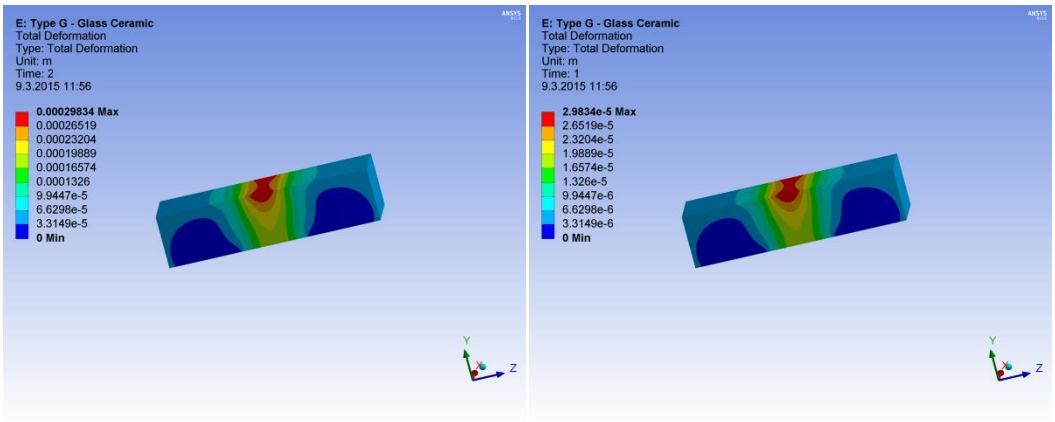

Figure 4.18. *Total deformation of Macor (Load: left-300 kN, right-30 kN)*

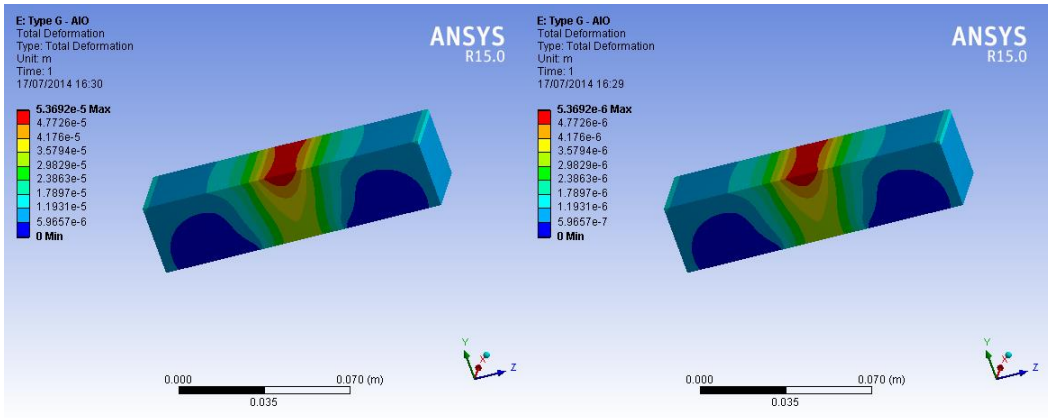

Figure 4.19. *Total deformation of Al_2O_3 (Load: left-300 kN, right-30 kN)*

Foreseeing the realistic crack path and the load carrying capacity of a homogeneous material is easily to be achieved in design. For heterogeneous like material, the realistic crack path and the cracking mechanism are complicated to predict. Many studies are conducted on heterogeneous asphalt mixture beam through the 3PB test for studying the cracking mechanisms and the fracture characteristics of the tested materials. Guowei Zeng et al., applied numerical simulations and described the trends of the central crack and off-center cracks in an asphalt mixture beam, and also explained the reason of the fracture [58]. Anyi Yin et al., also conducted simulation and explained deeply about the relations between the coarse distributions and the crack path trends [59]. Moreover, the distribution of microcracks before the crack propagation, the crack propagation process and the crack path with different offset distances were explained clearly by the authors [60]. The above mentioned methodologies can be useful for current study of B_4C, Al_2O_3 and Macor.

Figures 4.17-4.19 illustrate that the maximum deformation starts from the mid-span area, the tip of the crack, where the stress concentration is located. At this point, the stress and the strain are the highest. After that, the fracture is propagated along the initial crack in the vertical direction of the beam. Thus, damage accumulation is the main rea-

son to form the final fracture directly. The crack propagation of the specimen should be stable and the propagation path should be straight under a constant loading.

The maximum total deformations of B_4C, Macor and Al_2O_3 are 0.043 mm, 0.298 mm and 0.054 mm under 300 kN loads, and 0.0043 mm, 0.0298 mm and 0.0054 mm under 30 kN loads respectively, as shown in figures 4.17-4.19. The equivalent strains and the equivalent stresses of B_4C, Macor and Al_2O_3 are summarized accordingly in Table 4.5.

Table 4.5. *Simulation results of 3PB test*

Material	***300 kN Loading***			***30 kN Loading***		
	Max Deformation (mm)	Equivalent Stress (MPa)	Equivalent Strain (mm/mm)	Max Deformation (mm)	Equivalent Stress (MPa)	Equivalent Strain (mm/mm)
B_4C	0.043	1956.6	0.0047	0.0043	195.66	0.00047
Al_2O_3	0.054	1962.1	0.0058	0.0054	196.21	0.00058
Macor	0.298	1976.7	0.032	0.0298	197.67	0.0032

As shown in the above table, Macor has the largest maximum deformation and the biggest equivalent strain among three selected materials under the same loads (0.298 mm and 0.032 mm/mm under 300 kN, and 0.0298 mm and 0.0032 mm/mm under 30 kN respectively), while B_4C has the smallest values. Furthermore, Macor has the highest equivalent stress of 197.67 MPa, and B_4C has the lowest equivalent stress of 195.66 MPa among three materials under 30 kN. Therefore, the 3PB simulation results present that Macor can endure more stress than the other two materials, which is conflicting with the result from the Brazilian disk test. However, the maximum deformation and the biggest equivalent strain show Macor has the worst bearing capacity in the 3PB test, compared with B_4C and Al_2O_3. This result complies with the result from the Brazilian disk test. In the Brazilian disk test, Macor has been proven to be the weakest material, and it seems to be non-homogeneous. Thus, conducting the 3PB test on a non-homogeneous material like Macor might lead to a different result.

4.4.2. Three-point bending test and analysis

Like the Brazilian disk test, the 3PB tests are conducted on the same machine, the INSTRON 30 TON. The test machine with a capability of 100 kN static loads is widely used for the 3PB test. A typical configuration of most specimens is a rectangular bar. The loading configuration is a cylinder bar. Figure 4.20 presents the test devices. As the Figure shows, two cylinder bars are fixed parallel to each other on the test platform, with a fixed distance of 60 mm. A displacing cylinder bar is placed above the middle of the tested specimen, and a soft Pb metal sheet is used as a gasket between the sliding cylinder and the specimen, to compensate the surface anomalies that may exist between the interfaces. The sliding cylinder and the Pb gasket are presented in Figure 4.21.

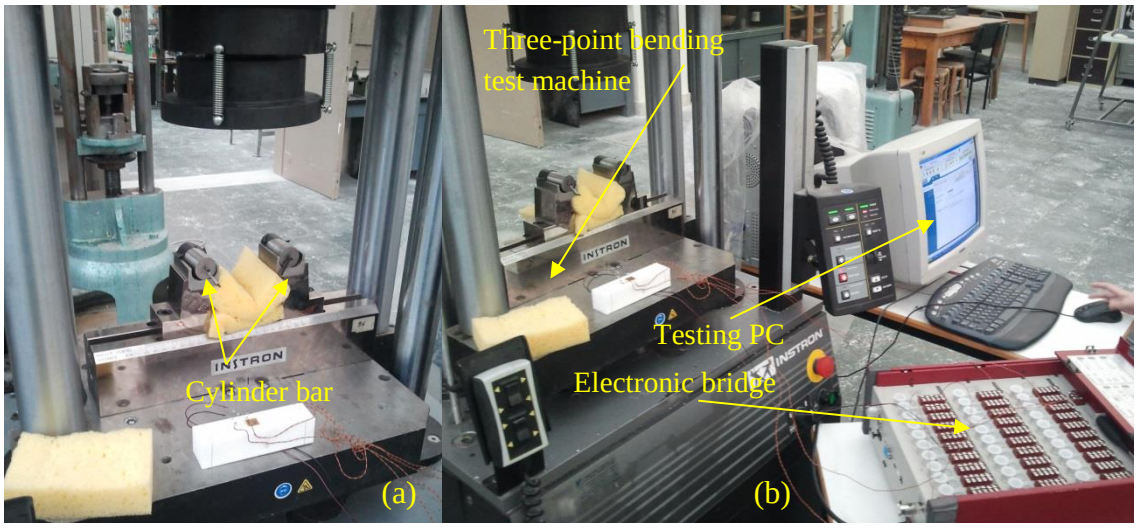

Figure 4.20. 3PB test equipments: (a) 3PB test machine with two fixed cylinder bars; (b) 3PB test machine, electronic bridge and testing PC

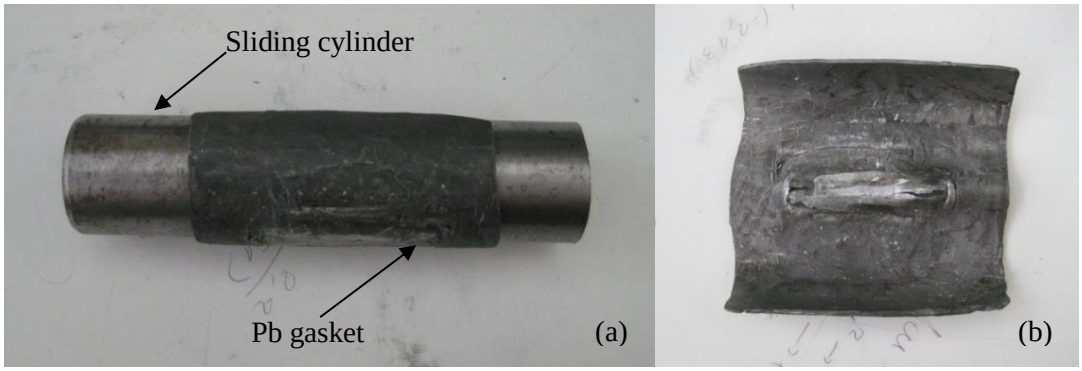

Figure 4.21. *Sliding cylinder and Pb gasket:*
(a) Sliding cylinder with Pb gasket;(b) Pb gasket

Similar to the specimen preparation of the Brazilian disk test, to start the 3PB test, all the specimens need to be named one by one. Triple strain gauges on the center of the surface of each specimen have to be positioned and glued. The sensor *c* detects the horizontal strain and is parallel with the length of the rectangular bar. Sensor *a* detects the vertical strain, and is parallel to the axis of the displacing and fixed cylinders. The prepared specimens with glued strain gauges for material A, M and B are named and presented in Figure 4.22. The connected specimen and machine are shown in Figure 4.23. The surface glued with the strain sensors has to be faced down in the 3PB test. Pressure applied by the displacing cylinder has to be avoided.

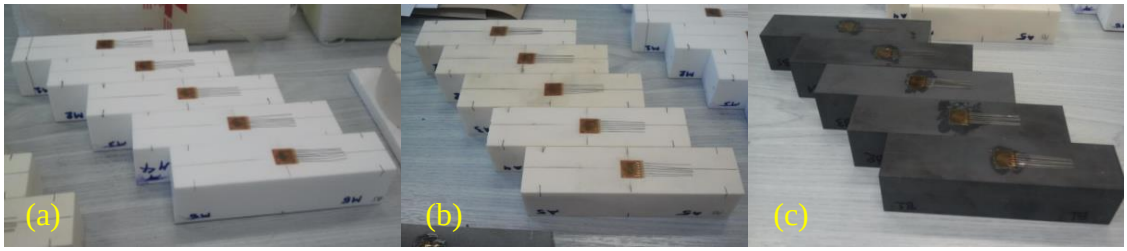

Figure 4.22. *Prepared specimens: (a) M1-M5, (b) A1-A5, (c) B1-B5*

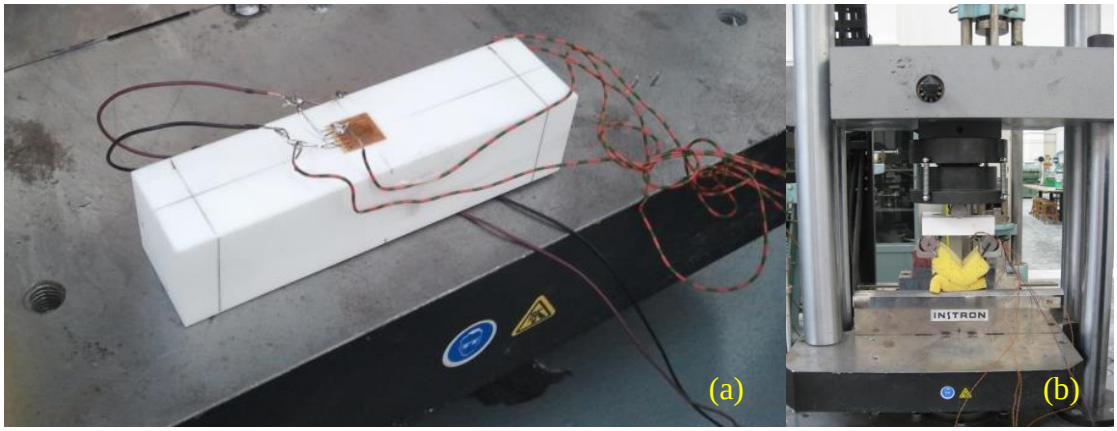

Figure 4.23. *Connected specimen with the testing machine: (a) prepared specimen with the glued gauge, (b) 3PB test machine with the positioned specimen*

During the 3PB test, the static load reaches 24 kN for the M1 specimen to break. For M2, M3, M4 and M5, the results of the maximum loads to be 20 kN, 20 kN, 14 kN and 16 kN. Pictures are shown in Figures 4.24, 4.25 and 4.26.

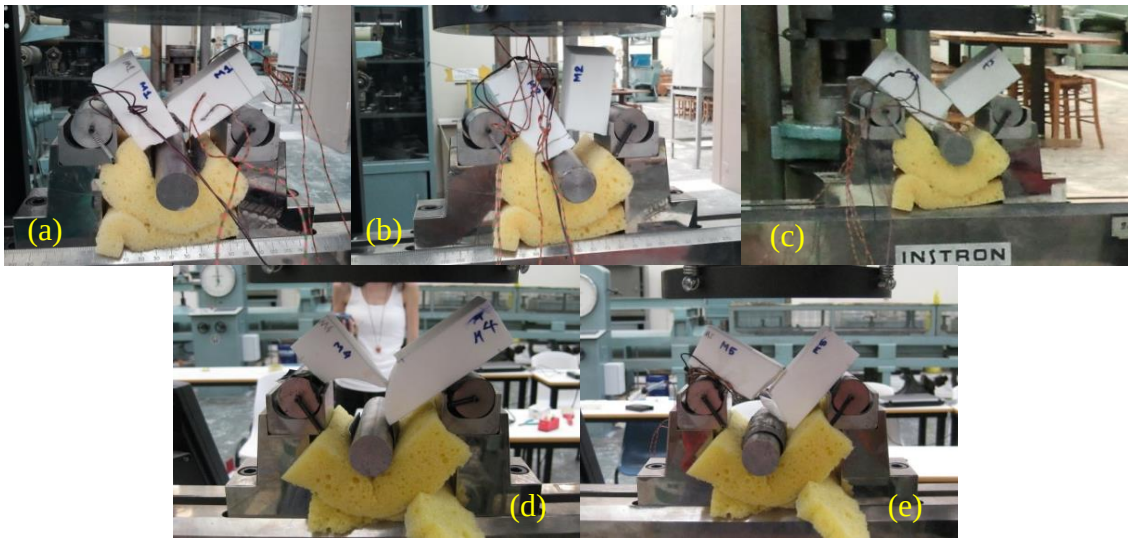

Figure 4.24 *The failure status of five M specimens: (a) M1-3PB; (b) M2-3PB; (c) M3-3PB; (d) M4-3PB; (e) M5-3PB.*

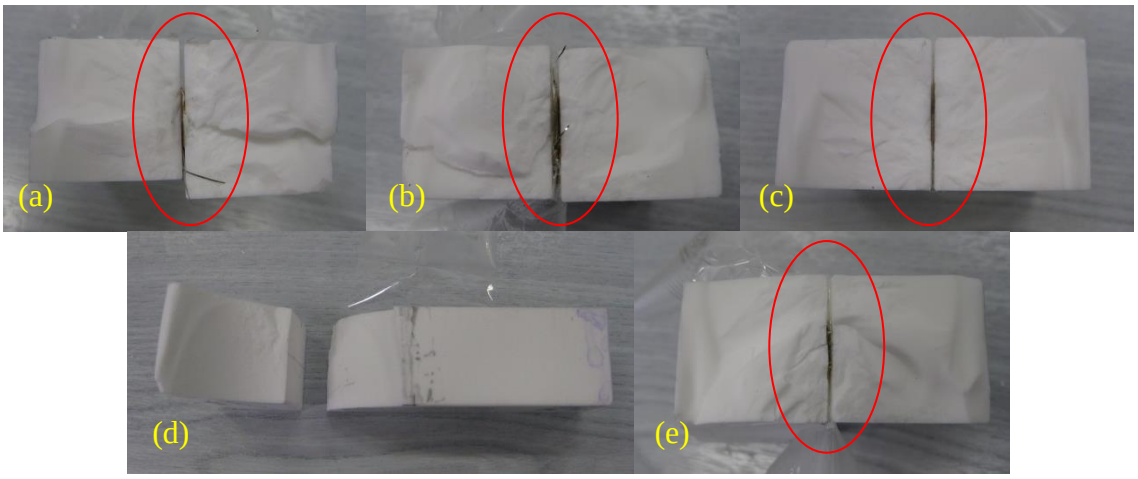

Figure 4.25 *Ruptured cross sections of five M specimens:*
(a) M1-3PB, (b) M2-3PB, (c) M3-3PB, (d) M4-3PB, (e) M5-3PB

After a careful examination to the failure moment of the specimen and the cross-section of the rupture, the failure status of M4-3PB proved to be different from the other specimens. The reason for the different failure effect is that the displacing cylinder was sliding from the center of the specimen interface towards the left side, and the Pb gasket slid along the surface of the cylinder as well. Once there is a space between the Pb gasket and the cylinder, the top cylinder slides aside while the static loading is ongoing. From the cross section surfaces of the fractured specimens in Figure 4.25, it is easy to see that the fracture initiated from the mid-span area, and extended through the beam to the bottom side, which was held by two fixed cylinder bars. The surface status of the cross section of the fractured beams is different. The region where the damage starts from is much rougher than the rest of the cross section surface, which can explain that the fracture is propagated along the vertical direction after the crack initiated from the tip crack in beams.

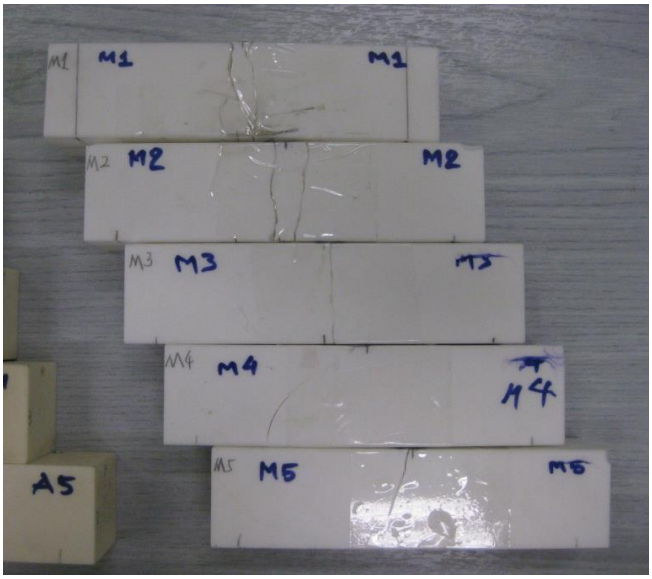

Figure 4.26 *Cracking path of M specimens after the rupture*

It is also evident in Figure 4.26 that the initial crack starts from the mid-span of the beam, then the crack is propagated along the inside structure, downwards to the bottom of the beam. As mentioned before, the crack prefers growing along the initial crack direction. The crack path should be a stable and straight line. However, except M3 and the failed specimen M4, the crack paths of the rests show roughness and twists. It may be because the micro-voids, impurities or heterogeneity exist in Macor beam, which obstruct the cracks propagation. Then the crack propagation bypasses the micro-voids and the propagation direction changes as well. Even though, the crack still returns back to its initial path. Meanwhile, some discrete micro-cracks are activated and formed a fracture zone near the vertical center line of the beam. Thus, few small fractured pieces appear during the test, but the beam is not completely broken into two pieces.

All three materials (Macor, Al_2O_3 and B_4C) are tested under the same conditions, and the failure status of specimen A and specimen B are presented in Figures 4.27 and 4.29. The cross sections of the ruptured A specimens and B specimens are shown in Figures 4.28 and 4.30. The Figure 4.31 illustrates the overview of the crack paths of A specimens and B specimens after rupture. The Al_2O_3 specimens are broken when the static loads reach 34 kN, 27 kN, 28 kN, 25 kN and 35 kN for A1, A2, A3, A4 and A5 respectively. Likewise, the maximum failure static loads for B_4C are measured to be 27 kN, 31 kN, 30 kN, 30 kN and 31 kN correspondingly.

Similar to Macor, from the cross section surfaces of specimens, the initiated damage region can be observed from both Figures 4.28 and 4.30. Also the stress concentration area can be defined. That corresponds to the previously mentioned theoretical results of the simulation demonstration.

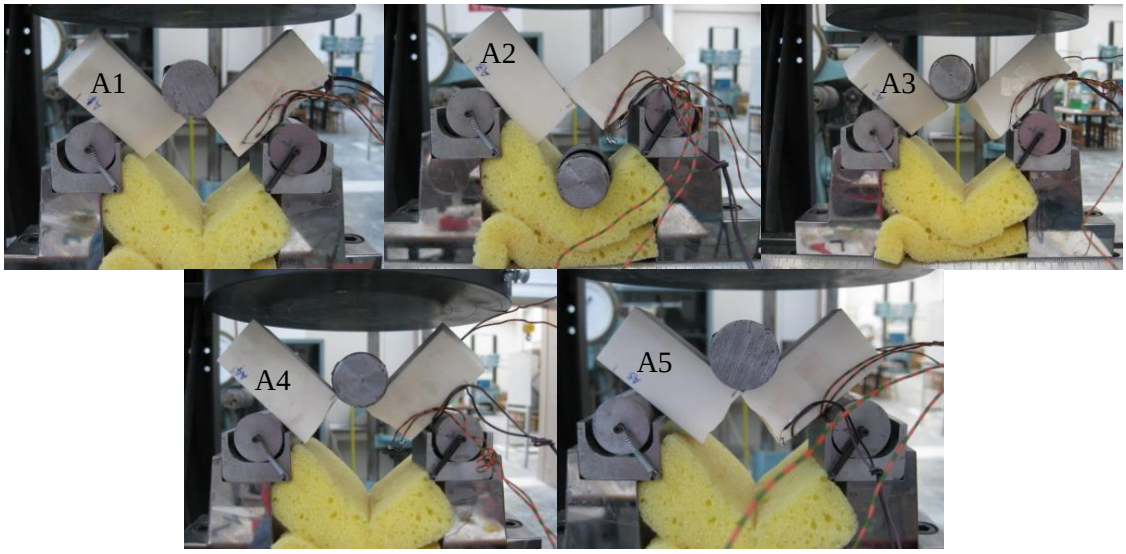

Figure 4.27 *Failure status of five A specimens*

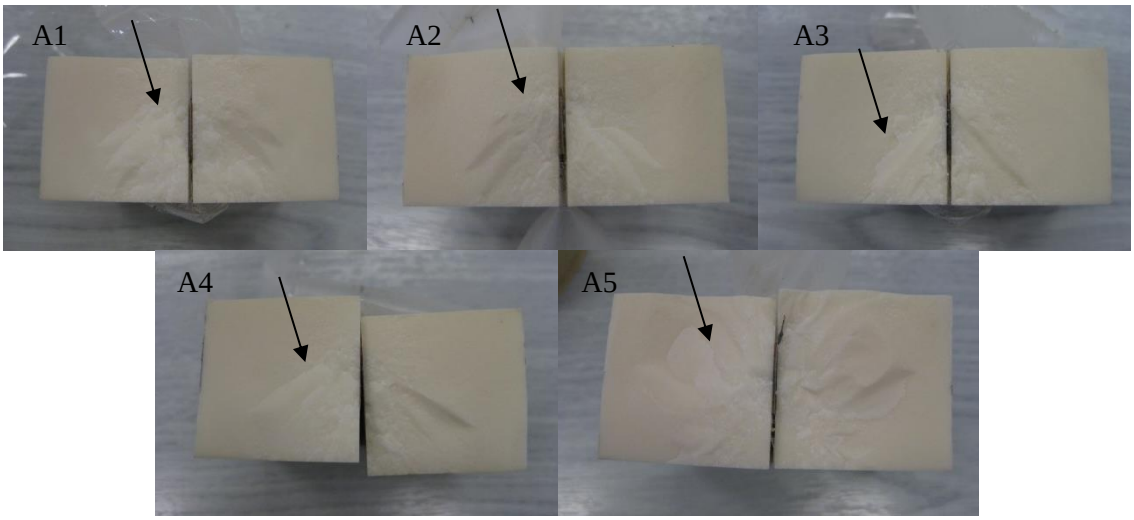

Figure 4.28. *Cross sections of five ruptured A specimens*

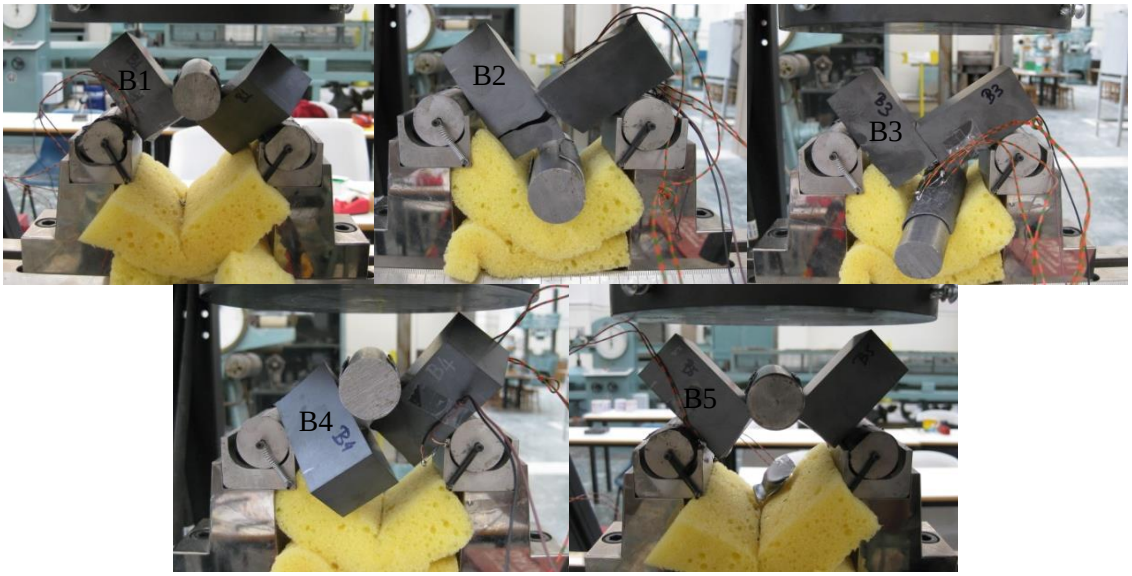

Figure 4.29. *Failure status of five B specimens*

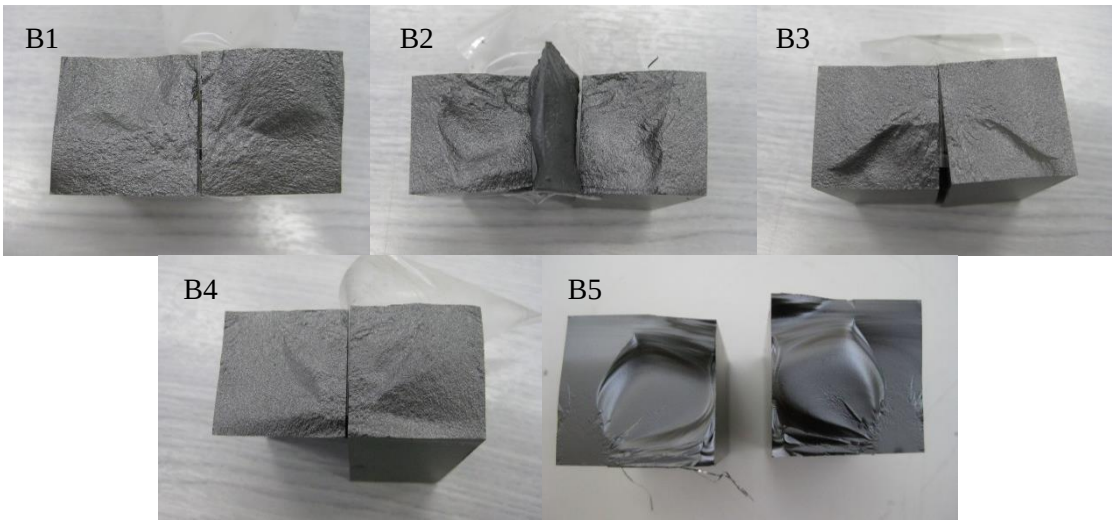

Figure 4.30. *Ruptured cross sections of five B specimens*

As presented in Figure 4.31, the cracks of Al_2O_3 and B_4C specimens are propagated almost along the vertical center line of the beams, which are different from the cracking paths of Macor. Similar to the simulation analysis, the damage starts from the crack tip and the crack propagation develops along the initiated direction. Even those crack paths are not very straight; the crack lines seem to be stable.

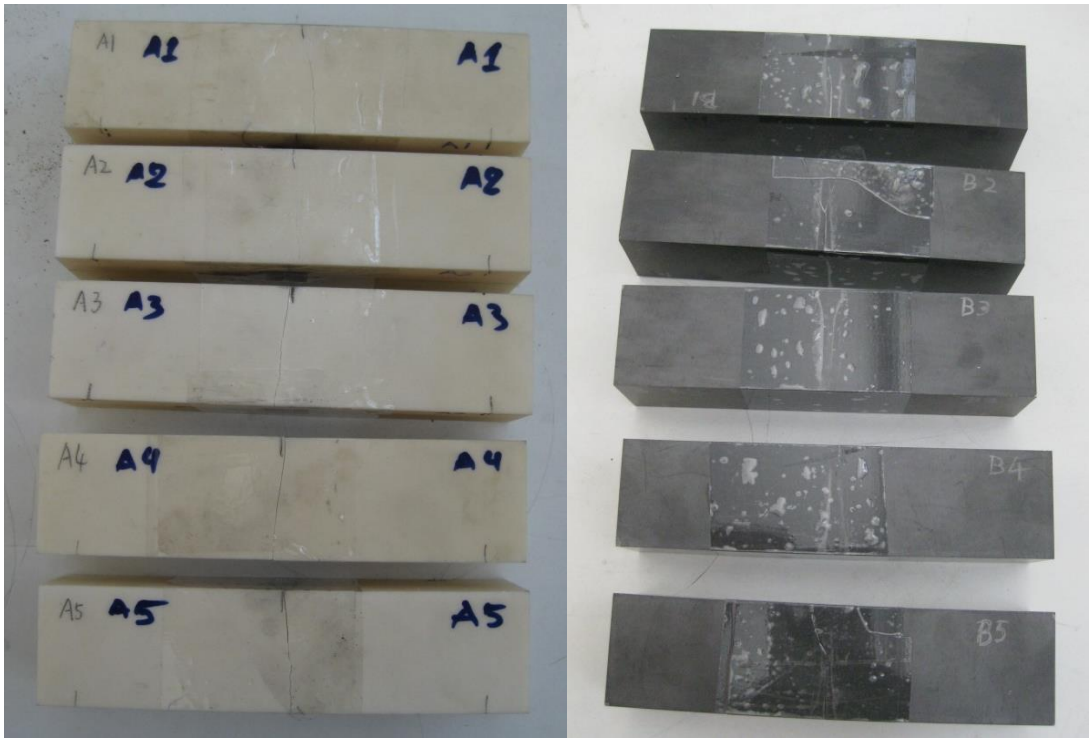

Figure 4.31. *Crack paths of the ruptured specimens. (a) A specimens; (b) B specimens*

After examining the failure status of all the tested materials in 3PB test, Macor proved to be the "weakest" material again in comparison to the others (Al_2O_3 and B_4C). The mechanical test result is also conformed to the simulation result.

5. RESULTS AND DISCUSSION

From the Brazilian disk test and the 3PB test, massive interesting data are obtained via the testing PC from the electronic bridge acquisition system. The strain is recorded directly from the electronic bridge acquisition system, and the applied load, measured extension, compressive strain, compressive stress, compressive load are recorded by the testing PC from the loading sensor. After the data processing, the comparison curves for each material and the comparison tables are drew. The Young's modules (E) and the Poisson's ratio (ν) are also calculated. This chapter presents the experimental curves and tables for comparison. Through the comparison and data analysis, the properties of the materials are discussed. Moreover, the result of Young's modulus from the Brazilian disk test for the Macor is compared with the tested result of the Epument from the previous year. In addition, the Young's modulus from the Brazilian disk test for the Macor is compared with the measured and calculated value acquired from 3PB test. As a conclusion, a proposal for the better structural material is provided.

5.1. Brazilian disk test result and discussion

In the Brazilian disk test, 0.02 mm/min loading speed is applied to simulate the static load. The load-displacement curves for five Macor specimens are shown in Figure 5.1. It is evident that the displacement increases with the increasing of the pseudo static load applied on specimens. The total deformations of M1, M2, M3, M4 and M5 are 1.36 mm, 1.73 mm, 1.32 mm, 1.45 mm and 1.23 mm accordingly. The maximum loads at the rupture points of the specimens are 110.20 kN, 137.84 kN, 135.99 kN, 138.21 kN and 133.02 kN correspondingly. Compared with the maximum deformations of 0.55 mm under the 300 kN loads, and of 0.055 mm under the 30 kN loads in the simulation, the before mentioned values appear relatively. The real deformations between 1.23 mm to 1.73 mm appear under 110.20 kN and up to 138.21 kN. The values are bigger than simulation results described in Chapter four. Because the simulation results are based on the assumption of homogeneous materials, the actual heterogeneous structure of the material and lots of voids in the material cause the deviation of above results.

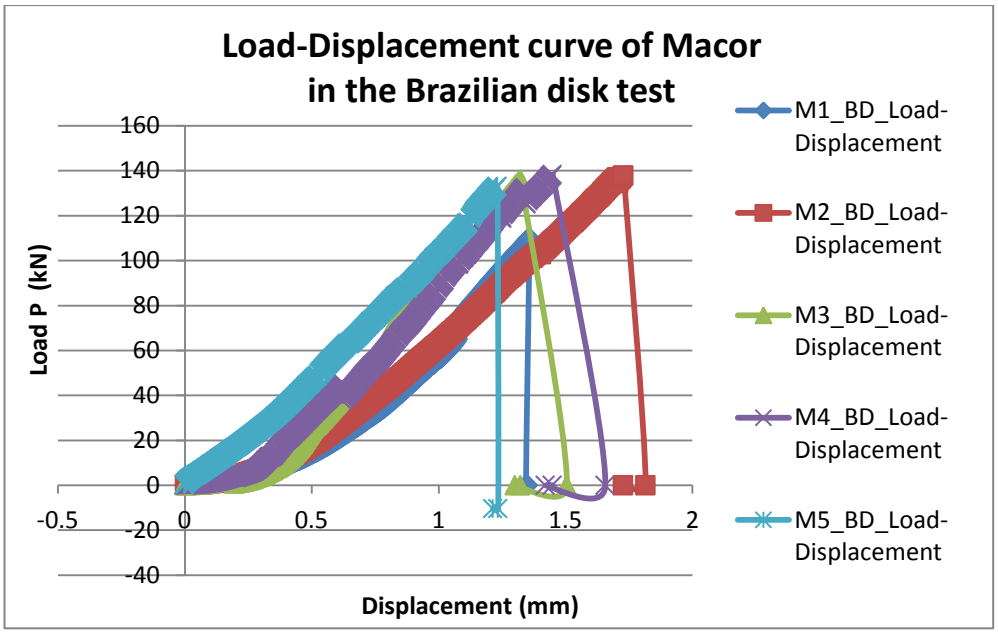

Figure 5.1. *The Load-Displacement curves of Macor (M) specimens in the Brazilian disk test (BD)*

In Figure 5.1, the load-displacement curves of five M specimens appear to have a linear-like behavior, also those curves are similar with each other except the slightly individual differences from each specimen. In general, the displacement increases slowly when the load is less than 20 kN. At this stage, the load is accumulating; meanwhile, the stress concentration starts growing along the vertical diameter of the specimen. The first element is damaged around the vertical diameter of the disk; therefore, the fracture is initiated. As the loading is ongoing, more elements near the vertical diameter are damaged, and the fracture is propagating rapidly with the increasing loads under the increased stress concentration, until the specimen break. At the moment, the maximum displacement, maximum load and maximum strain are obtained and recorded by the test equipment.

From previously acquired available data of Epument of different sizes in Brazilian disk test, the Strain-Stress curves of Epument-B and Epument-S are shown in Figures 5.2 and 5.3. From Figure 5.2, the maximum stresses of all Epument-B specimens are between 0.96 MPa and 1.18 MPa. The maximum stresses of all Epument-S specimens from 1.25 MPa to 1.42 MPa are shown in Figure 5.3. Testing data of Epument S-1 are suppressed due to it comes from the integrated rock reinforcement area and not the actual material.

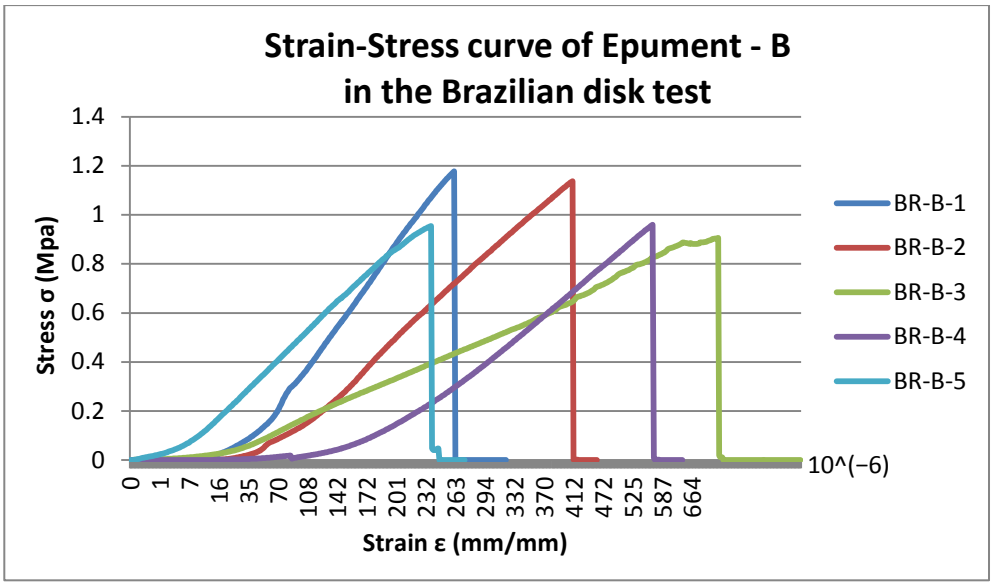

Figure 5.2. *The Strain-Stress curves of Epument-B specimens in the Brazilian disk test (BR)*

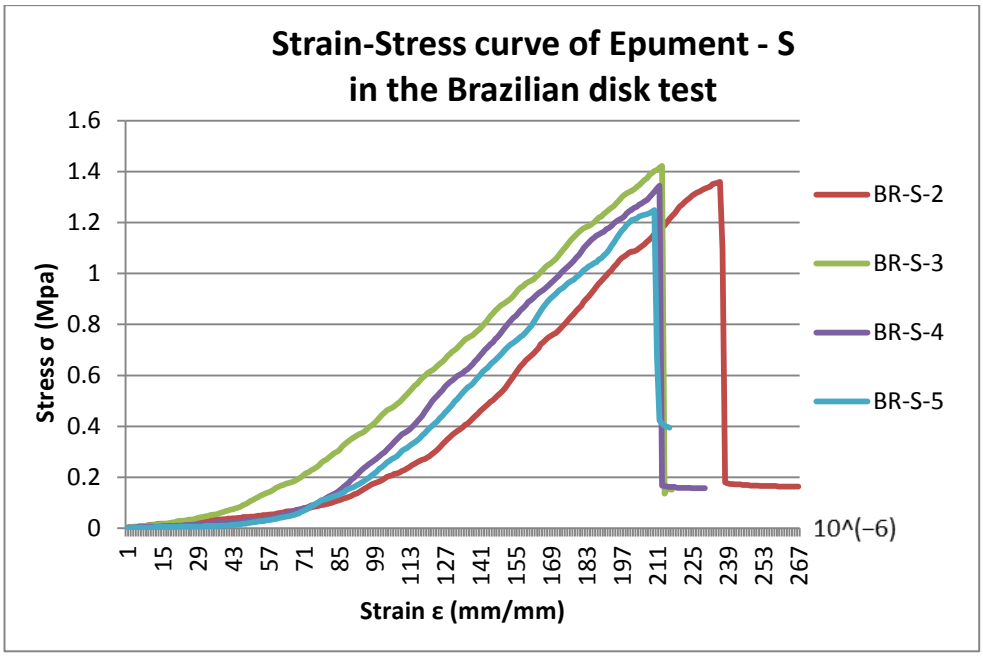

Figure 5.3. *The Strain-Stress curves of Epument-S specimens in the Brazilian disk test (BR)*

The strain-stress curves in Figures 5.2 and 5.3 increase linearly. Although it was mentioned in previous chapter that the size of the specimen has no influence to the test results of Brazilian disk test, to verify if the size of the disk will really affect the Young's modulus of the material in reality, Figures 5.2 and 5.3 are intergraded in Figure 5.4. It is obvious to see that the curves of Epument-B and Epument-S are overlapped and appear

to be linear. The blue point in Figure 5.4 represents the test result of the integrated rock reinforcement in the specimen, which is not taken into account in the comparison.

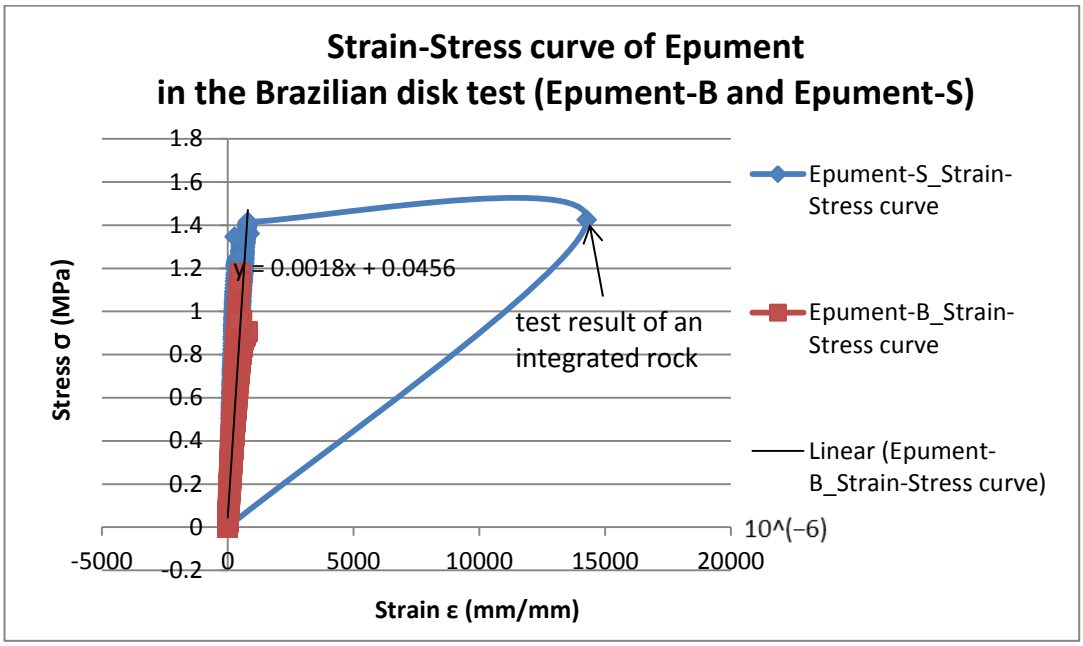

Figure 5.4. *The Strain-Stress curves of Epument specimens in the Brazilian disk test (BR)*

Due to the fact that strain-stress curves are linear, the Young's modulus E can be represented by the slope of the line section, which can be obtained by the formula (2) of chapter three. Also as mentioned before, from the Figure 4.15, the ruptured specimens of Epument presented the similar homogenous behavior in the Brazilian disk test. Thus, the tensile stress can be calculated from the equation (1) of chapter three, and the tensile strains are obtained directly from the electronic bridge acquisition system. As a result, the calculated Es of the Epument large disks and the small disks are similar to each other, around 1.8 GPa, which proves that the size of the specimen is not an influence factor for Brazilian disk test.

For Macor disks, the crack traces shown in Figure 4.14 indicate Macor does not behave as homogenous as assumed. In this case, the stress of Macor in the Brazilian disk test has to be calculated as mentioned in the study of Ye Jianhong et al., for non-homogenous material [42]. Therefore, the E should be calculated via formulas (5), (6) and (7). The Poisson's ratio ν in formulas (6) and (7) is the actual Poisson's ratio of the tested material, which is the most important factor in the calculation. The reliability of the tensile elastic modulus E_t is determined by the accuracy of the ν. From the formula (7), it is easy to see that the correction coefficient A is sensitive to Poisson's ratio. By equation (3), the actual Poisson's ratio ν of the tested material should be defined by uniaxial compression test, which is not available in this thesis. Thus, the Young's modulus

E of Macor in Brazilian disk test is calculated via formula (2), and compared with the values obtained from the 3PB test.

Assuming that three candidate materials are performing homogeneously and isotropically, in the same way as Epument, the Young's modulus of the Brazilian disk test can be obtained directly from the slope of the strain-stress curve. The strain-stress curves of five Macor are shown in Figure 5.5.

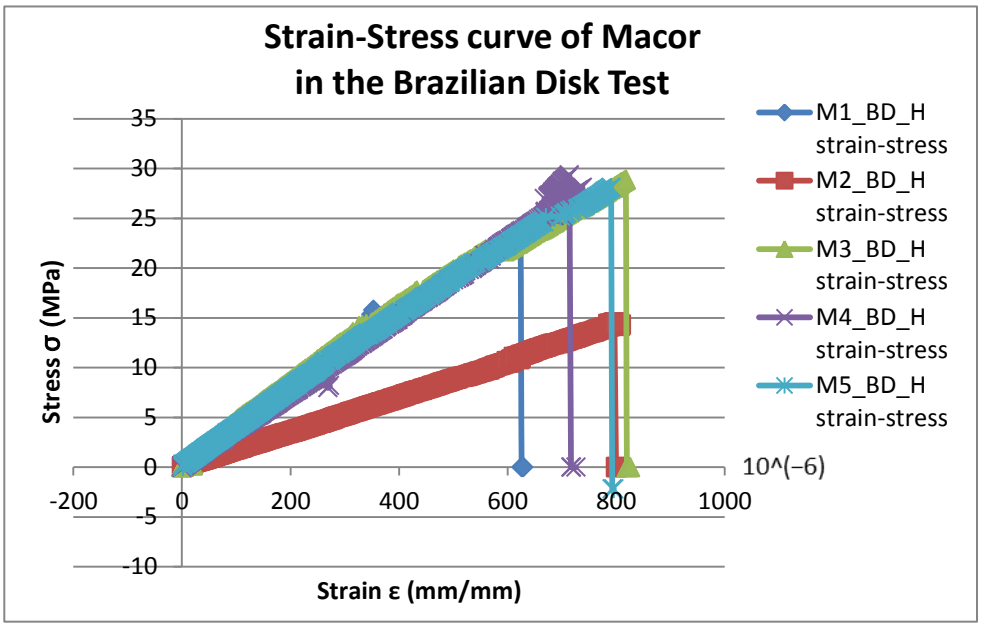

Figure 5.5. *The strain-stress curves of Macor (M) specimens in the Brazilian disk test (BD)*

Figure 5.5 shows the strain-stress curves of five Macor specimens. With the exception of the M2 specimen, all data of the other specimens are overlapped on the same linear line. It also indicates that the strain and stress are increasing with the increased load. At the point before the material failed, the maximum strain and stress are reached. Because the curves are linear, via formula (2), the Young's modulus of M1, M3, M4 and M5 are calculated to be 36.6 GPa, 34.2 GPa, 37.4 GPa and 34.6 GPa correspondingly, while the value of M2 is 17.4 GPa.

In order to compare the Young's modulus of Epument and Macor from the Brazilian disk test, the strain-stress curves of all disk specimens are intergraded in Figure 5.6. From the figure, the strain-stress curves of both Macor and Epument are linear, and the slope of 0.0365 of Macor is bigger than the slope of 0.0018 of Epument. Via formular (2), the average Young's modulus E_{Macor} is 36.5 GPa, which is higher than the 1.8 GPa of $E_{Epument}$. In addition, both tested results are smaller than the theoretical values provided by firms.

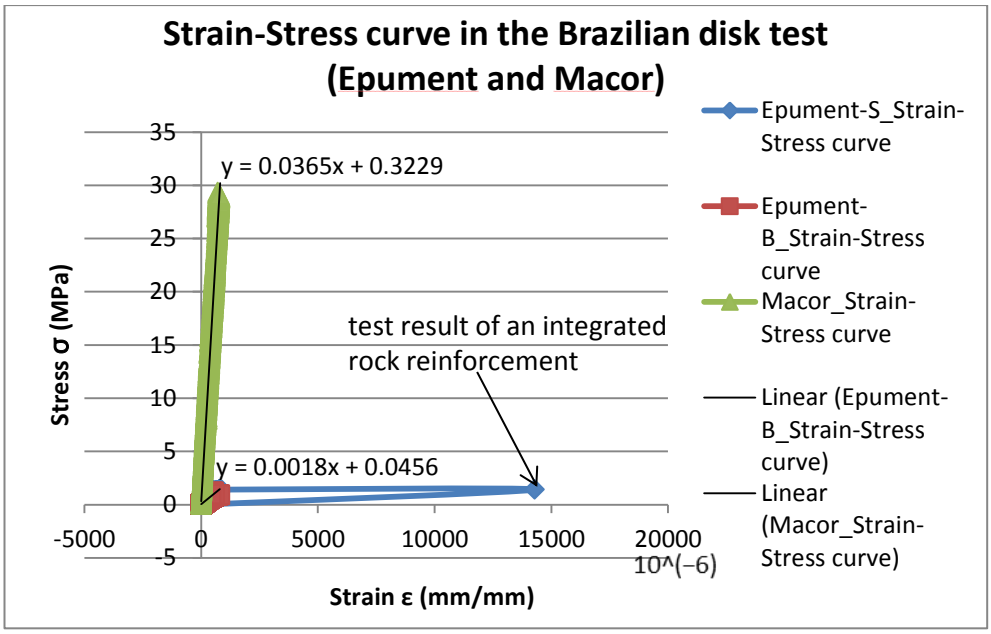

Figure 5.6. *The strain-stress curves of Macor (M) and Epument specimens in the Brazilian disk test (BD)*

Above results conform to the theory that was mentioned in the previous chapter, and it also indicates that the displacement of the specimen is controlled by the compressive loading condition [54]. The maximum loads applied in Brazilian disk test, the obtained maximum strain, the maximum stress and the maximum displacement of Epument specimens and Macor specimens are listed respectively in Table 5.1, except the suppressed data of Epument S-1.

Table 5.1. *The experimental results of Epument and Macor specimens in the Brazilian disk test*

Material	Max Load (kN)	Max Strain (mm/mm) $* 10^{-6}$	Max Stress (MPa)	Max Displacement (mm)
Epument B-1	216.88	515	1.18	0.003
Epument B-2	207.95	535	1.14	0.003
Epument B-3	168.74	800	0.91	0.004
Epument B-4	176.26	571	0.96	0.003
Epument B-5	175.88	420	0.96	0.004
Epument S-2	69.50	885	1.36	15.69
Epument S-3	70.75	14286	1.42	14.29
Epument S-4	68.41	521	1.35	14.65
Epument S-5	64.46	410	1.25	14.36
Macor 1	110.20	624	23.38	1.36
Macor 2	137.84	809	14.53	1.73
Macor 3	135.99	818	28.86	1.32
Macor 4	138.21	741	29.34	1.45
Macor 5	133.02	791	28.08	1.23

As shown in the table, the maximum strains for Epument-B and Epument-S are in the similar ranges, which are from 420 * 10^{-6} mm/mm to 800 * 10^{-6} mm/mm, and from 410 * 10^{-6} mm/mm to 885 * 10^{-6} mm/mm, while the maximum loads are quite different. By comparing the maximum loads applied on Epument-S and Macor, and their representative maximum displacement, it is obvious that Macor can withstand higher loads than Epument, while Epument has more deformation than Macor.

5.2. Three-point bending test result and discussion

As mentioned in chapter four, the Brazilian disk test of B_4C and Al_2O_3 will be conducted in future. To compare the candidate materials with the baseline and the alternative materials, three candidate materials are treated as isotropic and homogeneous materials in current thesis.

In the 3PB test, the static loading speeds applied on Macor, Al_2O_3 and B_4C are 0.02 mm/min, 0.1 mm/min and 0.05 mm/min respectively. The load-displacement curves are presented in Figures 5.7, 5.8 and 5.9.

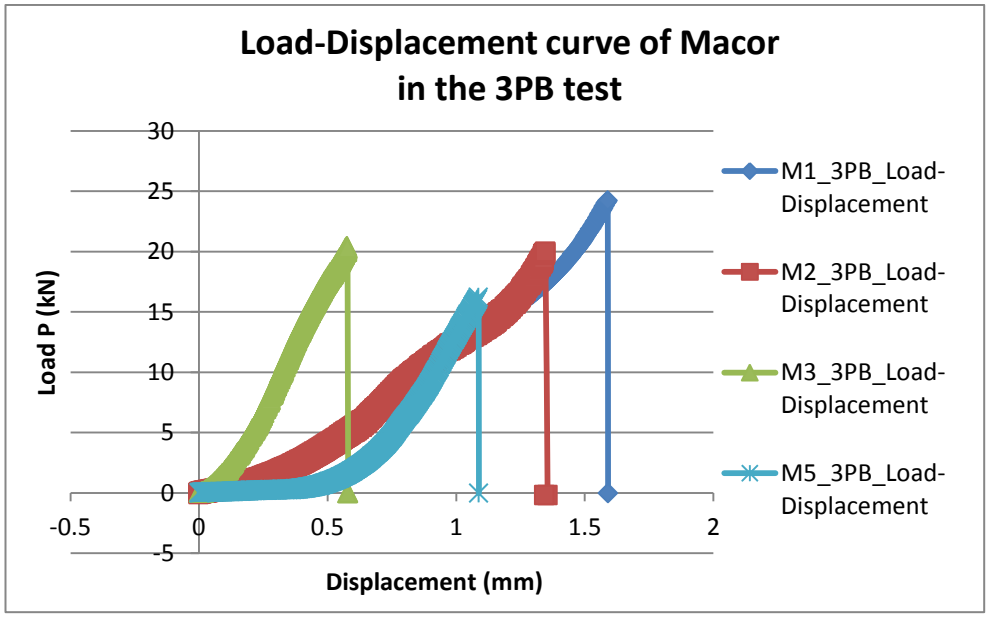

***Figure 5.7**. The Load-Displacement curves of Macor (M) specimens in the 3PB test*

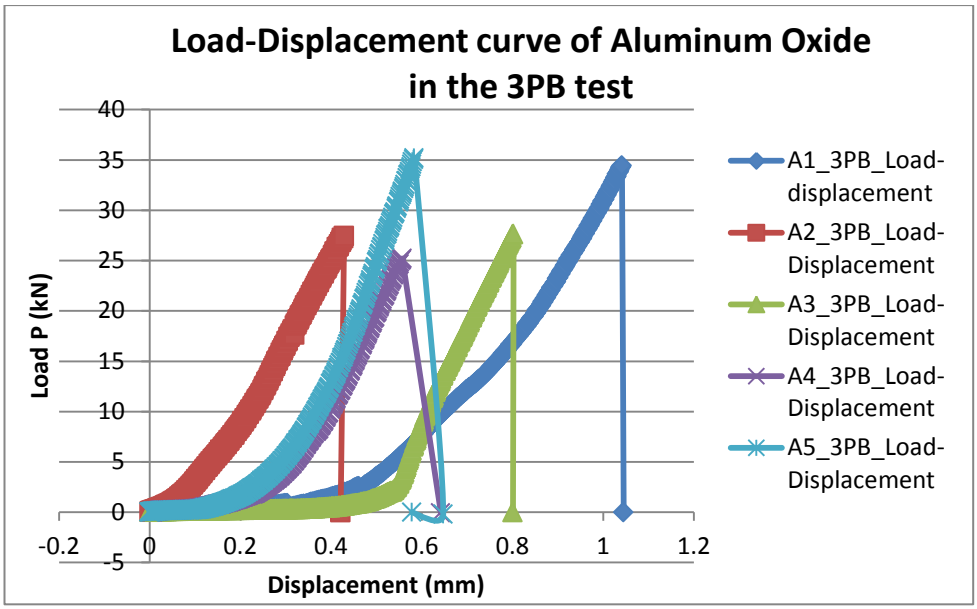

***Figure 5.8**. The Load-Displacement curves of Al_2O_3 (A) specimens in the 3PB test*

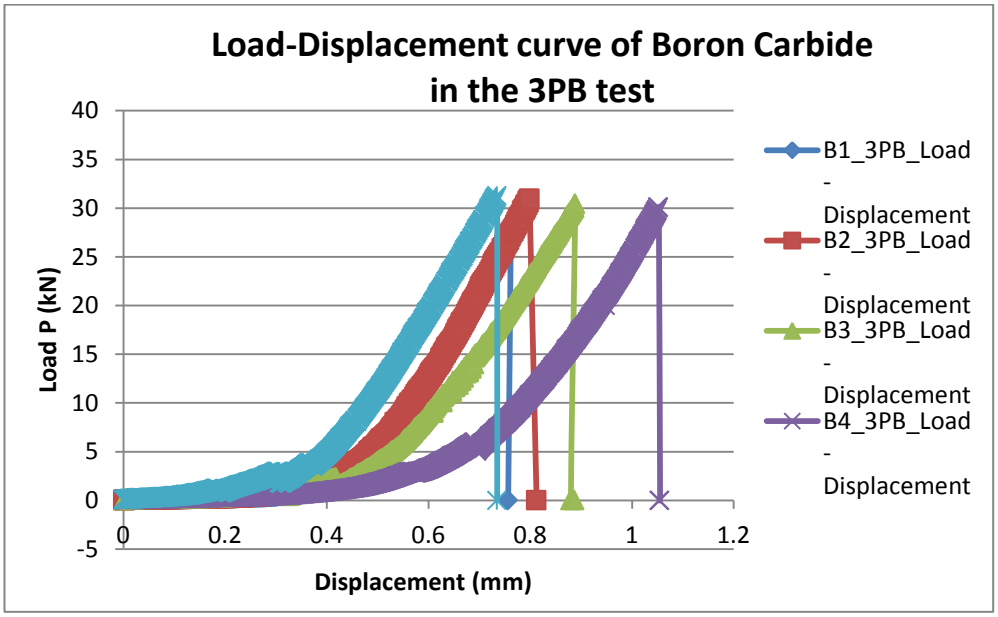

***Figure 5.9**. The Load-Displacement curves of B_4C (B) specimens in the 3PB test*

As mentioned in previous, during the 3PB test of M4 specimen, the cylinder was sliding while the static load was applied. In Figures 5.7, 5.10 and 5.13, the testing data of M4 are suppressed due to the measured values come from a positioning fault during the experiment and can't be considered.

From Figures 5.8 and 5.9, it is obvious that the curves of B_4C are in the same range of values. The displacements increase slowly when the load is less than 5 kN. Afterwards, the displacements increase rapidly until the specimens are broken. The maximum displacements for Macor are measured to be from 0.58 mm to 1.59 mm when the maximum applied loads vary from 16.21 kN to 24.21 kN. Such values are bigger than the simulation result of 0.298 mm under 300 kN, for the same reason as mentioned before.

For B_4C and Al_2O_3, the maximum displacements are from 0.73 mm to 1.05 mm and from 0.43 mm to 1.04 mm correspondingly, while the maximum loads vary from 27.08 kN to 31.26 kN, and from 25.22 kN to 35.19 kN respectively. The corresponding simulation results of 0.043 mm and 0.054 mm under 300 kN for B_4C and Al_2O_3 are less than the actual tested results.

In general, the load-displacement curves in above figures prove and explain the mentioned fracture process of specimens in the 3PB test. At the beginning of the test, the displacement of the specimen increases slowly with the increasing of the static load, and the material surface receives stress concentration and extends the stress concentration along the mid-span vertical direction of the specimen. When the stress concentration accumulated until a certain level, fracture is initiated from the material surface and propagated towards the mid-span vertical direction of the specimen. From the second part of the curves, the load-displacement curves behave linearly. Before the material fractured, the maximum displacement appears under the biggest loads. Based on the tested results, B_4C can withstand higher load and present small micrometric scale deformation, while Macor appears to present deformation when the loads are smaller than the Macor's maximum loads. This result conforms to the 3PB simulation result, which indicates that the Macor is the weakest material and B_4C to be the strongest material in the 3PB test among three candidate materials. It again indicates that the 3PB test is not suitable to be used for non-homogeneous material, and the test result is not accurate.

The rectangular configuration of the specimens are with 120 mm long, 30 mm wide (W) and 30 mm high (H) in the 3PB test, and they are placed above of two fixed cylinders which have a distance of 60 mm (L) from each other. By the force (P) applied from the testing PC, the maximum flexural stress (σ) can be calculated by using equation (12). The strain-stress curves of Macor, Al_2O_3 and B_4C in the 3PB test are described in Figures 5.10, 5.11 and 5.12.

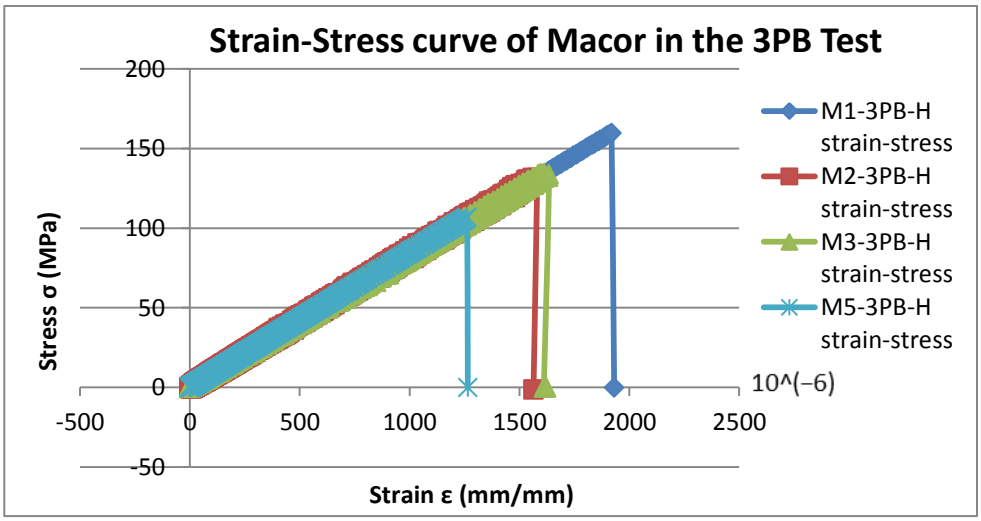

***Figure 5.10**. The Strain-Stress curves of Macor (M) specimens in the 3PB test*

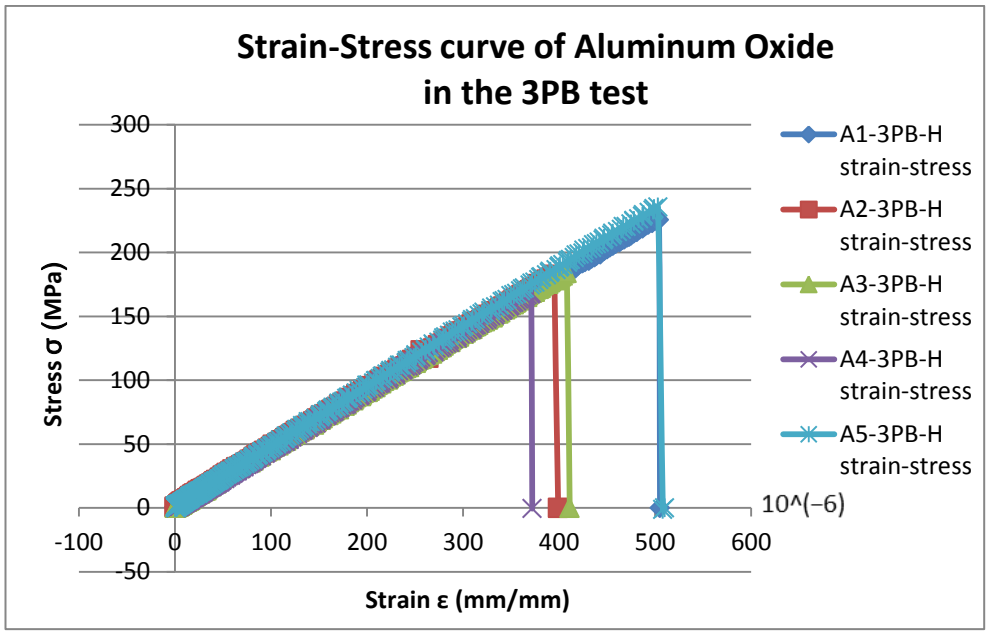

Figure 5.11. *The Strain-Stress curves of Al_2O_3 (A) specimens in the 3PB test*

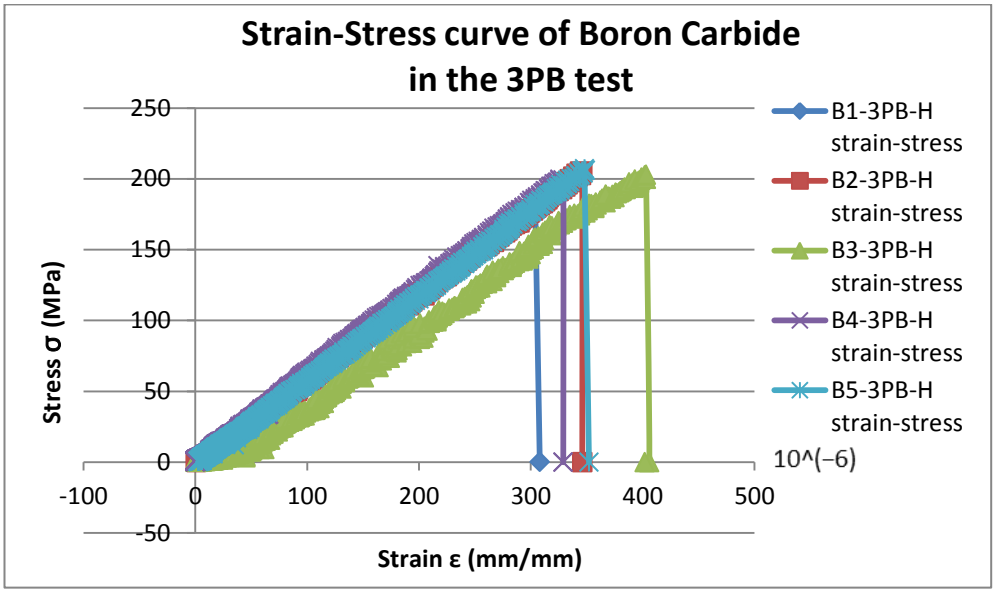

Figure 5.12. *The Strain-Stress curves of B_4C (B) specimens in the 3PB test*

From Figures 5.10 to 5.12, all the curves of each material appear linearly. The stress increases linearly with the strain. On the same chart, the curves appear overlapping with each other, and their slopes are similar, especially in Figures 5.10 and 5.11. By using the formula (12), the tensile stresses of all tested specimens are presented in Table 5.2. As shown in the Figures and the Table, the ranges of the maximum loads of material B, A and M are 27.09 kN - 31.26 kN, 25.22 kN - 35.19 kN, and 16.21 kN - 24.21 kN. Accordingly, the ranges of the maximum deformations are 0.73 mm - 1.05 mm, 0.43 - 1.04 mm, and 0.58 mm - 1.59 mm respectively. Again, it proves that B_4C and Al_2O_3 can withstand higher loads than Macor, same as the simulation result.

Table 5.2. *The experimental results of three candidate materials in the 3PB test*

Material	Max Load P (kN)	Max Strain (mm/mm) $* 10^{-6}$	Max Stress (MPa)	Max Displacement (mm)
B_4C 1	27.09	304	179.25	0.76
B_4C 2	30.95	344	205.13	0.80
B_4C 3	30.44	403	202.70	0.89
B_4C 4	30.12	326	199.62	1.05
B_4C 5	31.26	348	207.12	0.73
Al_2O_3 1	34.43	504	225.60	1.04
Al_2O_3 2	27.43	395	182.48	0.43
Al_2O_3 3	27.62	408	255.60	0.80
Al_2O_3 4	25.22	371	168.12	0.56
Al_2O_3 5	35.19	503	235.42	0.58
Macor 1	24.21	1919	159.68	1.59
Macor 2	19.97	1578	131.66	1.35
Macor 3	20.29	1634	134.68	0.58
Macor 5	16.21	1262	106.86	1.09

By integrating the tested results of all three materials in one chart, the strain-stress curves are shown in Figure 5.13. The experimental results of the 3PB test for three candidate materials are listed in Table 5.2.

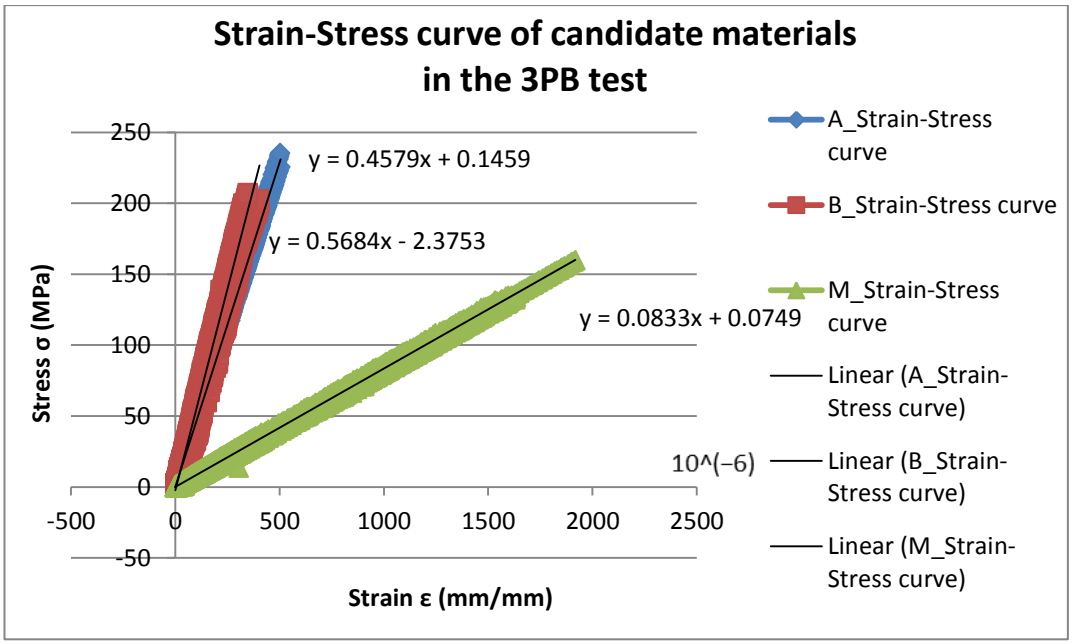

Figure 5.13*. The Strain-Stress curves of three candidate materials in the 3PB test*

Figure 5.13 shows the strain-stress relationships between three candidate materials, also the slopes of each material are presented and compared. By using the formula (2), the Young's modulus of materials A, B and M are calculated to be 457.9 GPa, 568.4 GPa and 83.3 GPa correspondingly. Apparently, E_B is the biggest among three materials, while E_M is the smallest, and E_A is in between. The experimental results prove again that the stress concentration increases at the mid-span of the specimen surface, and initi-

ates the fracture. With the increased load, the displacement increases and the fracture is propagated along the initiated vertical direction of the specimen, until the material fractures.

By using the formulas (2) and (3), the Young's modulus E and the Poisson's ratio ν from the 3PB test are calculated and listed in Table 5.3. The maximum value of each material is highlighted with bold.

Table 5.3 *Young's modulus and Poisson's ratio of materials A, B and M in the 3PB test*

Material	E (GPa)	ν	Material	E (GPa)	ν	Material	E (GPa)	ν
A1	444.7	0.20	**B1**	580.4	0.14	**M1**	81.6	**0.23**
A2	446.4	0.20	**B2**	590.2	**0.19**	**M2**	83.4	**0.23**
A3	445.3	0.20	**B3**	517.9	0.12	**M3**	81.9	**0.23**
A4	447.2	0.19	**B4**	**602.7**	0.13	**M4**	\	\
A5	**448.6**	**0.21**	**B5**	590.0	0.13	**M5**	**83.5**	0.22

From above table, B_4C presents the highest Young's modulus (602.7 GPa), by comparing with Al_2O_3 (448.6 GPa) and Macor (83.5 GPa). It also has the lowest Poisson's ratio (0.19) among three materials. Macor has the lowest Young's modulus (83.5 GPa) comparatively, and the Poisson's ratio (0.23) is the highest among three materials. The values of the Young's modulus (448.6 GPa) and the Poisson's ratio for Al_2O_3 (0.21) are in between. If all three candidate materials are presumed to be homogenous, by comparing the experimental results of Young's modulus and Poisson's ratio with the theoretical values in Table 2.3, the experimental Young's modulus are all higher than the theoretical values, while the experimental Poisson's ratios are all smaller than the theoretical values.

Table 5.4 *Maximum Loads and Maximum stresses of materials A, B and M in the 3PB test*

Material	P_{max} (kN)	σ_{max} (MPa)	Material	P_{max} (kN)	σ_{max} (MPa)	Material	P_{max} (kN)	σ_{max} (MPa)
A1	34.43	225.60	**B1**	27.09	179.25	**M1**	**24.21**	**159.68**
A2	27.43	182.48	**B2**	30.95	205.13	**M2**	19.97	131.66
A3	27.62	225.60	**B3**	30.44	202.70	**M3**	20.43	134.68
A4	25.22	168.12	**B4**	30.12	199.62	**M4**	\	\
A5	**35.19**	**235.42**	**B5**	**31.26**	**207.12**	**M5**	16.21	106.86

From the Table 5.4, the maximum load of B_4C is aroud 30 kN, while the related maximum stress is approximately 200 MPa. Al_2O_3 can withstand a maximum about 35 kN load, and the maximum stress (235.42 MPa) is relatively higher than B_4C. For the Macor, the maximum load is in the range of 15-20 kN and the maximum stress is around

135 MPa. The above results prove once more that the B_4C is stronger compared to Al_2O_3. The Macor is again the weakest material among all three candidates.

5.3. Summary of the test results

Following sections 5.1 and 5.2 in the current chapter, the key parameters of the mechanical properties of the candidate materials are investigated and discussed. For better understanding and comparison, the before mentioned main parameters of different materials are listed in Table 5.5. The experimental results are shown in bold, and the data of SiC and Epument are from firms.

As mentioned before, the 3PB test is mainly used on homogeneous materials or material with homogeneous structure. The Brazilian disk test is conducted first to confirm whether the material has homogeneous structure or not. If the Young's modulus of the Brazilian disk test is the same as the Young's modulus of the 3PB test, material proved to be a homogeneous material. If it is not the case, it is non- homogeneous material. However, the Brazilian disk tests for B_4C and Al_2O_3 are not available due to the limitation. The 3PB test results are based on the assumption of isotropic and homogeneous for all three candidate materials.

Table 5.5. *Properties comparison for baseline, alternative and candidate materials*

Materials	**SiC**	**Epument 145 B**	**B_4C**	**Al_2O_3 (99%)**	**Macor**
Density (g/cm^3)	3.21	2.4	2.48	3.81	2.52
Young's modulus E (GPa)	420	40-45	**517.9-602.7**	**444.7-448.6**	**81.6-83.5**
Poisson's ratio ν	0.16	0.30	**0.12-0.19**	**0.18-0.20**	**0.13-0.23**
Stress σ_{max} (MPa)	450	\	**179.15-207.12**	**168.12-235.42**	**106.86-159.68**
Load P_{max} (kN)	\	\	**27.09-31.26**	**25.22-35.19**	**16.21-24.21**

Table 5.5 shows the experiment results of the Young's modulus of material B, A and M, which are 517.9 - 602.7 GPa, 444.7 - 448.6 GPa and 81.6 - 83.5 GPa respectively. The Young's modulus of all three materials from experiments are all higher than its industrial values, by comparing with 450-470 GPa, 370 GPa and 66.9 GPa of material B, A and M from the Table 2.3. The minimum Young's modulus of B_4C (517.9 GPa) is the highest among three candidate materials, the baseline material and the alternative material, while the Young's modulus of Epument (40-45 GPa) is the lowest. Epument has the highest Poisson's ratio (0.30), which indicates the material should have bigger deformation than the others. The Poisson's ratio of SiC is 0.16, which is in the range of the Poisson's ratio of three candidate materials. The minimum Poisson's ratio of the B_4C (0.12) is the lowest among the compared materials. From the industrial values, the tensile stress of the SiC is still the highest (450 MPa) among five compared materials in

Table 5.5. Except Epument, the density of B_4C is the smallest (2.48 g/cm3) in the comparison of five materials, while the density of Al_2O_3 is the biggest (3.81 g/cm3). For this point, B_4C is lighter than the rests.

From the ruptured situation of Macor specimens in the Brazilian disk test, and calculating with formula (2), the Young's modulus of the Brazilian disk test E_{BD} (slope of 36.5 GPa) is not the same as the Young's modulus of the 3PB test E_{TPB} (slope of 83.3 GPa). However, the theoretical Poisson's ratio is used in the calculation of the Young's modulus in Brazilian disk test, due to the non-availability of the uniaxial test in this study. The calculated Young's modulus of the Brazilian disk test might be different from the calculated result with the real tested Poisson's ratio. Even though, current calculated results and fracture situation proved that the Macor is not homogeneous material. Comparing to experimental results, the mechanical properties on the data sheets provided by the manufacturers for three candidate materials are input to the simulation provide different simulation results. Especially for Macor, it is observed to have the smallest equivalent stress (131.96 MPa) under 30 kN in the simulation of Brazilian disk test, but the simulation of 3PB test provides the biggest equivalent stress (197.67 MPa) under the same load. However, the actual mechanical test result of Macor proves that Macor is the most brittle material among three candidate materials, and Macor is a non-homogeneous material. For B_4C and Al_2O_3, the simulation results of Brazilian disk test and 3PB test show the non-homogeneous property of both materials, but it is difficult to prove the simulation conclusion of the Brazilian disk test through the actual fracture status of both materials due to the limitation of the experiment in the thesis. Therefore, the comparison of three candidate materials is only done through the 3PB test with the assumption of homogeneous materials. In this case, B_4C proved to have the biggest Young's modulus (517.9-602.7 GPa) among three candidate materials.

The aim of the study is to compare the experimental data from 3PB test and Brazilian disk test, and to extract the slopes of the Young's modulus from different tests. By calculating the Young's modulus of Macor in the 3PB test and the Brazilian disk, the difference between two values is 56.18%, which is too big. Also, from the crack patterns of Macor in Brazilian disk test, it is obvious that Macor behaves heterogeneously. Therefore, Macor is not homogenous comes to the conclusion, and the Young's modulus cannot be obtained from the 3PB test. The Brazilian disk tests of Al_2O_3 and B_4C can be conducted in future for the comparison of Young's modulus in the 3PB test and the Brazilian disk test, and for the confirmation of the homogeneity of the materials. To get an accurate Young's modulus in the Brazilian disk test, an actual Poisson's ratio of the specimen should be deduced from uniaxial test or Resonant Ultrasound Spectroscopy (RUS) proposed by Jyrki Vuorinen from Tampere University of Technology. The RUS method can be used to analyze the mechanical properties of materials, and only a very small piece of material specimen is needed, compared with uniaxial test. Therefore, the

3PB test results of Al_2O_3 and B_4C are used to compare with Macor by assuming both Al_2O_3 and B_4C are homogeneous material in the study.

6. CONCLUSIONS

The main goal of this thesis is to study three candidate materials, and comparing them with the baseline and the alternative materials which are used for supporting system girders, and mapping candidate materials for forward material study for the supporting system girders. At the start-up of the study, simulations are conducted with the ANSYS software. Afterwards, experiments on the material properties are scheduled so as to measure and compare the simulation results with the tested data.

The selection of candidate materials is based on the properties of the baseline and the alternative materials. In mechanical tests, Al_2O_3 proved to withstand maximum 35.19 kN loads. Macor can withstand the least loads (maximum 24.21 kN) among three materials. In the 3PB test, B_4C is measured to have the biggest maximum Young's modulus of 602.7 GPa and the smallest minimum Poisson's ratio of 0.12 among three candidates, the baseline and the alternative materials. The results are only available with the assumption of homogeneous materials.

Brazilian disk test and 3-point bending test are selected as mechanical tests in the study. By comparing the actual Young's modulus of the specimens in Brazilian disk test and 3PB test, the homogeneity of three candidate materials can be deduced and investigated. In the Brazilian disk test of Macor, the stress concentration is located on the static loading point. When the stress concentration is accumulated until a critical level, a fracture is initiated. After that, the fracture is propagated along the vertical diameter of the specimen. If the material is homogeneous, the crack pattern should be a straight line along the vertical diameter of the specimen. On the contrary, if it is not homogenous, a lot of micro-cracks in the fracture zone are congested and form a primary crack, which is not a straight line, along the vertical diameter. In the 3PB test, the stress concentration is located on the mid-span of the specimen, a fracture is initiated by the accumulated stress concentration, the crack propagation direction prefers the initiated direction of the fracture, and the crack line is along the vertical direction of the specimen. For homogeneous material, the crack line is a straight line at the mid-span location. As shown in the mechanical tests, Macor proved to be a non-homogeneous material. Thus, the Young's modulus of Macor in the 3PB test is not accurate and it can only be used for comparison purpose in the study when assuming all candidate materials are homogenous. Moreover, an accurate Young's modulus for a non-homogeneous material can be obtained by using equations of Brazilian disk test. In this case, the real Poisson's ratio of the specimen is very important for the calculation of the actual Young's modulus, and the actual Pois-

son's ratio has to be tested. In the study, the calculation of the actual Young's modulus in Brazilian disk test is using the theoretical Poisson's ratio due to the limitation of the experiment. In addition, the analysis of the homogeneity of specimen has to be associated with the fracture process and test results of the specimen.

During the data processing, the Young's modulus is calculated with formulas of homogenous materials. As a result, only Macor proved to have different values of Young's modulus. Therefore, the fact that Macor is a non-homogeneous material is stated safely. The mechanical properties from the supplier data sheets are also compared to the experimentally acquired values. It appears that the differences of 22%, 17.5% and 20% for the Young's modulus of the B_4C, Al_2O_3 and Macor exist between experimental and theoretical values. Likewise, there are 18.2% and 55% differences for the Poisson's ratio of Al_2O_3 and Macor.

According to the test results in chapter five, the relationships of the Young's modulus, the Poisson's ratio, the maximum stress and the density of three candidate materials, the baseline material and the alternative material in the 3PB test are (bold values are provided by suppliers):

- $E_{B4C} > E_{Al2O3} > \mathbf{E_{SiC}} > 400$ GPa;
- Maximum $\nu_{B4C} < \mathbf{\nu_{SiC}} < \nu_{Al2O3} < \nu_{Macor} < \mathbf{\nu_{Epument;}}$
- $\mathbf{\sigma_{max}}$ **of SiC (450 MPa)** is the biggest among all the materials;
- $\mathbf{\rho_{Epument} < \rho_{B4C} < \rho_{Macor} < \rho_{SiC} < \rho_{Al2O3}}$

Based on the study of material properties, B_4C is proposed for further study. However, this is a study only for the material properties. The choice for the structural material of the supporting system depends on the combination of feasibility study, manufacturing strategy, radiation hardness cost and resources evaluation, and the overall CLIC Module development schedule.

For further study, the Brazilian disk test can be conducted on B_4C and Al_2O_3, to verify if both materials are homogeneous materials. Moreover, uniaxial test or Resonant Ultrasound Spectroscopy (RUS) can be carried on to obtain the actual Poisson's ratio for calculating the accurate Young's modulus of a non-homogeneous material in the Brazilian disk test. A thermal analysis and an irradiation test under a high energy and neutron beam shall be considered as well.

REFERENCES

[1] Wikipedia, the free encyclopedia [WWW]. [accessed on 21.06.2013]. Available at: http://en.wikipedia.org/wiki/CERN.

[2] Swisscontacts [WWW]. [accessed on 23.06.2013]. Available at: http://www.swisscontacts.ca/portraits/european-organization-nuclear-research-cern-nutshell.html.

[3] CERN accelerating science [WWW]. [accessed on 23.06.2013]. Available at: http://home.web.cern.ch/about/member-states.

[4] CERN accelerating science [WWW]. [accessed on 23.06.2013]. Available at: http://ts-dep.web.cern.ch/ts-dep/groups/lea/int/workshops/.

[5] CERN accelerating science [WWW]. [accessed on 27.06.2013]. Available at: http://angelsanddemons.web.cern.ch/about/mission.

[6] Aicheler, M., Burrows, P., Draper, M., Garvery, T., Lebrun, P., Peach, K., Phinney, N., Schmickler, H., Schulte, D., Toge, N. A Multi-TeV Linear Collider based on CLIC technology. Geneva 2012, CERN, CERN-2012-007. 841 p.

[7] CERN accelerating science [WWW]. [accessed on 03.07.2013]. Available at: http://clic-study.web.cern.ch/CLIC-Study/Layout/OverallCLIC3.html.

[8] CLIC-study [WWW]. [accessed on 03.07.2013]. Available at: http://clic-study.org/accelerator/CLIC-inaNutshell.php.

[9] G.Riddone, A.Samoshkin, D.Gudkov. CLIC Two-Beam Module design and integration. CERN, CERN-ATS-2010-216. 3p.

[10] N.Gazis., G.Riddone., H. Mainaud-Durand., D.Gudkov., A.Samoshkin., S.Simopoulos., E.Hinis., T.Alexopoulos. Study of the supporting system for the CLIC Two-Beam Module. DURACOSYS Conference, Greece, 12-15 September 2010. Geneva, Switzerland, September 2010. pp. 2-7.

[11] N.Gazis. Technical Specification for the Supporting Systems of the RF-Structures for the CLIC two-beam prototype modules in CLEX. CERN, November 2011. EDMS CERN 1164992, IT-3713/BE/CLIC. 31 p.

[12] N.Gazis. Study of the supporting system for the CLIC Two-Beam Module. CERN/NTNU, December 2010. Presentation. 35 p.

[13] N.Gazis. Technical Specification of the Main Beam girder with V-shaped supports for the CLIC two-beam module type 1. CERN, March 2012. EDMS CERN 1180917, 22 p.

[14] Paul Scherrer Institut [WWW]. [accessed on 28.08.2013]. Available at: http://www.psi.ch/.

[15] The European XFEL [WWW]. [accessed on 08.16]. Available at: http://xfel.desy.de/localfsExplorer_read?currentPath=/afs/desy.de/group/xfel/wof/EPT/TDR/XFEL-TDR-Ch-4.pdf.

[16] Giuseppe Magnani et al. Pressureless sintered silicon carbide with enhanced mechanical properties obtained by the two-step sintering method. Ceramics International. Volume 40 (2014), pp 1759-1763.

[17] Bruno Masenelli, From Small Fullerenes to Superlattices, Science and applications. Pan Stanford Publishing 2012. pp 121–162.
[18] Crystallography and Engineering Properties of Ceramics, Engineered Materials Handbook Desk Edition, ASM International, 1995, pp. 922–975.
[19] J.R. Davis, Guide to Materials Selection, Engineered Materials Handbook Desk Edition, ASM International, 1995, pp. 106–154.
[20] Russell H.Jones et al. Environmental Effects on Engineered Materials. CRC Press 2001. P 28.
[21] Vladislav, D., Sara, R., Richard, A, H., Manish, C. Boron Carbide: Structure, Properties, and Stability under Stress. Journal of the American Ceramic Society 94(2011), pp. 3605-3628.
[22] H.K.Clark., J.L.Hoard. The crystal structure of Boron Carbide. Journal of The American Chemical Society 65(1943)11, pp. 2115-2119.
[23] G.L. DePoorter, T.K. Brog, and M.J. Readey, Structural Ceramics, Properties and Selection: Nonferrous Alloys and Special-Purpose Materials, Vol 2, ASM Handbook, ASM International, 1990, pp 1019–1024.
[24] D.M.Rowe, CRC Handbook of Thermoelectrics. CRC Press 1995. P 14.
[25] Glass Processing, Engineered Materials Handbook Desk Edition, ASM International, 1995, pp. 1115–1170.
[26] Glass Fab, Inc [WWW]. [accessed on 10.07.2013]. Available at: http://www.glassfab.com/file/sites|*|537|*|Data-Sheets|*|Corning-Macor.pdf.
[27] A. Osaka, Ceramic Materials, Materials for Medical Devices. Vol 23, ASM Handbook, ASM International, 2012, pp 265–277.
[28] Wikipedia, the free encyclopedia [WWW]. [accessed on 10.04.2013]. Available at: https://en.wikipedia.org/wiki/File:Boron_carbide.JPG.
[29] Yixing Feifan Ceramics Co.,Ltd [WWW]. [accessed on 10.04.2013]. Available at: http://www.al2o3-ceramic.com/photo/pl888434-95_al2o3_white_aluminum_oxide_ceramic_round_plate_with_surface_finish_ra_0_4_sim_ra_0_8.jpg.
[30] Made-in-China [WWW]. [accessed on 10.04.2013]. Available at: http://www.made-in-china.com/showroom/innovacera/product-detailCvDnrqLUbQWO/China-Machinable-Glass-Ceramics-Ceramic-Insulator-Macor.html.
[31] J.L. Ellis and C.G. Goetzel, Cermets, Properties and Selection: Nonferrous Alloys and Special-Purpose Materials, Vol 2, ASM Handbook, ASM International, 1990, pp 978–1007.
[32] Online Materials Information Resourse [WWW]. [accessed on 07.03.2013]. Available at: http://www.matweb.com/.
[33] D. Wilson and L.A. Carlsson, Mechanical Testing of Fiber-Reinforced Composites, Mechanical Testing and Evaluation, Vol 8, ASM Handbook, ASM International, 2000, pp. 905–932.

[34] Metalworking Processes, Mechanical Testing and Evaluation, Vol 8, ASM Handbook, ASM International, 2000, pp 70–78.
[35] Ceramic-Matrix Composites, Engineered Materials Handbook Desk Edition, ASM International, 1995, pp. 1059–1093.
[36] Diyuan Li, Louis Ngai, Yuen Wong. The Brazilian Disc Test for Rock Mechanics Applications: Review and New Insights. Rock Mech Rock Eng (2013) 46, pp 269-287.
[37] Hadi Haeri et al., Experimental and numerical study of crack propagation and coalescence in pre-cracked rock-like disks. International Journal of Rock Mechanics & Mining Sciences. 67 (2014). pp.20-28.
[38] Yong Yu et al. A modified Brazilian disk tension test. International Journal of Rock Mechanics & Mining Sciences. 46 (2009). pp. 421-425.
[39] Hudson JA et al,. The controlled failure of rock discs and rings loaded in diametral compression. Int J Rock Mech Min Sci 1972;9(2): 241–4.
[40] K.Khan, N.A.Al-Shayea. Effect of Specimen Geometry and Testing Method on Mixed Mode I-II Fracture Toughness of a Limestone Rock from Saudi Arabia. Rock Mech. Rock Engng. (2000) 33 (3), pp 179-206.
[41] Abbass Tavallali et al., Behaviour of layered sandstone under Brazilian test conditions: Layer orientation and shape effects. Journal of Rock Mechanics and Geotechnical Engineering. 5 (2013). pp. 366-377.
[42] Ye Jianghong., F.Q.Wu., J.Z.Sun. Estimation of the tensile elastic modulus using Brazilian disc by applying diametrically opposed concentrated loads. International Journal of Rock Mechanics & Mining Sciences 46(2009) pp. 568-576.
[43] (Room-Temperature Strength Test Methods for Isotropic Ceramics) Testing and Characterization of Ceramics, Engineered Materials Handbook Desk Edition, ASM International, 1995, pp. 865–904.
[44] Mechanical Testing of Polymers and Ceramics, Mechanical Testing and Evaluation, Vol 8, ASM Handbook, ASM International, 2000, pp 26–48.
[45] Luca Collini et al., Flexural strength of glass-ceramic for structural applications. Journal of the European Ceramic Society. 34 (2014). pp. 2675-2685.
[46] E. Shapiro, Bend Testing, Mechanical Testing and Evaluation, Vol 8, ASM Handbook, ASM International, 2000, pp 172–184.
[47] Standard Test Method for Flexural Strength of Concrete (Using Simple Beam With Center-Point Loading), ASTM standards, C 293-00 (2001). pp 168-170.
[48] K.A.Silva. Standard Specifications for Casting Tolerances – Linear Dimensions. InForce Rapid Proto Casting Inc., V ancouver, WA, USA 98685. September 2008. P. 8.
[49] MISUMI India [WWW]. [accessed on 20.07.2013]. Available at: http://in.misumi-ec.com/contents/tech/press/29.html.
[50] FRIALIT-DEGUSSIT Technical Ceramics [WWW]. [accessed on 20.07.2013]. Available at: http://www.degussit.co.uk/Tolerances.htm.
[51] ANSYS [WWW]. [accessed on 16.04.2013], Available at: http://www.ansys.com/Products?path=/WWW/htdocs/fluent/software/platform/.

[52] Laboratory Testing Inc. [WWW]. [accessed on 16.04.2013]. Available at: http://www.labtesting.com/services/materials-testing/mechanical-testing/.
[53] LMATS [WWW]. [accessed on 16.04.2013]. Available at: http://www.lmats.com.au/resource-centre/mechanical-testing.html.
[54] W.C.Zhu, C.A.Tang. Numerical simulation of Brazilian disk rock failure under static and dynamic loading. International Journal of Rock Mechanics & Mining Sciences 43 (2006). pp. 236-252.
[55] S.K.Kourkoulis et al,. The Brazilian disc under parabolically varying load: theoretical and experimental study of the displacement field. International Journal of Solids and Structures 49 (2012). pp. 959-972.
[56] S.K.Kourkoulis et al,. The standardized Brazilian disk test as a contact problem. International Journal of Rock Mechanics & Mining Sciences 57 (2013). pp. 132-141.
[57] Rice University [WWW]. [accessed on 06.06.2013]. Available at: http://www.owlnet.rice.edu/~msci301/ThermalExpansion.pdf.
[58] Guowei Zeng et al., Simulation of damage evolution and crack propagation in three-point bending pre-cracked asphalt mixture beam. Construction and Building Materials. 55 (2014). pp. 323-332.
[59] Anyi Yin et al., Multiscale fracture simulation of three-point bending asphalt mixture beam considering material heterogeneity. Engineering Fracture Mechanics 78 (2011). pp. 2414-2428.
[60] Anyi Yin et al., Fracture simulation of pre-cracked heterogeneous asphalt mixture beam with movable three-point bending load. Construction and Building Materials. 65 (2014). pp. 232-242.

APPENDIX 1: ORIGINAL TESTING DATA

Mechanical tests.xlsx

20121018_BR-S-_Comprative_Graphs.x

20130121_BR-B-_Comprative_Graphs.x

APPENDIX 2: MATERIAL DATASHEETS

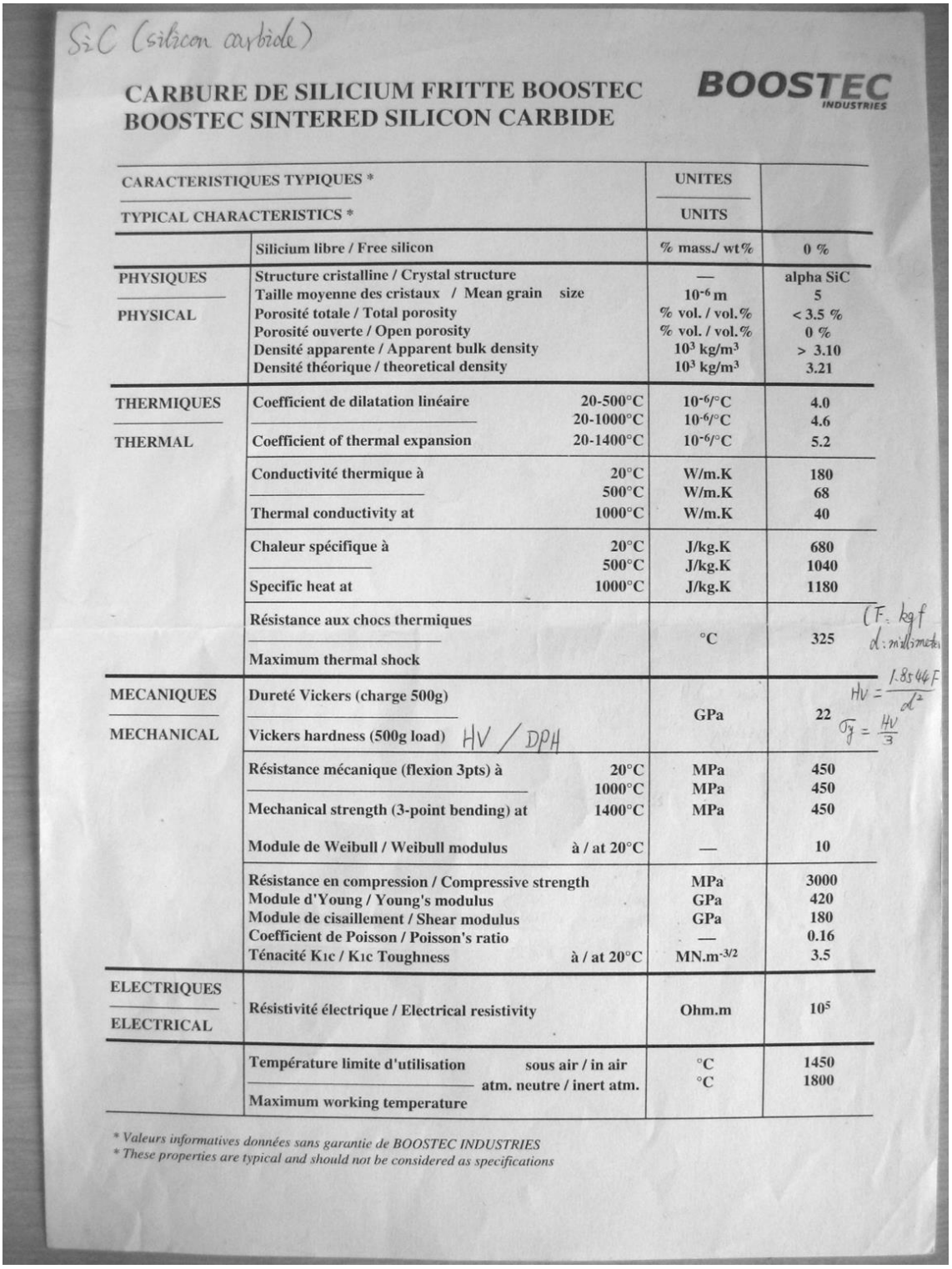

SiC (silicon carbide)

CARBURE DE SILICIUM FRITTE BOOSTEC
BOOSTEC SINTERED SILICON CARBIDE

BOOSTEC INDUSTRIES

CARACTERISTIQUES TYPIQUES * / TYPICAL CHARACTERISTICS *			UNITES / UNITS	
	Silicium libre / Free silicon		% mass./ wt%	0 %
PHYSIQUES / PHYSICAL	Structure cristalline / Crystal structure		—	alpha SiC
	Taille moyenne des cristaux / Mean grain size		10^{-6} m	5
	Porosité totale / Total porosity		% vol. / vol.%	< 3.5 %
	Porosité ouverte / Open porosity		% vol. / vol.%	0 %
	Densité apparente / Apparent bulk density		10^3 kg/m^3	> 3.10
	Densité théorique / theoretical density		10^3 kg/m^3	3.21
THERMIQUES / THERMAL	Coefficient de dilatation linéaire	20-500°C	10^{-6}/°C	4.0
		20-1000°C	10^{-6}/°C	4.6
	Coefficient of thermal expansion	20-1400°C	10^{-6}/°C	5.2
	Conductivité thermique à	20°C	W/m.K	180
		500°C	W/m.K	68
	Thermal conductivity at	1000°C	W/m.K	40
	Chaleur spécifique à	20°C	J/kg.K	680
		500°C	J/kg.K	1040
	Specific heat at	1000°C	J/kg.K	1180
	Résistance aux chocs thermiques		°C	325
	Maximum thermal shock			
MECANIQUES / MECHANICAL	Dureté Vickers (charge 500g)		GPa	22
	Vickers hardness (500g load) HV / DPH			
	Résistance mécanique (flexion 3pts) à	20°C	MPa	450
		1000°C	MPa	450
	Mechanical strength (3-point bending) at	1400°C	MPa	450
	Module de Weibull / Weibull modulus	à / at 20°C	—	10
	Résistance en compression / Compressive strength		MPa	3000
	Module d'Young / Young's modulus		GPa	420
	Module de cisaillement / Shear modulus		GPa	180
	Coefficient de Poisson / Poisson's ratio		—	0.16
	Ténacité K1c / K1c Toughness	à / at 20°C	MN.m$^{-3/2}$	3.5
ELECTRIQUES / ELECTRICAL	Résistivité électrique / Electrical resistivity		Ohm.m	10^5
	Température limite d'utilisation	sous air / in air	°C	1450
		atm. neutre / inert atm.	°C	1800
	Maximum working temperature			

CF: kgf
d: millimeter
$HV = \frac{1.8544F}{d^2}$
$\sigma_f = \frac{HV}{3}$

* *Valeurs informatives données sans garantie de BOOSTEC INDUSTRIES*
* *These properties are typical and should not be considered as specifications*

EPUCRET
discover the future

www.rampf-gruppe.de

Technical Data Sheet
EPUMENT 145B

Product description	EPUMENT 145B – is a three component cast polymer based on an epoxy resin including a more special filler combination consisting of raw materials. Due to state-of-the-art batching, mixing and vibrating engineering, a high performance material is achieved which is homogenous, optimally compact and low on entrapped air.
Properties	• Highest rigidity • Low thermal conductivity • Thermal expansion coefficient adjusted to steel • Lowest creep behaviour under stress influence
Application	For casting big weldments or cast constructions e.g. machine parts (pillars, machine stands and engine beds) as well as substructures for assemblies strained by vibration e.g. engines, gear, turbines, centrifuges and test rigs to get a higher static and dynamic rigidity.

Mechanical data

• **Density**	approx. 2,4 g/cm³	
• **Compressive strength ***	130 - 150 N/mm²	
• **Flexural strength ***	30 - 40 N/mm²	
• **Modulus of elasticity ***	40 - 45 kN/mm²	
• **Poisson's ratio**	approx. 0,30	
• **Logarithmic decrement**	0,022	
• **Thermal expansion coefficient**	approx. 15 · 10^{-6} K^{-1}	at 20 °C
• **Thermal conductivity**	approx. 2,9 W/mK	at 25 °C
• **Specific heat capacity**	approx. 0,73 J/g K	at 25 °C
• **Thermal diffusivity**	approx. 1,75 mm²/s	at 25 °C
• **Wall thickness**	> 90 mm	
• **Maximum grain size**	16 mm	

Note	All recommendations for the use of our products are based on years of experience and the current state of our knowledge. Notwithstanding any such recommendations the Buyer shall remain responsible for satisfying himself that the products are suitable for his intended process or purpose. Since we cannot control the application, use or processing of the products, we cannot accept responsibility therefore. The Buyer shall ensure that the intended use of the products will not infringe any third party's intellectual property rights. We warrant that our products are free from defects in accordance with and subject to our general conditions of supply.

* measured by the testing machine Form + Test Seidner, Typ 502/3000/100SP

EPUCRET Mineralgusstechnik GmbH & Co.KG
Daimlerstraße 18-26 • D-73117 Wangen bei Göppingen • T +49 (0) 7161 95889-0 • F +49 (0) 7161 95889-29
E info@epucret.de • http://www.epucret.de

ABSCO MATERIALS

Product Data Sheet

Boron Carbide

Chemical

	Total B	Total C	B_4C
F4 – F150	77-80 %	17-21 %	96-98 %
F180 – F400	76-79 %	17-21 %	95-97 %
F500 – F800	75-78 %	17-21 %	94-97 %
F1000 – F1500	74-78 %	17-21 %	93-97%
-10µ or -25µ	76-81 %	17-21 %	93-97 %
-100, -200, -325 mesh	76-81 %	17-21 %	93-97 %
-60 + 150 mesh	76-81 %	17-21 %	93-97 %
B_2O_3	max 0.5%		
Fe2O3	max 0.5 %		

Physical (typical)

Density	>2.48 g/cm^3	hot pressed and sintered
Hardness (Knoop 100g)	2900-3580	
Fracture Toughness	2.9-3.7 MPa.m$^{1/2}$	
Young's Modulus	450-470 GPa	
Electrical Conductivity(25^{o}C)	140 S	
Thermal Conductivity (25^{o}C)	30-42 W/m.K	
Thermal Expansion Coefficient	5 x 10^{-6}/^{o}C	

Boron Carbide

Appearance	Application
Black powder	Refractory, Wear Resistant and Structural Ceramics Metal Matrix Composites Nuclear Shielding Grinding, Polishing and Lapping Ballistic armour

Material can also be supplied as hot pressed and sintered pieces up to 400 x 400 mm^2

CAS Number 12069-32-8

Transport Non hazardous

ABSCO Materials, 42 Hollands Road, Haverhill, Suffolk CB9 8SA, England

Tel : +44 (0)1440 709709 / Fax : +44 (0)1440 709708 / enquiries@abscomaterials.com

A partnership between ABSCO Ltd and Hertford Resources Ltd

CARBOSYSTEM®

ALUMINA OXIDE MATERIAL

PHYSICAL AND MECHANICAL PROPERTIES

QUALITY		CB271	CB272	CB273	CB274	CB275	CB276	CB277	CB278	CB279
Alumina Content (Al_2O_3)	%	60	75	80	85	92	95	99	99,5	99,8
Porosity	%	20	0,1	0	0	0	0	0	0	0
Density	g/cm^3	3,00	3,10	3,30	3,40	3,60	3,70	3,81	3,90	3,91
Hardness	Mohs	7,5	7,5	7,5	7,5	8,5	8,8	9,0	9,5	9,5
Flexural Strength	MPa	205	280	216	230	312	304	340	360	370
Thermal Expansion Coeff.	$10^{-6}/°C$	7,1	7,6	7,6	7,6	7,5	7,3	7,6	7,6	7,6
Dielectric Strength	KV/mm	10	10	10	10	10	10	10	10	10
Thermal Conductivity	W/m.K	16	17	17	17	18	20	34	35	36
Volume Resistance at 20 °C	Ωcm	1014	1014	1014	1014	1014	1014	1014	1014	1014
at 300 °C	Ωcm	1013	1013	1013	1013	1013	1012	1010	1010	1010
Safe Use Temperature	°C	1350	1100	1300	1350	1500	1600	1700	1800	1800

These properties are typical average value

Macor®

Machinable Glass Ceramic

Features

- Machinable with ordinary metalworking tools
- Macor allows fast turnaround, no post firing required
- Holds tight tolerances, up to 0.0005in. (0.013mm)
- Withstands high temperature, up to 1000°C (no load)
- Macor is clean, no outgasing and zero porosity.

Properties

Macor MGC has a continuous use temperature of 800°C and a peak temperature of 1000°C. Its coefficient of thermal expansion readily matches most metals and sealing glasses. It is nonwetting, exhibits zero porosity, and unlike ductile materials, won't deform. It is an excellent insulator at high voltages, various frequencies and high temperatures. And, when properly baked out, it won't outgas in vacuum environments.

Machining

Machining tolerances are surprisingly tight, up to 0.0005in. (0.013mm). Macor MGC can be machined to a surface finish of less than 20µin. (o.5µn) and polished to a smoothness of 0.5µin. (0.013µm). Configurations are limited only by available equipment and the experience of the machinist.

Sealing, joining and metalising

Macor MGC can also be joined or sealed-both to itself and to other materials-in a number of ways; metalised parts can be soldered together and brazing has proved to be effective method of joining the material to various metals: epoxy produces a strong joint, and sealing glass create a vacuum tight seal. Even a straightforward mechanical joint is possible. It can be thick film metalised using metal inks, or thin film metalised by sputtering.

Applications

Ultra-high vacuum environments

Macor MGC is used as an insulator or coil support and for vacuum feed-troughs. In these applications the conductive materials are supported by the Macor MGC part and a compatible sealing glass is used to produce a vacuum-tight, hermetic seal.

Constant vacuum applications

Macor MGC parts are found in spacers, headers and windows for microwave tube devices and as sample holders in field ion microscopes.

Aerospace industry

Over 200 distinctly shaped Macor MGC parts can be found on America's reusable Spacer Shuttle Orbiter. Retaining rings of Macor MGC are used at all hinge points, windows and doors.
Also, large pieces of Macor glass ceramic are used in a NASA spaceborne gamma radiation detector. For this application frame corners are joined by a combination of machined (butt-lap) mechanical joints and a sealing glass.

Nuclear-related experiments

Since Macor MGC is not dimensionally affected by irradiation, small cubes of the material are machined to a tolerance of one micron and are used as a reference piece to measure dimensional change in other materials.

Welding nozzles

Welding equipment manufacturers are using Macor MGC as a nozzle on the tips of oxyacetylene torches. The material's nonwetting characteristic means molten particles won't adhere to and decrease the effectiveness of the nozzle.

Fixtures

Macor MGC is used as an electrode support and burner block in several industrial high heat, electrical cutting operations due to its low thermal conductivity and excellent electrical properties.

Medical Equipment

Producers of medical components are intrigued by Macor MGC's inertness, precise machinability and dimensional stability.

Conclusion

When you need the performance of a technical ceramic- (high use temperature, electrical resistivity, zero porosity) – and your application demands the ready fabrication of a complicated shape look at Macor MGC. It will lower costs and substantially reduce the time between design and actual use.

Properties

Thermal

	SI/Metric	Imperial
Coefficient of expansion -200-25°C 25-300°C 25-600°C	 7.4 x 10^{-6}/°C 9.3 x 10^{-6}/°C 12.6 x 10^{-6}/°C	 41 x 10^{-7}/°F 52 x 10^{-7}/°F 70 x 10^{-7}/°F
Specific heat 25°C	0.79 KJ/kg°C	0.19 Btu/lb°F
Thermal Conductivity 25°C	1.46 W/m°C	10.16 Btu in / Hr ft²°F
Thermal diffusivity 25°C	7.3 x 10^{-7}m²/s	0.028ft²/hr
Continuous operating temp	800°C	1472°F
Maximum no load temp	1000°C	1832°F

Mechanical

	SI/Metric	Imperial
Density	2.52g/cm³	157lbs/ft³
Porosity	0%	0%
Young's modulus 25°C (Modulus of Elasticity)	66.9 GPa	9.7 x 10^6psi
Poisson's ratio	0.29	0.29
Shear modulus 25°C	25.5 GPa	3.7 x 10^6psi
Hardness Knoop 100g Rockwell A	 250 48	 250 48
Modulus of rupture 25°C Flexural Strength	94Mpa Min. specified average value	13,600 psi Min. specified Average value
Compressive Strength	345MPa	50,000 psi
Fracture Toughness	1.53MPa $m^{0.5}$	1,390psi $in^{0.5}$

Electrical

	SI/Metric	Imperial
Dielectric constant 25°C 1KHz 8.5GHz	 6.03 5.67	 6.03 5.67
Loss tangent 25°C 1KHz 8.5GHz	 4.7 x 10^{-3} 7.1 x 10^{-3}	 4.7 x 10^{-3} 7.1 x 10^{-3}
Dielectric Strength (25°C) AC avg. (12mm thickness) DC avg.(12mm thickness)	 9.4KV/mm 62.4KV/mm	 785V/mil 5206V/mil
DC volume resistivity 25°C	>10^{16} ohm-cm	>10^{16} ohm-cm

Chemical

Tests				Results
Solution	pH	Time	Temp	Weight loss (mg/cm²) gravimetric
5% HCl Hydrochloric Acid	0.1	24 hrs	95°C	~100
0.002 N HNO_3 Nitric Acid	2.8	24 hrs	95°C	~0.6
0.1 N $NaHCO_3$ Sodium Bicarbonate	8.4	24 hrs	95°C	~0.3
0.02 N Na_2CO_3 Sodium Carbonate	10.9	6 hrs	95°C	~0.1
5% NaOH Sodium Hydroxide	13.2	6 hrs	5°C	~10
Resistance to water over time H_20	7.6	1 day* 3 days* 7 days* 3 days# 6 days#	95°C 95°C 95°C 95°C 95°C	0.01 0.07 9.4 0.06 0.11

* - Water not freshened daily # - Water freshened daily

Machining
Key factors for successful machining are proper machining speeds and coolant. Macor MGC can be machined with high-speed steel tools, but carbide tools are recommended for longer wear. Achieve the best results by using a water-soluble coolant especially formulated for cutting and grinding glass or ceramics.
No post firing is required after machining.

Sawing
Use a carbide grit blade at a band speed of 100fpm. (30.5m/min). An alternative is a silicon carbide or diamond cut-off wheel.

Turning
Cutting speed…. 30-50sfm (9-15m/min)
Feed rate……. 002-.005ipr
(0.005-0.013cm/rev)
Depth of cut… .150-.250in. (0.38-0.64cm)

Milling
Cutting speed… 20-35sfm(6.1-10.7m/min)
Chip load…… .002ipt(0.05mm per tooth)
Depth of cut ……150-. 200in. (0.38-0.51cm)

Drilling

Drill Size	Spindle Speed	Feed rate
¼ in (0.64cm)	300rpm	.005ipr 0.013cm/rev
½ in (1.27cm)	250rpm	.007ipr 0.018cm/rev
¾ in (1.90cm)	200rpm	.010ipr 0.025cm/rev
1 in (2.54cm)	100rpm	.012ipt 0.030cm/rev
2 in (5.08 cm)	50rpm	.015ipr 0.038cm/rev

Allow at least 0.50in (0.13cm) of extra material on the backside for breakout. This excess can be moved after drilling.

Tapping
Make clearance holes one size larger than those recommended for metals. Chamfer both ends of the hole to reduce chipping. Run the tap in one direction only. Turning the tap back and forth can cause chipping. Continuously flush with water or coolant to clear chips and dust from the tap.

Grinding
Diamond, silicon carbide or aluminium oxide grinding wheels can be used.

Polishing
Start with loose 400-grit silicon carbide on a steel wheel. For the final polish, use cerium oxide or alumina on a polishing pad for glass or ceramics. A 0.5µin. (0.013µm) finish can be achieved.

Composition
Macor MGC is a white, odourless, porcelain-like (in appearance) material composed of approximately 55% fluorophlogopite mica and 45% borosilicate glass. It has no known toxic effects: however the dust created in machining can be an irritant. Good housekeeping and appropriate machining techniques can avoid this irritation. The material contains the following compounds:

	Approx. weight %
Silicon – $Si0_2$	46%
Magnesium – MgO	17%
Aluminium – AL_20_3	16%
Potassium – K_20	10%
Boron – B_20_3	7%
Fluorine – F	4%

Ceramic Substrates & Components Ltd

Technical Data

The general characteristics of **Macor** were derived from laboratory tests performed by Corning from time to time on sample quantities. Actual characteristics of production lots may vary.

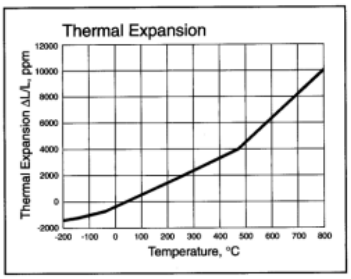

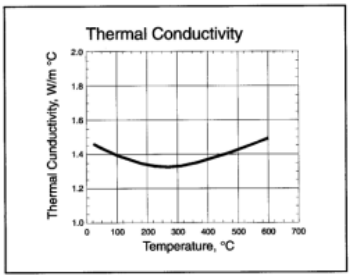

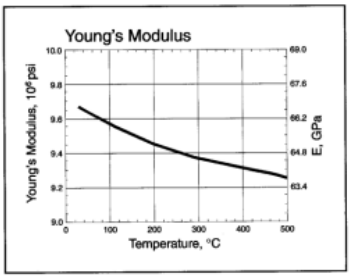

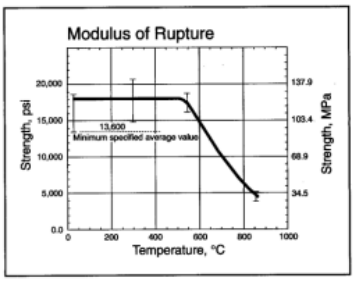

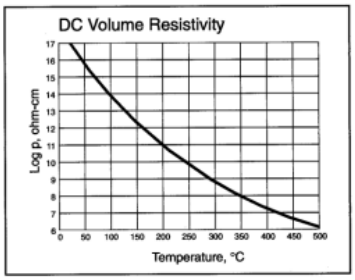

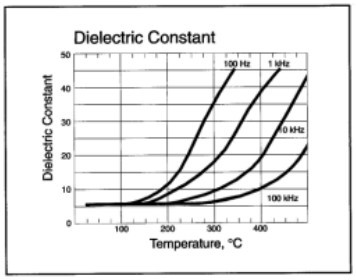

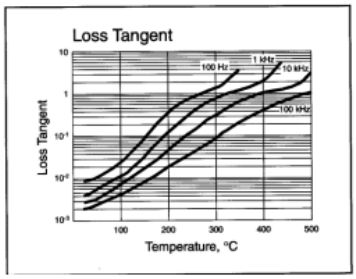

Ceramic Substrates & Components Ltd

APPENDIX 3: THE DATA SHEET OF HBM STRAIN GAUGE

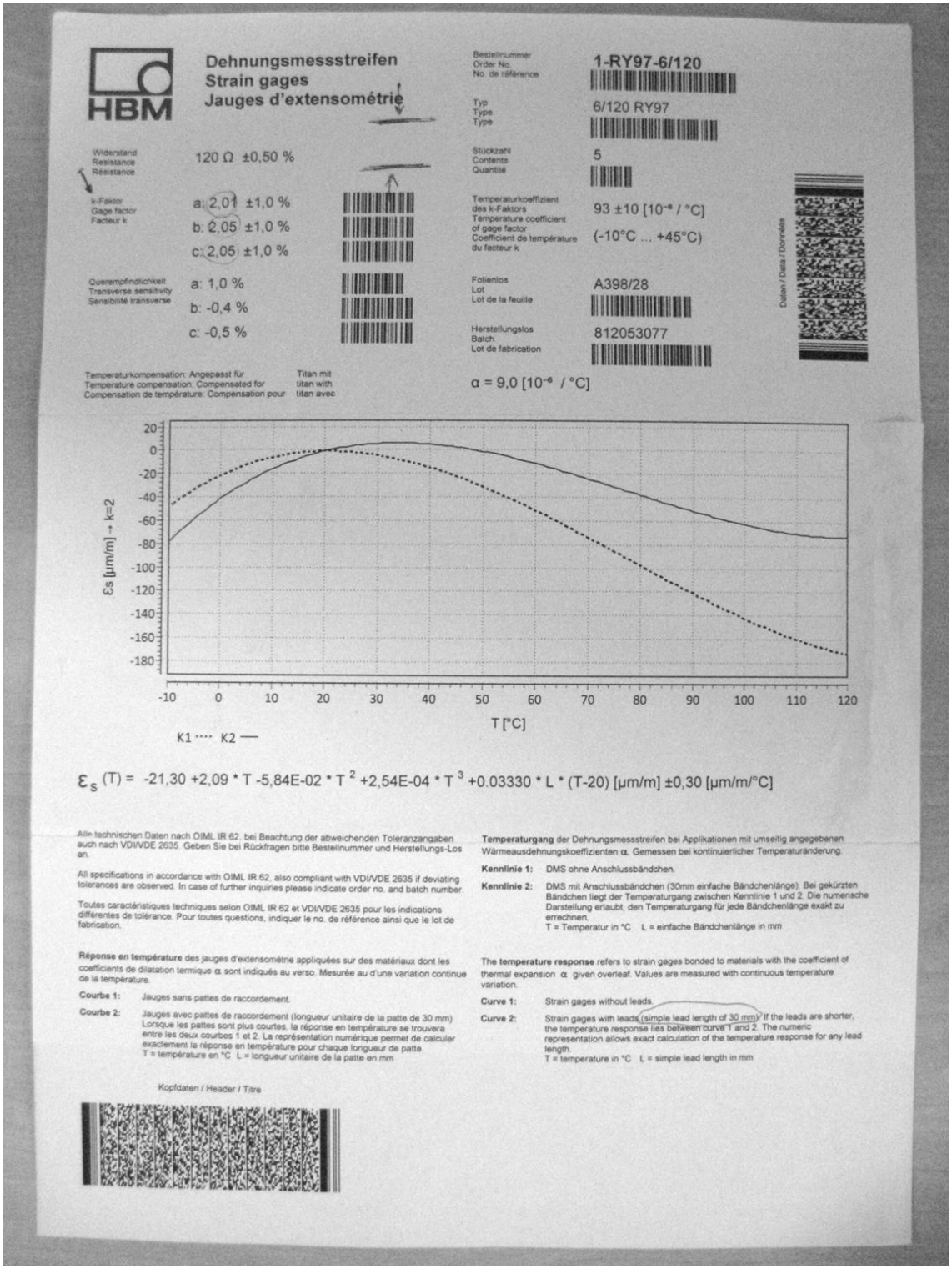

HBM

Dehnungsmessstreifen
Strain gages
Jauges d'extensométrie

Bestellnummer / Order No. / No. de référence: **1-RY97-6/120**

Typ / Type / Type: 6/120 RY97

Stückzahl / Contents / Quantité: 5

Widerstand / Resistance / Résistance: 120 Ω ±0,50 %

k-Faktor / Gage factor / Facteur k:
a: 2,01 ±1,0 %
b: 2,05 ±1,0 %
c: 2,05 ±1,0 %

Temperaturkoeffizient des k-Faktors / Temperature coefficient of gage factor / Coefficient de température du facteur k: 93 ±10 [10^{-6} / °C] (-10°C ... +45°C)

Querempfindlichkeit / Transverse sensitivity / Sensibilité transverse:
a: 1,0 %
b: -0,4 %
c: -0,5 %

Folienlos / Lot / Lot de la feuille: A398/28

Herstellungslos / Batch / Lot de fabrication: 812053077

Daten / Data / Données

Temperaturkompensation: Angepasst für Titan mit
Temperature compensation: Compensated for titan with
Compensation de température: Compensation pour titan avec

α = 9,0 [10^{-6} / °C]

ε_s (T) = -21,30 +2,09 * T -5,84E-02 * T^2 +2,54E-04 * T^3 +0.03330 * L * (T-20) [µm/m] ±0,30 [µm/m/°C]

Alle technischen Daten nach OIML IR 62, bei Beachtung der abweichenden Toleranzangaben auch nach VDI/VDE 2635. Geben Sie bei Rückfragen bitte Bestellnummer und Herstellungs-Los an.

All specifications in accordance with OIML IR 62, also compliant with VDI/VDE 2635 if deviating tolerances are observed. In case of further inquiries please indicate order no. and batch number.

Toutes caractéristiques techniques selon OIML IR 62 et VDI/VDE 2635 pour les indications différentes de tolérance. Pour toutes questions, indiquer le no. de référence ainsi que le lot de fabrication.

Réponse en température des jauges d'extensométrie appliquées sur des matériaux dont les coefficients de dilatation termique α sont indiqués au verso. Mesurée au d'une variation continue de la température.

Courbe 1: Jauges sans pattes de raccordement.

Courbe 2: Jauges avec pattes de raccordement (longueur unitaire de la patte de 30 mm). Lorsque les pattes sont plus courtes, la réponse en température se trouvera entre les deux courbes 1 et 2. La représentation numérique permet de calculer exactement la réponse en température pour chaque longueur de patte.
T = température en °C L = longueur unitaire de la patte en mm

Temperaturgang der Dehnungsmessstreifen bei Applikationen mit umseitig angegebenen Wärmeausdehnungskoeffizienten α. Gemessen bei kontinuierlicher Temperaturänderung.

Kennlinie 1: DMS ohne Anschlussbändchen.

Kennlinie 2: DMS mit Anschlussbändchen (30mm einfache Bändchenlänge). Bei gekürzten Bändchen liegt der Temperaturgang zwischen Kennlinie 1 und 2. Die numerische Darstellung erlaubt, den Temperaturgang für jede Bändchenlänge exakt zu errechnen.
T = Temperatur in °C L = einfache Bändchenlänge in mm

The **temperature response** refers to strain gages bonded to materials with the coefficient of thermal expansion α given overleaf. Values are measured with continuous temperature variation.

Curve 1: Strain gages without leads.

Curve 2: Strain gages with leads (simple lead length of 30 mm). If the leads are shorter, the temperature response lies between curve 1 and 2. The numeric representation allows exact calculation of the temperature response for any lead length.
T = temperature in °C L = simple lead length in mm

Kopfdaten / Header / Titre